Silicon-Based Resonant Microsensor Platform
for Chemical and Biological Applications

A Dissertation
Presented to
The Academic Faculty

By

Jae Hyeong Seo

In Partial Fulfillment
Of the Requirements for the Degree
Doctor of Philosophy in the
School of Electrical and Computer Engineering

Georgia Institute of Technology

December 2007

Silicon-Based Resonant Microsensor Platform
for Chemical and Biological Applications

Approved by:

Dr. Oliver Brand, Advisor
School of Electrical and Computer
Engineering
Georgia Institute of Technology

Dr. Mark G. Allen
School of Electrical and Computer
Engineering
Georgia Institute of Technology

Dr. Albert B. Frazier
School of Electrical and Computer
Engineering
Georgia Institute of Technology

Dr. Jennifer E. Michaels
School of Electrical and Computer
Engineering
Georgia Institute of Technology

Dr. Jim Spain
School of Civil and Environmental
Engineering
Georgia Institute of Technology

Dr. Henry Baltes
ETH Zurich
Zurich, Switzerland

Date Approved: October 29, 2007

To my family for their endless encouragement and patience

ACKNOWLEDGEMENTS

There are many people who deserve my sincere heartfelt appreciation. Because of their help and support, my life during the past few years was tolerable and will remain a good memory.

First of all, I would like to thank my advisor Dr. Oliver Brand for his continuous support, encouragement, and confidence throughout my study towards this Ph. D. He gave me the chance to be the first member of his group and allowed independent thought and research. I appreciate the friendly guidance on the research that I conducted and the good time we had together.

I like to thank dissertation committee: Dr. Mark G. Allen, Dr. Albert B. Frazier, Jeniffer E. Michaels, Dr. Jim C. Spain, and Dr. Henry Baltes, for their helpful discussions and generous assistance to my research.

I am grateful to my colleagues in our research group for their assistance and useful discussions about my research. I would like to thank all my current and past group mates: Robert Sunier, Prateek Tandon, Thomas M. Schweizer, Kianoush Naeli, Stefan Schild, Kemal Safak Demirci, Albert Byun, Stuart Truax, Juan M. Cesaretti, and Luke A. Beardslee. I hope all of them achieve brilliant success in their careers.

I owe special thanks to all of the MIRC staff for their assistance. Particularly, I would like to thank cleanroom manager Mr. Gary Spinner for his technical support and consideration. He made my cleanroom life more comfortable and enjoyable. And I wish to thank all of my Korean friends. I have enjoyed the talk about research and life and benefited a lot from their help.

I would like to express my sincere gratitude to my mother, parents-in-law, sisters, brothers-in-law, and sisters-in-law for their never-ending encouragement and patience. Finally, I would love to express my special thanks to my wife, Hye Jeong for her love and patience, my son Jin Myeong, and my daughter Young Sun.

TABLE OF CONTENTS

LIST OF TABLES

LIST OF FIGURES

LIST OF ABBREVIATIONS

AW	Acoustic Wave
AFM	Atomic Force Microscopy
APTES	Aminopropyl Triethoxysilane
BAW	Bulk Acoustic Wave
BSA	Bovine Serum Albumin
CHEMFET	Chemically Sensitive Field Effect Transistor
CMOS	Complementary Metal Oxide Semiconductor
ENFET	Enzymatically Selective Field Effect Transistor
FEM	Finite Element Method
FET	Field Effect Transistor
FO	Fiber Optic
FPW	Flexural Plate Wave
ICP	Inductively Coupled Plasma
IDT	Inter-Digitated Transducer
ISFET	Ion Selective Field Effect Transistor
KOH	Potassium Hydroxide
MZI	Mach-Zehnder Interferometer
PECVD	Plasma Enhanced Chemical Vapor Deposition
PEEK	Polyetheretherketone
PENT	Pentaerythritol Tetranitrate
PMMA	Polymethylmethacrylate

QCM	Quartz Crystal Microbalance
RIE	Reactive Ion Etching
SAW	Surface Acoustic Wave
SEM	Scanning Electron Microscope
SH-APM	Shear Horizontal Acoustic Plate Mode
SH-SAW	Shear Horizontal Surface Acoustic Wave
SPR	Surface Plasmon Resonance
TCf	Temperature Coefficient of Frequency
TED	Thermoelastic Damping
TIR	Total Internal Reflection
TSM	Thickness Shear Mode
Q-factor	Quality factor
UV	Ultra Violet

SUMMARY

The main objective of this thesis is the performance improvement of microresonators as mass-sensitive biochemical sensors in a liquid environment. Resonant microstructures fabricated on silicon substrates with CMOS-compatible micromachining techniques are mainly investigated in this work, enabling the use of well-established CMOS technologies for sensor array integration in the future.

Two particular approaches have been chosen to improve the resolution of resonant chemical/biochemical sensors. The first approach is based on designing a microresonator with improved Q-factor in air and in liquid, thus, improving the frequency resolution. The second approach is based on minimizing the frequency drift of microresonators by compensating for frequency drifts caused by temperature, thus, stabilizing the resonance frequency of the resonators.

A disk-shape resonant microstructure vibrating in a rotational in-plane mode has been designed, fabricated and extensively characterized both in air and in water. The designed resonators have typical resonance frequencies between 300 and 1,000 kHz and feature on-chip electrothermal excitation elements and a piezoresistive Wheatstone bridge for vibration detection. By shearing the surrounding fluid instead of compressing it, damping is reduced and high quality factors up to 5800 in air and 94 in water have been achieved. The integrated excitation and detection elements enable a closed-loop operation of the disk-type microresonators with frequency stabilities, measured with the Allan-variance method at 1-sec gate time, reaching 1.07×10^{-8} in air and 2.3×10^{-6} in water.

An analytical model, describing the mechanical behavior of the disk resonators, represented by a simple harmonic oscillator, has been derived and compared with experimental results. The analytical expression for the resonance frequency of the disk resonators is obtained by deriving expressions for their effective rotational spring constant and rotational moment of inertia. Besides, an analytical expression for the Q-factor is derived by estimating the energy loss from the viscous damping. In spite of many simplifying assumptions, the developed analytical models show a good agreement with FEM simulation and experimental results and facilitate the geometrical optimization of the disk-type resonators.

A strategy to compensate for temperature induced frequency drifts of resonant microstructures has been developed. The compensation method is based on a controlled stiffness modulation of the resonator by an additional feedback loop and extracting the relative Q-factor changes caused by temperature variations. The developed method is experimentally verified by compensating for frequency fluctuations of a microresonator induced by ambient temperature changes. In principle, the proposed method is applicable to all resonant microstructures featuring excitation and detection elements.

Finally, the application of the designed resonator as a biological sensor in liquid environment has been demonstrated experimentally using the specific binding of anti-β-galactosidase antibody to β-galactosidase enzyme covalently immobilized on the resonator surface. The resonator showed stable responses upon expoure to the antibody solution, giving an approximately 1 kHz frequency change when 0.36 ng antibody is injected.

CHAPTER 1

INTRODUCTION

The demand for chemical and biological sensors has been growing during the past decades especially in the fields of medical and diagnostic industries, environmental monitoring for public safety and security, industrial process control and scientific research. The chemical sensor market in the US has expanded at an annual growth rate of 8.6% during the years from 2001 to 2006 [1] and is expected to expand continuously in the future mainly driven by medical and diagnostics applications.

Despite the relatively high growth rate of the chemical/biochemical sensor market, the majority of chemical analyses are still relying on expensive laboratory analysis with bench-top instruments. These are highly selective and sensitive, but the analyses are done off-line and typically time and labor intensive, thus limiting their applications. Therefore, cost effective, highly sensitive chemical/biochemical sensors with continuous in-situ monitoring ability are in great demand.

From this point of view, micromachined chemical and biochemical sensors, which exploit well-established industrial semiconductor fabrication processes, are one of the most promising candidates. Compared to other competing technologies, low power consumption, small sensor and sample volumes, fast response times, excellent manufacturing/process repeatability and mass production capability with high production yield are strong advantages of microsensor technology.

Among other possible transduction mechanisms for microsensors, mass-sensitive resonant sensors have been widely investigated for chemical/biochemical sensing applications [2-6]. In addition to their high mass-sensitivity, any chemical species that binds to the sensor surface can be detected. Moreover, the frequency output of the

resonant sensor makes it insensitive to variations in signal amplitude and can be easily digitized by use of simple counters. Even though mass-sensitive devices have shown a high sensor resolution in air, a substantial degradation of their performance has been observed in liquid environment and must be overcome to broaden their application as a biological sensor. For this reason, substantial research efforts have been exerted to enhance the mass-sensitive sensor resolution in water-based solutions.

1.1 Silicon Based Resonant Chemical Sensors

The successful commercialization of MEMS (microelectromechanical systems) sensors is undoubtedly related to the use of microfabrication technologies borrowed from the semiconductor industry for (high-volume) manufacturing and also to the possibility of monolithic integration of electronic components with the transducer elements. Considering the recent demand for miniaturized biochemical sensors with multi-analyte sensing capabilities, microsensor arrays integrated on a common silicon substrate are promising candidates to meet these needs.

Besides its excellent electrical properties as a semiconductor material, single crystalline silicon (SCS) has attractive mechanical properties that make it a good material choice for resonant biochemical sensors. These include a linear stress-strain relation, the absence of a mechanical hysteresis, the robustness to mechanical fatigue, and high piezoresistive coefficients for converting mechanical vibrations into an electrical signal.

In case of resonant mass-sensitive sensors, the mechanical resonance frequency of a microresonator changes in proportion to the mass loading. Because of the small mechanical mass of the resonator, inherited from the small size of the vibrating microstructure, an excellent mass-sensitivity is generally achieved. With a proper coating on the resonator surface, such resonant microstructures can be used as chemical/biochemical sensors. In particular, silicon cantilevers have been widely

investigated as a mass-sensitive sensor platform, because of their simple structure and well-defined mechanical characteristics. Combined with high mechanical Q-factors of up to 1000 in air, minimal detectable mass changes in the pico-gram range and below are feasible in a gaseous environment [7]. However, the out-of-plane vibration characteristic for cantilever-based resonators experiences a high viscous damping in liquid environment, thus lowering the Q-factor and mass resolution [8]. To overcome this challenge, an optimization of the resonant microstructure and a proper choice of the resonance mode are indispensable in order to reduce the vibration loss in liquid environment.

Besides the above-mentioned limitations related to the microstructure's Q-factor, the resonance frequency drift caused by mechanical stiffness changes is another drawback of resonant sensors and limits their effective mass-detection resolution. Mechanical stiffness variations from various environmental effects, such as temperature and humidity, are the main cause of this resonance frequency drift. Without successful compensation for these environmental influences, a high sensor resolution and, thus, a successful commercialization of resonant chemical/biochemical sensors are hard to achieve.

1.2 Outline of Thesis

The main objective of this thesis is the performance improvement of microresonators as mass-sensitive biochemical sensors in a liquid environment. Resonant microstructures fabricated on silicon substrates with CMOS-compatible micromachining techniques are mainly investigated in this work to be able to benefit from well-established CMOS technologies for sensor array integration in the future.

After the introduction, MEMS-based sensor technologies for chemical and, in particular, biochemical sensing applications are briefly reviewed and compared in Chapter 2. The discussion includes calorimetric, chemomechanical, optical and

electrochemical sensors. In Chapter 3, the rotational in-plane mode resonator, investigated in this work, is introduced and the design layout for electrothermal excitation and piezoresistive detection of in-plane vibrations is detailed. Finally, the fabrication process developed to implement the designed resonator structure is explained. The characteristics of the designed resonator in terms of Q-factor, short-term frequency stability, and temperature coefficient of resonance frequency are presented in Chapter 4. In an attempt to understand the mechanical behavior of the designed disk-type resonator more clearly and to optimize its structural dimensions with respect to the sensor resolution, an analytical model has been developed and is discussed in Chapter 5. The analytical models for the resonance frequency and Q-factor of the resonator are compared with experimental results and finite element simulations. Chapter 6 introduces a temperature compensation method based on a controlled stiffness modulation by a feedback loop. Along with the concept of the proposed compensation method, a mathematical analysis and experimental results are included in this chapter. Initial performance tests of the designed resonator as a biological sensor are executed using specific antigen-antibody binding and presented in Chapter 7. To this end, β-galactosidase enzyme is immobilized on the resonator surface as a sensitive layer and the mass loading by anti-β-galactosidase antibody binding is monitored by measuring the resonance frequency of the resonator. Finally, the research results are summarized in Chapter 8.

1.3 Major Results

In-plane Mode Disk Resonator

A novel resonant microsensor platform for chemical and biological sensing applications in gaseous and liquid environment is designed and fabricated. The disk-

shape microstructure is operated in a rotational in-plane mode with typical resonance frequencies between 300 and 1,000 kHz. By shearing the surrounding fluid instead of compressing it, the damping is reduced and high quality factors are achieved. The resonators feature electrothermal excitation elements and a piezoresistive Wheatstone bridge for vibration detection, sensitive only to the desired in-plane rotational vibration mode. Microresonators with different dimensions have been fabricated and extensively characterized, achieving quality factors up to 5,800 in air and 94 in water. Short-term frequency stabilities obtained from Allan-variance measurements with 1-sec gate time are as low as 1.07×10^{-8} in air and 2.3×10^{-6} in water.

Analytical Modeling of Disk Resonator

An analytical model describing the mechanical behavior of the disk resonators, represented by a simple harmonic oscillator, is derived for the optimization of the resonator geometry. The resonance frequency of the disk resonators is determined by deriving analytical expressions for their effective rotational spring constant and rotational moment of inertia. The resonance frequencies extracted from the analytical expressions are in good agreement with both numerical FEM results and experimental results. An analytical expression for the Q-factor is also derived by estimating the energy loss from the viscous damping and compared with experimental results. Even though only viscous damping is considered in this model, the analytical model provides a valuable upper limit for the Q-factor of the designed disk resonator.

Temperature Compensation

A strategy to compensate for frequency drifts caused by temperature changes in resonant microstructures is developed. The compensation method is based on a controlled stiffness modulation of the resonator by an additional feedback loop and extracting the

relative quality factor change caused by temperature. The developed method is experimentally verified by compensating for frequency fluctuations of a microresonator induced by ambient temperature changes. The proposed method is applicable to all resonant microstructures featuring excitation and detection elements and insensitive to the temperature dependence of the excitation and detection principles.

Bio-Molecular Sensing in Liquid Environment

The application of the developed disk resonator as a biological sensor in liquid environment is demonstrated by specific binding of anti-β-galactosidase antibody to covalently immobilized β-galactosidase enzyme on the resonator surface. With short-term frequency stabilities of the disk resonators as low as $1.07 \; 10^{-8}$ in air and $2.3 \; 10^{-6}$ in water, mass detection limits in the low femtogram and low picogram are expected in air and in liquid, respectively.

CHAPTER 2

CHEMICAL AND BIOLOGICAL SENSOR TECHNOLOGIES

Micromachined chemical/biochemical sensors typically consist of a sensitive layer and a transducer, converting changes in the physicochemical properties of the analyte specific sensing layer into a signal, generally an electrical signal. Upon exposure to a specific chemical species, the physicochemical properties of the sensitive coating, such as mass, optical properties, resistance, enthalpy and potential, are changed by absorption/adsorption of analyte, chemical reaction, charge transfer, etc [5, 9, 10].

A variety of biochemical sensors have been devised based on different transduction principles, and they are generally classified into four main categories according to their transduction mechanism [10, 11] : i) thermal (calorimetric) sensors, ii) chemomechanical (mass-sensitive) sensors, iii) optical sensors and iv) electrochemical sensors. Each sensing mechanisms has its particular advantages and disadvantages with respect to the sensitivity, selectivity, resolution, manufacturing cost, robustness to disturbances, etc.

The four transduction principles and the characteristics of each sensor type are reviewed and compared in this chapter, with special emphasis on biochemical sensors operating in liquid environment. However, it should be noted that comparing a wide variety of biochemical sensors is difficult and rather subjective because some of the limitations of each sensor technologies can be overcome by building sensor arrays, in which multiple selective layers are used [11].

2.1 Calorimetric Sensors

Thermal or calorimetric sensors determine the presence or concentration of a chemical by measuring the enthalpy changes caused by the absorption or desorption of analyte molecules in the sensitive layer. These enthalpy changes (liberation or abstraction of heat to/from their surroundings) cause temperature variations, which can be transduced into an electrical signal. As an example, the reactant concentration can be determined by measuring the temperature difference between a chemically active area and an inactive area. To achieve high sensitivity with a calorimetric sensor, the sensing area has to be thermally isolated from the surroundings as much as possible and, therefore, the sensing area is generally placed on thermally insulated micromachined structures. The temperature change caused by a chemical reaction is transformed into an electrical signal e.g. by a platinum resistance thermometer (catalytic thermal sensor) or a thermocouple (thermoelectric sensor) [5, 12].

2.1.1 Catalytic Thermal Sensors

Catalytic thermal sensors measure the heat produced by the controlled localized combustion of flammable gaseous compounds on a hot catalyst (e.g., Pt or Pd) surface through resistance thermometers. By flowing electrical current through the heater, the catalyst surface is heated up to a temperature sufficient for oxidizing the combustible gas mixture catalytically. The heat of oxidation is then measured by a resistance thermometer. These catalytic thermal sensors are typically used for detecting flammable gases such as methane, butane, hydrogen, carbon monoxide, propane or propylene in gaseous environments [13, 14] with the following typical detection limits: hydrogen $\approx$ 13 ppm, carbon monoxide $\approx$ 32 ppm, propane $\approx$ 14 ppm, and propylene $\approx$ 8 ppm [14]. Catalytic sensors generally suffer from a poor selectivity and their application in liquid environment is not reported yet.

8

2.1.2 Thermoelectric Sensors

Thermoelectric sensors based on the Seebeck effect measure temperature variations by means of a thermovoltage, which is proportional to the temperature difference between a hot and a cold junction. In these sensors, the hot junctions are typically located on a (micromachined) membrane or bridge that is coated with a sensitive layer liberating or abstracting heat upon interaction with an analyte, while the cold junctions are on the bulk substrate featuring a high thermal conductivity. In CMOS-based thermoelectric sensors, polysilicon/aluminum thermocouples are generally used [12, 15] and several thermocouples are commonly connected in series to increase the thermovoltage. Their application in detecting organic volatiles in the gas phase and measuring concentrations of glucose, urea and hydrogen peroxide in the liquid phase has been demonstrated [16, 17]. A sensitivity of $53.5\,\mu V/M$ for glucose, $26.5\,\mu V/M$ for hydrogen peroxide and $17\,\mu V/M$ for urea with a 2 mM detection limit for glucose in a continuous flow mode has been reported with the use of polysilicon-Au thermopile-based sensors with integrated microfluidic channels [17].

2.2 Chemomechanical Sensors

Chemomechanical sensors determine an analyte concentration by monitoring mechanical property changes of the sensor, such as its mass, elastic modulus and deflection, when chemical species are accumulated in a sensing layer. Among others, the static beam bending and mass loading are most commonly used as a measure of the analyte concentration. Depending on the mode of sensor operation, chemomechanical sensors are generally classified as either static or dynamic mode sensors.

2.2.1 Static-Mode Sensors

Static-mode chemomechanical sensors determine the analyte concentration by measuring the deflection of a microstructure (generally a microcantilever) due to chemically induced surface stresses. For use as chemical sensors, the microstructures are typically modified so that one surface is passive while the other surface exhibits a high affinity to the target analyte. The relation between the deflection and the chemical molecular absorption/adsorption is generally explained by three distinctive mechanisms [18]. When the sensitive coating is very thin, e.g. a monolayer, compared to the thickness of the microstructure, spontaneous adsorption processes driven by an excess of interfacial free energy result in the reduction of the interfacial stress and, thus, expand the surface. On the other hand, if a thick analyte-permeable coating is used, the predominant mechanism of deflection is the analyte induced swelling of the coating. A third deflection mechanism combines bulk, surface and intersurface interactions and is most relevant to nanostructured coatings. Grain boundaries, voids, and impurities of nanostructured coatings generate high intrinsic stresses resulting in up to two orders of magnitude increase in cantilever deflection when receptor molecules are immobilized on a nanostructured surface [18]. However, deflections of cantilevers with nanostructured coating cannot be accurately predicted using current analytical models. The static mode detection method has been used for detecting various biochemical species in the liquid phase, such as glucose [4], myoglobin [19], complementary strands of oligonucleotides [20] and prostate-specific antigen (PSA) [21], showing sensor resolutions of 0.2 ng/ml for the prostate-specific antigen (PSA) and 20 μg/ml for myoglobin.

2.2.2 Dynamic-Mode Sensors

Dynamic-mode sensors assess an analyte concentration by measuring the frequency change of a resonating structure or a traveling acoustic wave upon mass loading and are

often called resonant sensors. The frequency output of resonant sensors is insensitive to variations in the signal amplitude, signal drift, and bias and can be easily digitized by the use of a counter. The obtainable dynamic range is limited only by the sensor principle itself but not by the analog-to-digital conversion [22]. Because these advantages are common to all resonant sensors, they have attracted increasing interest in recent years.

The first class of dynamic-mode mass-sensitive sensors, the so called acoustic wave devices, are largely classified as bulk acoustic wave (BAW) devices and surface acoustic wave (SAW) devices depending on the modes of wave propagation through or on a substrate [22, 23]. The most common BAW and SAW devices and their vibration modes are summarized in Figure 2.1.

TSM   SH-APM

Rayleigh Wave SAW   SH-SAW / Love Wave   Lamb Wave FPW
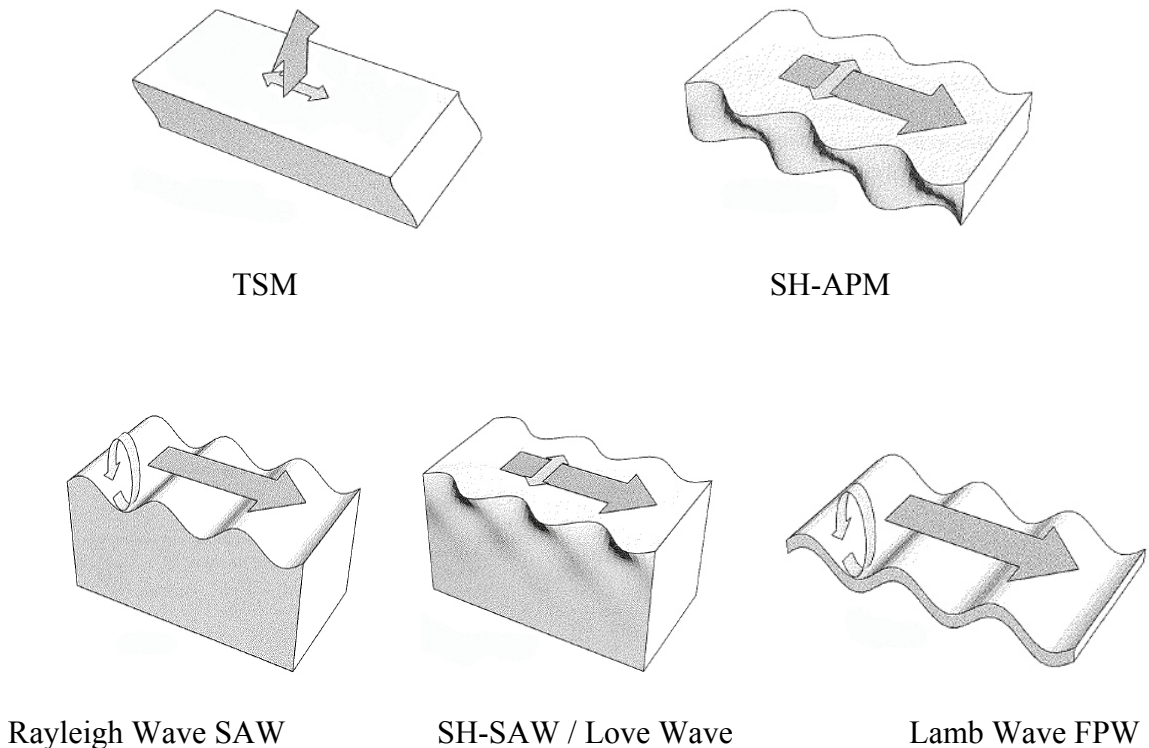
Figure 2.1: Wave propagation of acoustic wave devices [24].

The most common bulk acoustic wave devices are the thickness shear mode (TSM) resonator and the shear horizontal acoustic plate mode (SH-APM) resonator where the acoustic wave propagates through the substrate. The TSM, widely referred to as a quartz crystal microbalance (QCM), benefits from its simplicity of fabrication and a good temperature stability. Because of their shear wave propagation, QCMs show high quality factors (Q-factor) in water with typical values better than 1000 [25]. However, these devices typically show the lowest sensitivities among the acoustic wave devices. SH-APM devices use a thin piezoelectric plate whose thickness is in the range of 10 wavelengths of an acoustic wave [26]. The advantage of these devices is that the generated shear waves do not radiate acoustic energy into adjacent liquid media because of the absence of a surface-normal component of the displacement. As both surfaces undergo displacement, detection can occur on either side. Therefore, the inter-digitated transducers (IDT) generating and detecting the acoustic waves can be separated from the (conducting) fluids or gases while the other side can be used as the sensing area. Although more mass-sensitive than the TSM, SH-APM devices show lower sensitivities than the SAW resonators because the acoustic wave energy is not maximized at the sensing surface.

Surface acoustic devices utilize acoustic waves that propagate on the surface of their substrates. Rayleigh-wave surface acoustic wave (SAW), shear-horizontal surface acoustic wave (SH-SAW), Love wave and flexural-plate wave (FPW) devices belong to this category [22].

Rayleigh-wave SAW devices show a high mass sensitivity because all the acoustic energy is confined to within one wavelength of the surface. However, the surface normal velocity components of Rayleigh waves make them inadequate for liquid phase sensing, because the compressional waves cause an excessive attenuation of acoustic energy.

SH-SAW devices are very similar to the Rayleigh wave SAW devices, but if the cut of the piezoelectric crystal material is rotated appropriately, the wave propagation mode

changes from the Rayleigh waves to shear-horizontal surface waves. The appearance of these devices is similar to that of Rayleigh wave SAW devices, but a thin solid film or grating is often added to prevent wave diffraction to the bulk [27]. As the particle displacements on the surface of these devices are transverse to the wave propagation direction and parallel to the plane of the surface, the wave propagation is not severely attenuated when liquids come in contact with the propagating medium, allowing the SH-SAW sensor to operate in liquid environment.

Love-wave devices, a special class of the SH-SAW, have an additional wave guiding layer on top of the piezoelectric substrate and the IDTs are located at the interface between the substrate and the guiding layer. In Love-wave devices, the acoustic wave energy is concentrated in the guiding layer allowing high mass-sensitivities to be achieved. The Love-wave devices show the highest mass-sensitivity amongst acoustic wave sensors based on quartz substrates, but are less sensitive than FPW devices based on silicon substrates [26, 28].

Flexural-plate wave (FPW) devices feature plates that are only a fraction of an acoustic wavelength thick (typically 2~3μm). When the plate thickness is reduced to less than the acoustic wavelength, Lamb waves, consisting of two Rayleigh waves propagating on each side of the plate, are created with typical frequencies in the MHz range. The confinement of acoustic energy to the thin plate results in the highest mass sensitivity of all acoustic wave sensors. As the velocity of the flexural wave is significantly slower than the velocity of sound in liquid, the acoustic wave is not severely damped in liquid media, thus enabling its application to biochemical sensing in liquid environment. Another important advantage of FPW devices is that they can be fabricated using CMOS-compatible micromachining technologies on a silicon substrate, which enables easy integration of electronic circuitry with the acoustic wave devices [26]. However, the thin membrane structure paired with its low heat capacity makes FPW

devices sensitive to differential pressures on each side of the membrane and to temperature variations [29].

Table 2.1 summarizes features of the different acoustic wave devices discussed so far. The sensitivity of the acoustic wave sensor in this table is defined as relative frequency change per mass loading on a unit surface area.

Table 2.1: Comparison of the most common acoustic wave devices [23, 24, 26, 27]; sensitivity is defined as relative frequency change per mass loading on a unit surface area.

Device Type		Typical Substrate	Frequency [MHz]	Sensitivity [cm^2/g]	Operating Media
BAW	TSM	Quartz	5~10	14	gas/liquid
	SH-APM	Quartz Lithium Niobate	25~200	15	gas/liquid
SAW	Rayleigh	Quartz	30~300	133	gas
	SH-SAW	Lithium Tantalate	30~300	180	gas/liquid
	Love Wave	SiO_2 guiding layer on Quartz	30~300	221	gas/liquid
	FPW	ZnO on SiN_X	5~20	450	gas/liquid

The second class of dynamic-mode mass-sensitive sensors is characterized by the fact that a resonant microstructure is used as a sensing platform. The absorption of an analyte in a chemically sensitive layer causes a shift in the microstructure's resonance frequency, a consequence of changes in its oscillating mass. Spurred by extensive research on the fabrication and characterization of AFM probes, microcantilevers have been most extensively used as mass-sensitive transducers for chemical and biological sensors. Microcantilevers can be easily fabricated with industrial CMOS

(Complementary Metal Oxide Semiconductor) processes in combination with post-processing micromachining steps to release the microstructure. This enables the integration of signal conditioning and processing circuitry with different transducers or sensor arrays, yielding a better quantitative and discriminative chemical sensing ability than a single device sensor. More details on cantilever type resonant sensors can be found in Chapter 3. With the mass of the micromachined silicon resonator on the order of 10^{-9} ~ 10^{-6} g, minimal detectable mass changes of less than 1 pg are feasible at atmospheric pressure. Typical applications include the detection of organic volatiles in the gas phase using polymer coatings [7, 12, 15], but also biosensing in liquid to detect, e.g., avidin, biotinylated bovine serum albumin (bBSA) [6], and E-coli [2].

2.3 Optical Sensors

Optical chemical/biochemical sensors relate the modulation of a transducer's optical characteristics to chemical/biomolecular interactions on the sensor surface. Analyte-induced dielectric constant changes of the material in the sensing region modulate the propagation constants of light. Changes in the real part of the dielectric constant, which are related to the reflective surface properties, modulate the speed of light propagation. On the other hand, changes in the imaginary part of the dielectric constant, which are related to absorption losses in the medium, result in the attenuation of the light propagation. Surface plasmon resonance (SPR) and interferometric sensors are based on the real part of the dielectric constant, while luminescence sensors are based on the imaginary part of the dielectric constant [30]. Sensors based on the change in the imaginary part of the refractory index are typically less sensitive and selective than those that are based on the real part of the dielectric constant [31].

Chemically-induced optical property changes of a wave-guiding layer are assessed by means of an evanescent wave. When a light beam has an incident angle exceeding the

critical angle, a total internal reflection (TIR) occurs at the interface and, as a consequence, the light traveling inside the waveguide, is confined within the structure. Even though the light is confined inside the waveguide, its intensity does not abruptly decay to zero at the interface and a small fraction of the light penetrates into the reflecting medium by a fraction of a wavelength [31, 32]. This electromagnetic wave, called the evanescent wave, can interact with molecules within the penetration depth. The resulting transfer of energy modulates the refractive index of the medium in response to the chemical reaction on the waveguide surface. As the evanescent wave decays exponentially from the surface, the most sensitive detection is just at the transducer surface and, thereby, any changes in the bulk properties of the surrounding fluid will hardly affect the sensor response, making evanescent wave sensors highly selective and sensitive. Surface plasmon resonance sensors, grating couplers, Mach-Zehnder interferometers, and difference interferometers are sensor types based on evanescent wave transduction schemes with different respective methods of evanescent field generation.

The classification of optical chemical/biochemical sensors into a few types is difficult because of the wide variety of sensing schemes. The approach adopted in [31] is used here, classifying optical sensors into three main categories: fiber optical (FO) sensors, surface plasmon resonance sensors, and integrated sensors using planar/channel waveguides.

2.3.1 Fiber Optic Sensors

Fiber optic (FO) biochemical sensors are based on the transmission of light along a fiber strand under total internal reflection (TIR) conditions. Different types of spectroscopic techniques, e.g. absorption, fluorescence, phosphorescence, Raman, or surface plasmon resonance (SPR) are used in fiber optic sensors [32]. These sensors are usually classified into two main groups: extrinsic and intrinsic [31, 32]. In case of

16

extrinsic sensors, the optical fiber is used only for guiding light to and from the sensing region. As the immobilized sensing layer is attached to the optical fiber externally, they are called extrinsic optical fiber sensors. Reflected, scattered or emitted light returning from the sample is interpreted at the detector as a measure of the analyte concentration. Intrinsic fiber optic sensors usually use a tapered, fused-silica fiber and the interaction with the analyte occurs within a section of the optical fiber, which is usually done by directly immobilizing chemical receptors after decladding the optical fiber core. Optical fiber based biochemical sensors have several advantages including: i) light can be transmitted over a long distance without severe loss through the optical fiber, thus enabling remote monitoring of chemical species, ii) the sensing principle is immune to electromagnetic interference at the sensing site and can be used in harsh environments, iii) multiple analyte detection or single analyte monitoring at different locations is possible because FO sensors can guide light of multiple wavelengths at the same time and in different directions, and iv) multi-wavelength measurements can be used to improve sensor selectivity (using spectroscopic techniques) and correct for drift in optical and electrical components.

2.3.2 Surface Plasmon Resonance Sensors

The first application of surface plasmon resonance (SPR) in gas sensing and biosensing of an antigen-antibody interaction was demonstrated by Nylander and Liedberg in 1983 [33] and since then SPR has become a well-established method for biochemical sensing [31]. The plasmon is a collective oscillation of a free electron gas resulting from the quantization of plasma oscillations [34]. Surface plasmons are those plasmons that are confined to surfaces interacting strongly with light. Surface plasmon resonance (SPR), a quantum optical-electrical phenomenon, is caused by charge-density oscillations that may exist at the interface of two media with dielectric constants of opposite signs, for instance, a metal and a dielectric [31, 32, 35]. At a certain wavelength

and at a specific incident angle of light, called the angle of resonance, which is greater than the TIR angle, surface plasmons in the conducting film resonantly couple with the light. Both the energy and momentum of the photons must match exactly the energy and momentum of the plasmons to excite surface plasmon resonances. These resonance conditions can be satisfied either by adjusting the incident angle or the wavelength of the incident light. Any change in the chemical composition of the environment within the range of the plasmon electrical field (typically about 100 nm above and below the metal surface) causes a wavelength change of light that resonates with the plasmon. Two detection schemes are usually employed: i) the incident angle is swept until resonance is observed as a dip in the reflective curve while the wavelength is fixed, or ii) the wavelength is swept until resonance is observed while the incident angle is fixed. There are three general methods that can alter the momentum of photons in a way that meets the resonance criterion: i) total internal reflection inside a prism coupler (Kretschmann configuration), ii) diffraction at a grating (grating coupler), and iii) diffraction inside a wave guide (waveguide-based SPR) as shown in Figure 2.2.
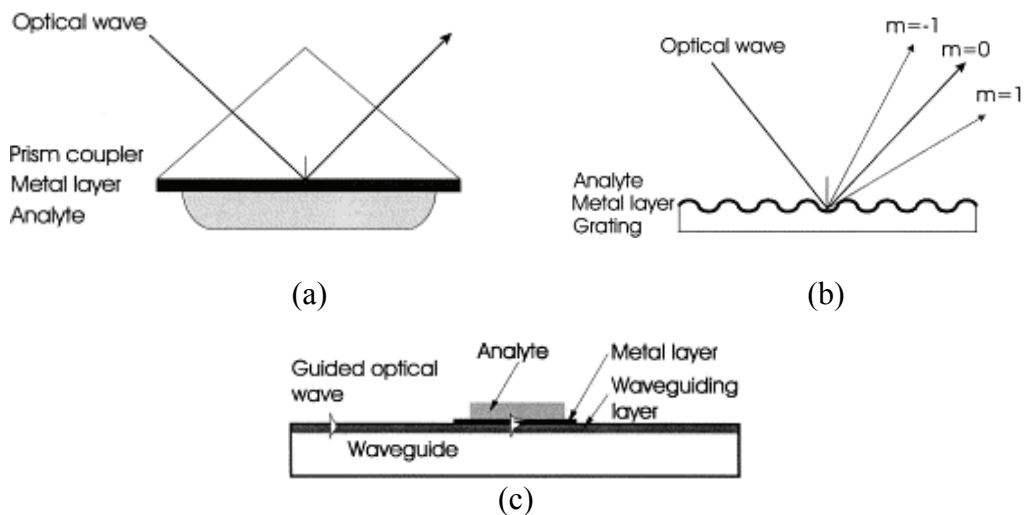
Figure 2.2: Configurations of SPR sensors: (a) prism coupler-based SPR system; (b) grating coupler-based SPR system; (c) waveguide-based SPR system [35].

The Kretschmann geometry (bulk prism coupler) based on attenuated total reflection (ATR) is the most widely used configuration in SPR sensors. The use of high quality bulk optics allows for the development of SPR sensors with refractive index resolution better than 3×10^{-7} RIU (Refractive Index Unit) [35]. As an attempt to use this SPR sensing technique for compact, mobile and cost effective sensing devices, integrated ATR-based SPR sensor systems are developed with several modifications to the optical system, light source and SPR probes. The resolution achieved with these integrated sensors is up to 1×10^{-5} RIU [35].

In the grating coupler configuration, the metal-dielectric interface is periodically distorted as shown in Figure 2.2(b). The incident optical wave is diffracted forming a series of beams directed away from the surface at a variety of angles that can be coupled to a plasmon wave. As the wavelength of resonance is determined by the period and the amplitude of the grating, a uniform and reliable grating geometry is critical to SPR signal strength and sensor sensitivity. The lower production cost and the wide variety of possible materials make the grating coupler system suitable for high volume production. Resolutions below 1×10^{-6} RIU have been reported with grating coupler based SPR sensor systems [35]. However, the flow cell and samples have to be transparent at the used wavelength, because light should be incident through the sample. The sensitivity and resolution of grating coupler based sensors are lower than that of prism coupler based sensors, regardless of the adopted detection methods.

Waveguide-based SPR sensors combine the resonant coupling of the guided light modes inside a waveguide with SPR at a gold-coated surface. When light incidents the region with a thin metal over-layer, it evanescently penetrates through the metal layer and excites a surface plasmon wave at the outer interface of the metal. The use of optical waveguides provides several benefits such as easy control of the optical path in the sensor system, small size, and ruggedness, enabling multi-channel sensing on one chip with the potential for efficient referencing and multicomponent sensor analysis of complex

19

samples. However, these devices show a rather limited operating range. Various approaches have been used to increase the operating ranges, but they show less sensitivity instead [31].

2.3.3 Integrated Optical Sensors

Integrated optical (IO) sensors are based on planar/channel waveguides and include additional optical components such as gratings, dividers, and combiners, on the same substrate [31]. The design and fabrication of these sensors utilizes microfabrication techniques to integrate multiple components on one substrate. Two main types of integrated optical biosensors, interferometric and grating coupling devices, will be reviewed here.

Interferometric biochemical sensors have a broader dynamic range than any other type of optical sensor and have shown the highest sensitivity. With their intrinsic reference channel, common mode effects such as temperature drift and non-specific adsorption can be compensated. Interferometers are based on the principle that two waves that have the same phase will amplify each other while two waves that have opposite phases will cancel each other, if both waves have the same amplitude. The most common type of interferometer for biochemical sensing is the Mach-Zehnder interferometer (MZI).

In an MZI, light from a monochromatic light source is split at a Y-junction into two identical beams that travel through reference and sensor arms, and is subsequently recombined into a mono-mode channel waveguide as shown in Figure 2.3. When a biochemical reaction happens in the sensing area, only the light traveling through the sensing arm will experience a phase change. Therefore, the light from both arms will interfere with each other, showing a sinusoidal variation of the light intensity at the sensor output that is directly related to the concentration of the analyte to be measured [36, 37].
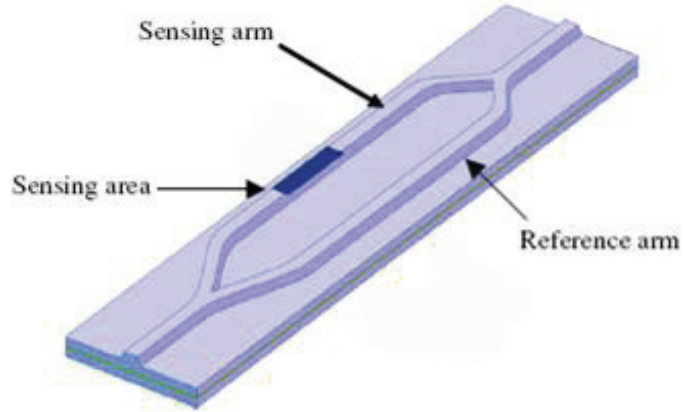
Figure 2.3: Schematic diagram of a Mach-Zehnder interferometer for biochemical sensing applications [36].

To achieve a high sensor resolution, the propagation losses in each arm should be identical and the input light has to be divided equally into each branch. In addition, a mono-mode optical waveguide is essential; otherwise multiple light waves will interfere with each other, producing a high signal noise. A refractive index resolution up to 10^{-6} and detection limits of $1pg/mm^2$ have been achieved with integrated MZI biochemical sensors [35, 36].

Grating coupler based sensors are based on the coupling of light into a thin waveguide by means of a grating coupler covered with a sensing layer. By monitoring the coupling angle, the refractive index change in the sensitive layer caused by a biochemical interaction can be accurately determined. There are two main types of grating coupler based sensors: input grating coupler and output grating coupler sensors as shown in Figure 2.4 [38-40].

In an input grating coupler system, a laser beam is diffracted by the grating and starts to propagate via internal reflection inside the waveguide at a certain incident angle. In the case of an output grating coupler system, a laser beam coupled into a planar waveguide is coupled out by the grating and the outcoupling angle is measured. Typical resolutions of refractive index changes reported with this method are $10^{-6} \sim 2\times10^{-7}$ with

minimum surface mass detection limits around 1~10pg/mm^2 [31]. However, to monitor the reflected radiation, either an angle-resolving arrangement or a CCD camera are required, making the whole system rather complicated [41].
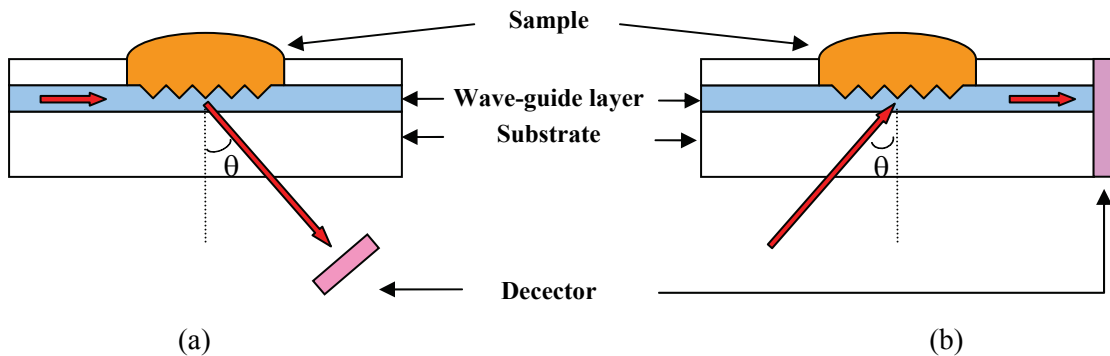
Figure 2.4: Configurations of grating coupler biosensors: output grating coupler (a), and input grating coupler (b).

2.4 Electrochemical Sensors

The oldest electrochemical sensors date back to the 1950s and constitute the largest group of chemical sensors. Typical electrochemical sensors are composed of two electrodes, a sensing and a reference electrode, separated by a chemically sensitive layer. Electrochemical reactions or charge transfer at the electrode surface are transduced into an electrical signal, generally a current, potential or conductance change. Depending on the electro-analytical principles, electrochemical sensors are classified into three categories: potentiometric, amperometric, and conductometric sensors [5, 10, 11, 42].

2.4.1 Potentiometric Sensors

Potentiometric sensors derive the analytical information by measuring the potential of the sensing electrode, which exhibits a logarithmic relation with the analyte

concentration in the sample. The potential measurement is usually done in the mode known as zero current potentiometry. Potentiometric sensors are particularly suitable for miniaturization into a field effect transistor (FET)-based architecture called a chemically sensitive FET (CHEMFET), because the transduced signal that carries the chemical information does not depend on the sensing area. In addition, noise and signal-to-noise ratio do not degrade significantly with miniaturization. Three different types of CHEMFETs can be classified depending on how the physical properties of the gate conductor are chemically modulated: ISFET (ion sensitive FET), ENFET (enzymatically selective FET), and work function FET. Utilizing well-established IC fabrication technologies along with small sensor size, sensor arrays with supporting electronics have been realized to overcome the limited selectivity of individual sensors [43].

The basic structure of the ISFET is similar to MOSFET, but the thin gate insulator is either directly exposed to the ionic medium or through an ion-selective membrane that responds only to certain kinds of ions [5, 44]. The metal gate of the metal oxide semiconductor FET (MOSFET) is replaced by an external reference electrode, while the liquid, in which this electrode is present, is in contact with the bare gate insulator. If the applied reference electrode potential is fixed, generally grounded, the gate potential is determined by the surface potential at the insulator/liquid interface. Therefore, any change of the surface potential from a chemically induced charge accumulation at the gate-surface interface is reflected in a change of the source-drain current. The primary disadvantage of ISFETs is that a large reference electrode is unavoidable for stable operation, limiting their practical application.

The ENFET is another CHEMFET structure without a conducting gate; a chemically sensitive enzyme layer forms either part of or the entire insulation layer of the FET structure. The conversion of a sample in the immobilized enzyme membrane results in a local change in pH, which in turn modulate the gate-source voltage of FET by the surface potential change at the insulation layer. However, potentiometric enzyme sensors

suffer from a nonlinear response caused by two reasons: i) the pH changes in the immobilized enzyme membrane depend on the initial pH of the solution, and ii) the enzymatic reaction of the immobilized enzyme is also pH dependent. Because of this problem, ENFETs have only limited usefulness in biochemical sensing applications [44].

In the case of work function FETs, a chemically selective layer is used as a conductive gate instead of completely removing the metal gate. The FET with a palladium gate is a well known microsensor of this type for the detection of gases such as hydrogen and ammonia. When two chemically different materials are electrically connected via a dielectric layer, the equalization of the Fermi-levels leads to the formation of an electric field in the dielectric layer. This field is proportional to the difference in the work-function of the two plate materials. The work-function change of the gate conductor caused by a chemical reaction modulates the threshold voltage of the FET, and the analyte concentration can be derived. The major advantage of this sensor type over the ISFET and ENFET in realizing miniaturized potentiometric sensors is the absence of a large reference electrode since the fully enclosed silicon is an excellent reference [44].

2.4.2 Amperometric Sensors

Amperometric sensors utilize the fact that if oxidization takes places at the anode and reduction occurs at the cathode, a measurable current is produced by the flow of electrons and ions. With amperometric sensors, the electrode potential is maintained at a constant level sufficient for the oxidation or reduction of the species of interest. It follows that the current flowing is proportional to the analyte concentration. Not only electrochemically reducible or oxidizable materials can be detected on metal electrodes like platinum and gold, but also electrochemically inactive analytes can be sensed indirectly by coating the surface of an electrode with a material that converts the electrochemically inactive analyte into electrochemically active species. For biological

sensing applications, amperometric sensors measure the concentration-dependent current through an electrochemical electrode coated with the biologically active material. The biologically active material, usually an enzyme, oxidizes or reduces the analyte or the enzyme's substrate. This reaction is electrochemically connected to the electrode either directly, through mediator molecules, or by the oxidation or reduction of co-reactant molecules or byproduct molecules. Typical substrates used in amperometric biosensors are glucose, urea, cholesterol, fructose, sucrose and ethanol, as well as tissue and whole organisms. A typical application for this type of biosensor is glucose sensing using immobilized glucose oxidase (GOD) as a biocatalyst [45].

2.4.3 Conductometric Sensors

Conductometric sensors rely on changes in the electric conductivity of a film or a bulk material because of the analyte presence. The analyte concentration can be determined by monitoring either a resistance change (chemoresistor) or a capacitance change (chemocapacitor) between two electrical contacts embedded in a sensitive material.

Chemoresistors are relatively easily and inexpensively fabricated due to their simple layout, but their application is usually limited to non-conducting media such as gases or dielectric liquids. Chemoresistors typically use conducting polymers such as polypyrroles, polyaniline and polythiophene as a sensitive material. Interdigitated electrode configurations are generally adopted to increase their sensitivity, and either DC or low frequency AC currents are used for the conductance measurement. Thereby, AC currents are used to avoid electrode polarization, but any capacitance between the two electrodes will be reflected in the sensor response. The functional relation between the chemoresistor response and the analyte concentration is generally not explicit, making the interpretation of the sensor response rather complicated [44].

Chemocapacitors consist of two electrodes and a sensitive layer coating, and constitute chemically sensitive capacitors. The capacitance change caused by a sensitive layer upon analyte adsorption determines the analyte concentration. In this case, either the dielectric constant or the physical volume of the sensitive layer varies in relation to the measurand. The capacitances are usually measured at frequencies from a few kHz to 500 kHz. Typical relative capacitance changes are around $10^{-3} \sim 10^{-6}$ with analyte concentration in the ppm range. Considering the small nominal capacitance (on the order of 1 pF) of a microfabricated sensor, the sensor output signal is typically weak. Therefore, an integrated solution with on-chip circuitry and reference capacitors (without sensitive layer) is required. Interdigitated electrode structures are predominantly used with chemocapacitive sensors. The sensor signal is highly dependent on the thickness of the sensitive layer and non-uniform sensor coatings can cause irreproducible sensor signals.

2.5 Comparisons of Biochemical Sensor Technologies

Comparing the wide variety of biochemical sensors is difficult and rather subjective because each sensor generally has its own specific requirements depending on its application area. However, a high sensitivity and selectivity, a wide sensing range, a simple and inexpensive fabrication process, and the simplicity of the overall sensing system are common features that every microsensor tries to achieve. In the following, general advantages and disadvantages of each sensor type (calorimetric, chemomechanical, optical and electrochemical sensors) will be compared with regard to the above-mentioned aspects.

Calorimetric biochemical sensors exhibit moderate sensitivity and selectivity and a good operational stability for continuous monitoring, typically limited only by the stability of the adopted sensitive layer. In the case of biological sensing applications, high

selectivities can be achieved by coating the sensor with specific catalysts such as enzymes and antibodies. Even though the sensor signal amplitudes are relatively small (~10's of μV), the high common-mode thermal noise rejection ratio and high heat power sensitivity of thermopile-based sensors enabled their application in a broad range of biochemical sensing areas. However, thermal sensors detect enthalpy changes during analyte absorption/desorption and, thus, are sensitive to analyte concentration changes only. In contrast to mass-sensitive, optical or electrochemical sensors, no output signal is generated at thermodynamic equilibrium [12, 46]. Furthermore, thermal sensors typically rely on a thin fragile membrane with a high thermal resistance to improve their sensitivity. In a liquid sensing environment, the sensitivity is often lowered because of the high thermal conductivities of the surrounding fluid and the sensor package.

Optical biochemical sensing approaches offer many advantages, including high sensitivity and low detection limit with, e.g., refractive index resolutions on the order of 10^{-5}~10^{-7} and limits of detection 0.1~10 pg/mm^2 [37]. Even more important, the use of spectroscopic sensing schemes generally provides excellent sensor selectivity. In addition, remote analyte monitoring and multiple analyte analyses have been shown to be feasible with, e.g., fiber optic sensors. With these attractive features as well as fast response times, optical sensors have been used and commercialized for a number of biological and chemical sensing applications. However, optical biochemical sensors also have certain drawbacks, including i) interference from ambient light, ii) background absorbance or scattering due to inhomogeneities, iii) limited stability caused by photobleaching of the immobilized sensing layer, iii) narrow dynamic range, iv) high sensitivity to temperature changes and minor alterations in the buffer solution (especially for evanescent field methods), and v) signal drift caused by the instability of the light source or aging of the detector. The main disadvantage of this class of devices is, however, their system complexity and the difficulty in integrating all optical components, including high quality monochromatic light sources, monomode waveguides and

27

detectors, onto a single substrate. As a result, the optical sensing system in general and spectroscopic system in particular are still expensive and rather bulky [31].

Today, electrochemical sensors are one of the most commercially successful type of chemical and biochemical sensor, mainly because of their simple structure and relatively easy and inexpensive fabrication processes. However, the long term stability of these sensors is typically not sufficient for continuous monitoring of analyte concentrations because of electrode fouling and the degradation of the chemically selective membranes along with surface oxidation of the metal electrodes. Coupled with a poor sensor selectivity and parasitic capacitance effects between the electrodes, the functional relationship between sensor response and analyte concentration is generally not explicit. Therefore, the interpretation of the sensor response is rather complicated and generally requires extensive calibration and frequent recalibration. Moreover, the sensor signal is highly dependent on the quality of the sensitive layer, e.g. its thickness and surface morphology, thus causing irreproducible sensor responses.

Chemomechanical sensors are based on two distinctly different sensing approaches, measuring either the deflection of a cantilever (static-mode) or the frequency change of a resonant sensor (dynamic-mode), as mentioned before. Even though these two sensor types are classified into same category, they have quite different characteristics when used as biochemical sensors. Therefore, the advantages and disadvantages of each sensor type are discussed separately here.

Chemomechanical sensors based on static mode detection (SMD) mostly use a thin cantilever as the transducer element. Because of their simple structure and their well-defined mechanical behavior, cantilevers have been widely investigated as a chemical sensing platform. They have shown good selectivity as well as high sensitivity with limits of detection as good as 10~30 ppt levels of pentaerythritol tetranitrate (PENT), which corresponds to a few femto-grams mass loading in air [47]. SMD-type sensors can be operated in vacuum, gases and liquids. However, the exact mechanism of the analyte-

28

induced deflection is not well understood yet and the sensors show long response times compared to other chemical sensing methods. Additionally, low signal-to-noise ratios, temperature-induced drifts, and sensitivity to external vibration are other disadvantages. The main drawback of static mode detection sensors is caused by the fact that a precise and accurate measurement of cantilever deflection is mandatory to achieve high sensor resolution as the chemically induced cantilever deflection is usually very small (typically in the range of 1~100nm). As a consequence, optical methods have been most extensively used for measuring the deflection, with achievable deflection resolutions down to 10^{-14}m ranges [18]. The optical readout is mostly based on external components, making the overall sensing system expensive and requiring proper alignment of the cantilevers with the optical system. In case of liquid-phase sensing, other drawbacks are change of the output signal by optical properties changes of the medium, the requirement for transparent media, and a minimum required reflecting area, thus limiting the application of SMD devices as biochemical sensors.

Mass-sensitive dynamic mode sensors have several attractive features including: i) high mass-sensitivity, ii) easy signal digitization using counters instead of A/D (analog-to-digital) converters, iii) wide dynamic range, iv) small size with on-chip actuation and sensing elements, v) a relatively simple fabrication process, vi) fast response time, and vii) robustness to external vibrations.

Some acoustic wave devices, especially the QCM, have high Q-factors both in air and in liquid environment, thus showing excellent frequency stabilities. But as most acoustic wave devices are fabricated on piezoelectric substrates, monolithic integration of electronic circuits is not feasible. The necessary circuits are added only in a hybrid fashion and this restricts the implementation of sensor arrays, required for improved sensor selectivity and multi-analyte detection capability in biochemical sensor applications. Due to their high resonance frequencies (typically 5~300 Mhz), these

sensors generally suffer from a higher aging rate, a higher background noise floor and higher power consumption of the associated digital circuitry [48, 49].

On the other hand, silicon-based resonant microsensors (mostly cantilever sensors) have several advantages over acoustic wave sensors, such as CMOS compatible fabrication processes, enabling the co-integration of data processing and self testing circuitry, small size and low power consumption, and the feasibility of sensor arrays coated with application specific sets of chemosensitive membranes. However, their resonance frequency is susceptible to thermally induced noise coming from temperature fluctuations in the surrounding environment, and the resulting frequency drift generally limits the resonant sensor's resolution. Moreover, changes in the viscosity or density of the medium also affect the resonance behavior, such as the resonance frequency and Q-factor, of the microsensors. While resonant cantilever sensors exhibit excellent performance in air, their operation in liquid media is challenging due to the associated high viscous damping. High viscous damping results in a reduced Q-factor and frequency resolution of the resonant sensor.

The sensor resolution of each sensor type discussed so far is summarized in Table 2.2. The limit of detection (LOD) of different sensors to several gases is used for comparison because both sensor sensitivity and background noise floor are reflected in the LOD. From a practical point of view, the LOD is more important than the sensor sensitivity for a particular chemical sensing application. Finally, Table 2.3 summarizes the characteristic properties of each chemical sensor type discussed in this chapter.

30

Table 2.2: Comparison of gas-phase chemical sensors in terms of limit of detection.

Unit: ppm

Sensor Analyte	Thermal	Chemomechanical		Optical	Electrochemical	
		AW	Cantilever		CHEMFET	Capacitive
Toluene	40-50 [12]	0.7-5.5 (FPW) [50]	1-2 [12]	0.01-16 [30]	1-40 [51]	5-55 [12, 52]
Benzene		1.1-13 (FPW) [50]		0.13-78 [30]		85 [52]
Ethanol	100-150 [12]		10-12 [12]		10-50 [51]	3-5 [12]
Ammonia				0.04-540 [30]	25 [53]	
H$_2$S		1-10 (SAW) [49, 53]			10 [53]	
NO$_2$		0.5-1 (SAW) [49, 53]			3 [53]	
Octane		1.5 (TSM) [7] 7 (SAW) [7]	2.5 [7]			29 [52]

Table 2.3: Summary of the properties of biochemical sensors.

Sensing Principle		Resolution	Overhead	Power	Advantages	Disadvantages
Thermal		Moderate	Low	Moderate	Operational stability for continuous monitoring. High thermal noise rejection ratio.	Only detect changes of analyte concentration. Sensitive to thermal conductivity of medium.
Chemomechanical	Static	High	High (optical sensing) Low (piezo-resistive sensing)	Moderate	High sensitivity. Operation in liquid.	Long response time. Low signal-noise ratio. Complicated/expensive optical equipment.
	Dynamic	High	Low	Moderate	High sensitivity and wide dynamic range. Simple fab. process. Fast response time.	Sensitive to thermal noise. Low resolution in liquid.
Optical		High	High	High	High sensitivity. High selectivity due to spectroscopic methods. Multi-analyte sensing. Fast response time.	Complicated/expensive sensing system. Photobleaching of sensitive layer. Signal drift by ambient temp., light, and unstable light source/detector.
Electrochemical		Moderate	Low	Moderate	Simple structure. Inexpensive fab.	High background noise floor. Sensitive to the quality of sensing layer.

CHAPTER 3

RESONANT MICROSTRUCTURE: DESIGN AND FABRICATION

3.1 Introduction

Benefiting from well-established semiconductor microfabrication technologies, micrometer or sub-micrometer sized silicon resonators can be fabricated with standard industrial batch processes, enabling mass production of mechanical resonators with high production yield. Besides their use as frequency standards and filters, one of the most well known and widely investigated application areas for microresonators is as mass-sensitive sensors. In this case, the microresonator is driven to oscillate at one of its mechanical resonance modes and a mass change is sensed by monitoring the resonance frequency of the resonator. Besides the high mass-sensitivity achieved with microresonators, their frequency output makes them attractive for chemical and biochemical sensing applications, promising a wide dynamic range, insensitivity to signal amplitude fluctuations, and a fast response time.

A resonating microstructure can be modeled as a simple harmonic oscillator consisting of a structural mass m, a damping coefficient b, and a spring constant k in the specific resonance mode of operation. From the Newton equation of motion, the well-known force-deflection relation of a harmonic oscillator in the Laplace domain is derived

$$\frac{X(s)}{F(s)} = \frac{1}{ms^2 + bs + k} \tag{3.1}$$

where $X(s)$ and $F(s)$ are the Laplace transforms of deflection and force, respectively.

Under the assumption of a weak damping, the resonance frequency ω_0 of the microstructure is determined as

$$\omega_0 = \sqrt{\frac{k}{m}} \tag{3.2}$$

Therefore, the resonance frequency change $\Delta\omega$ of the microstructure is related to a mass variation Δm and a stiffness variation Δk of the resonator:

$$\frac{\Delta\omega}{\omega_0} = -\frac{1}{2}\frac{\Delta m}{m} + \frac{1}{2}\frac{\Delta k}{k} \tag{3.3}$$

If the mechanical stiffness change of the resonator is negligible compared to the mass change, then the relative frequency change is essentially proportional to the relative mass change of the resonator.

3.1.1 Resolution of Mass-Sensitive Resonant Sensor

For the application of a microresonator as a chemical or biological sensor, the resonator surface has to be coated with a proper sensitive layer for the target molecules. The resolution c_{min} [µg/L] of the mass-sensitive chemical or biochemical sensor for a particular target analyte depends on the sensor sensitivity S [Hz/(µg/L)] and also on the minimal detectable frequency change Δf_{min} [Hz] of the resonator.

$$c_{min} = \Delta f_{min} / S \tag{3.4}$$

The sensor sensitivity is defined as the frequency change per change of analyte concentration in units of, e.g., [Hz/(µg/L)]. This sensitivity S is a function of the sorption characteristics of the chosen sensitive film, expressed by the partition coefficient [46], and the mass-sensing capability of the transducer:

$$S = \frac{df}{dc} = \frac{df}{d\rho_L} \cdot \frac{d\rho_L}{dc} = G \cdot S_A \tag{3.5}$$

Here, c, ρ_L, G, and S_A are the analyte concentration [µg/L], the density of the sensitive layer [kg/m^3], the mechanical density sensitivity of the resonator [Hz/(kg/m^3)], and the sensitivity related to the sorption characteristics of the sensitive coating [(kg/m^3)/(µg/L)], respectively. S_A is the density change of the sensitive film per change in analyte

concentration and, thus, solely determined by the sorption characteristics (partition coefficients) of the sensitive layer for the specific analyte. G, on the other hand, is solely a characteristic of the coated microresonator, relating the frequency change to the change in density of the sensitive film. To achieve a high sensor sensitivity, the density sensitivity G of the resonator must be improved, not just its mass sensitivity [Hz/kg]. It should be noted that the mass sensitivity can be easily improved by simply reducing the resonator's dimensions (see Equation (3.3)).

On the other hand, the minimal detectable frequency change of a resonator subject to harmonic oscillation is closely related to its short-term frequency stability. The frequency stability of a resonator in an amplifying feedback loop depends not only on the resonator itself but also on the phase noise of the feedback loop. The influence of the feedback loop phase noise $\partial \phi$ on the frequency output change $\partial \omega$ of a resonator is derived by first transforming Equation (3.1) into the frequency domain:

$$\frac{X(j\omega)}{F(j\omega)} = \frac{-j\dfrac{1}{m}}{\dfrac{\omega_0 \omega}{Q} - j\left(\omega_0^2 - \omega^2\right)} = \left|\frac{X(j\omega)}{F(j\omega)}\right| \cdot e^{j\phi} \text{ with } \omega_0 = \sqrt{\frac{k}{m}}, \quad Q = \frac{k}{b\omega_0} \tag{3.6}$$

The phase of the complex ratio $X(j\omega)/F(j\omega)$ is given by

$$\phi = -\frac{\pi}{2} + tan^{-1}\left(Q \cdot \frac{\omega_0^2 - \omega^2}{\omega \omega_0}\right) \tag{3.7}$$

and is approximated around the resonance frequency ω_0 by

$$\phi\big|_{\omega \cong \omega_0} = -\frac{\pi}{2} + tan^{-1}\left(2Q\frac{\omega_0 - \omega}{\omega_0}\right) \approx -\frac{\pi}{2} + 2Q \cdot \frac{\omega_0 - \omega}{\omega_0} \tag{3.8}$$

The resulting frequency noise per phase noise in proximity to ω_0 is given by

$$\frac{\partial \omega}{\partial \phi}\bigg|_{\omega \cong \omega_0} = -\frac{\omega_0}{2Q} \tag{3.9}$$

Designing a resonator with a high Q-factor reduces the frequency noise caused by the phase noise of the feedback loop. As a result, high Q-factor resonators show a better

frequency stability and a higher frequency resolution than resonators with low Q-factor. Therefore to achieve a better sensor resolution, the microresonators should be designed to have a high Q-factor and high density sensitivity. In this work, the approach of improving the frequency resolution by designing micro-resonators with high Q-factor is primarily investigated.

3.1.2 Quality Factor

The Q-factor of a resonator is defined as 2π times the ratio of the total stored mechanical energy E_S to the energy loss E_L in a single cycle of vibration.

$$Q = 2\pi \frac{E_S}{E_L} \tag{3.10}$$

The Q-factor is a complex parameter which depends on many energy dissipation mechanisms associated with the vibratory motion of a resonator. For a resonator operating at atmospheric pressure, vibration energy can be lost by viscous friction (viscous damping) of the surrounding fluid, coupling to the support structure (clamping loss), internal friction, etc. Among these, viscous damping is typically the most dominant loss mechanism when the resonator is operated in a gaseous/liquid environment, and is largely influenced by the geometry of the resonant structure and its resonance mode. Internal friction losses result from a variety of physical mechanisms, such as i) volume loss caused by lattice defects and phonon-phonon scattering, ii) surface loss originating from adsorbates on the surface and from surface defects due to the fabrication process, and iii) thermoelastic damping (TED) [9, 54, 55]. However, the exact mechanisms governing internal friction losses in microscale resonant structures are not well understood yet. The measured Q-factor of a resonator is the combination of the individual energy loss mechanisms, expressed as the inverse sum of the corresponding Q-factors:

$$\frac{1}{Q} = \frac{1}{Q_{viscous}} + \frac{1}{Q_{clamp}} + \frac{1}{Q_{volume}} + \frac{1}{Q_{surface}} + \frac{1}{Q_{TED}} + \dots \tag{3.11}$$

36

3.1.3 Resonant Micro Cantilever Sensor

Benefiting from extensive research on the fabrication and characterization of probes for atomic force microscopy (AFM), cantilever type resonant microstructures have been most extensively used as a resonant sensor platform for chemical and biochemical sensing applications. Q-factors up to 1,100 are typically achieved in air at resonance frequencies between 300 and 500 kHz, enabling sub-picogram mass resolution. Depending on the particular combination of analyte and sensitive layer, detection limits in the high ppb to low ppm range are reported with cantilever type resonant sensors [7, 8, 15].

However, in liquid environment, the cantilever's out-of-plane vibration is strongly damped, resulting in substantially lower Q-factors and, thus, mass resolution and detection limit [8, 56, 57]. In spite of extensive efforts, open-loop Q-factors above 20 are rarely achieved in liquid with micro cantilever type sensors [8, 58, 59].

In an attempt to overcome the high viscous damping and low sensor resolution in liquid, several different approaches have been investigated. Instead of measuring the resonance frequency changes in liquid, microcantilevers were immersed into the solutions containing the target analyte and afterwards dried. The analyte concentration is then sensed in air or vacuum by measuring the frequency change of the resonator before and after exposure to the liquid sample [3]. This method is, however, time consuming and not suitable for applications where continuous in-situ monitoring is required. Furthermore, the repeatability of the measurement results must be verified.

Another innovative approach is confining the liquid sample in a microfluidic channel integrated in a hollow cantilever beam, instead of operating the cantilever in the liquid. Analyte concentrations are sensed by measuring the resonance frequency shift of a suspended microfluidic channel upon accumulation of molecules on the inside walls of the device. Mass sensitivities up to 10^{-7} g/μm^2 have been reported with this method [6]. However, the fabrication process is rather complicated and the way of functionalizing or

coating the channel walls with a proper sensitive layer may limit its application as a biochemical sensor. Moreover, the on-chip excitation and detection elements have not been implemented yet with this MEMS resonator.

To overcome the above-mentioned limitations of cantilever-type resonant sensors in liquid environment, innovative designs for resonant microstructures and/or a proper choice of the resonance mode are highly required. In this work, microstructures vibrating in an in-plane mode are investigated to improve the Q-factor and, thus, the frequency resolution, by reducing the viscous damping caused by the vibratory motion of the resonator in a fluidic environment.

3.2 Resonator Design

Microresonators vibrating in an out-of-plane mode dissipate a substantial amount of energy by acoustic radiation into the surrounding media. At the same time, the resulting perpendicular fluid movements cause a mass-loading effect, increasing the effective mass of the resonator and, thus, reducing its resonance frequency. As a result, the sensor resolution is reduced dramatically, especially if operated in water.

A way to reduce acoustic damping and mitigate the mass-loading effect is using in-plane instead of out-of-plane vibration modes. In this work, a disk-shape microstructure operating in an in-plane mode is investigated. By shearing instead of compressing the surrounding fluid, damping from acoustic radiation and/or squeezed film damping is expected to reduce substantially, thus achieving higher Q-factors in air/liquid.

3.2.1 Eigenmodes of Disk Resonator

Figure 3.1 shows an SEM (Scanning Electron Microscope) image of the disk resonator investigated in this work. Two semi-circular disks are attached to a central silicon anchor beam by support beams.
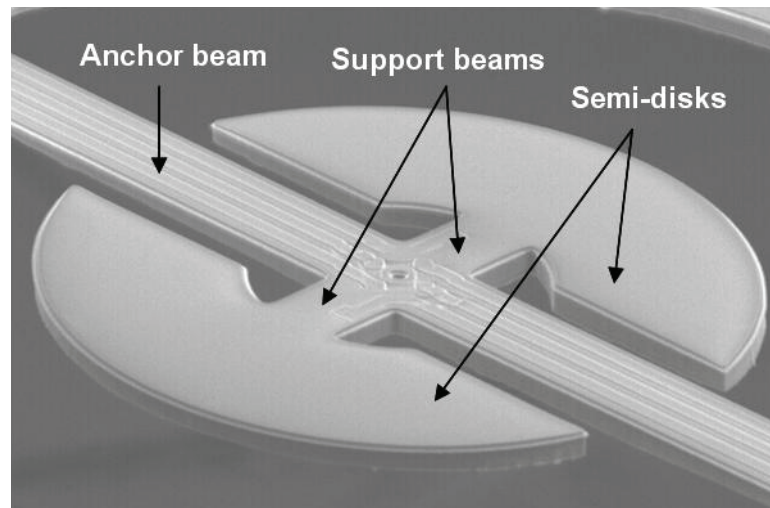
Figure 3.1: SEM photograph of a fabricated disk resonator.

This particular microstructure has several out-of-plane resonance modes at low frequencies (see simulated mode shapes in Figure 3.2), but operation at one of the higher frequency in-plane eigenmodes (6th, 7th and 11th modes in Figure 3.2) is preferred to minimize the damping from the surrounding fluid. It should be noted that depending on the structure dimensions, the order of the eigenmodes in Figure 3.2 might be changed.
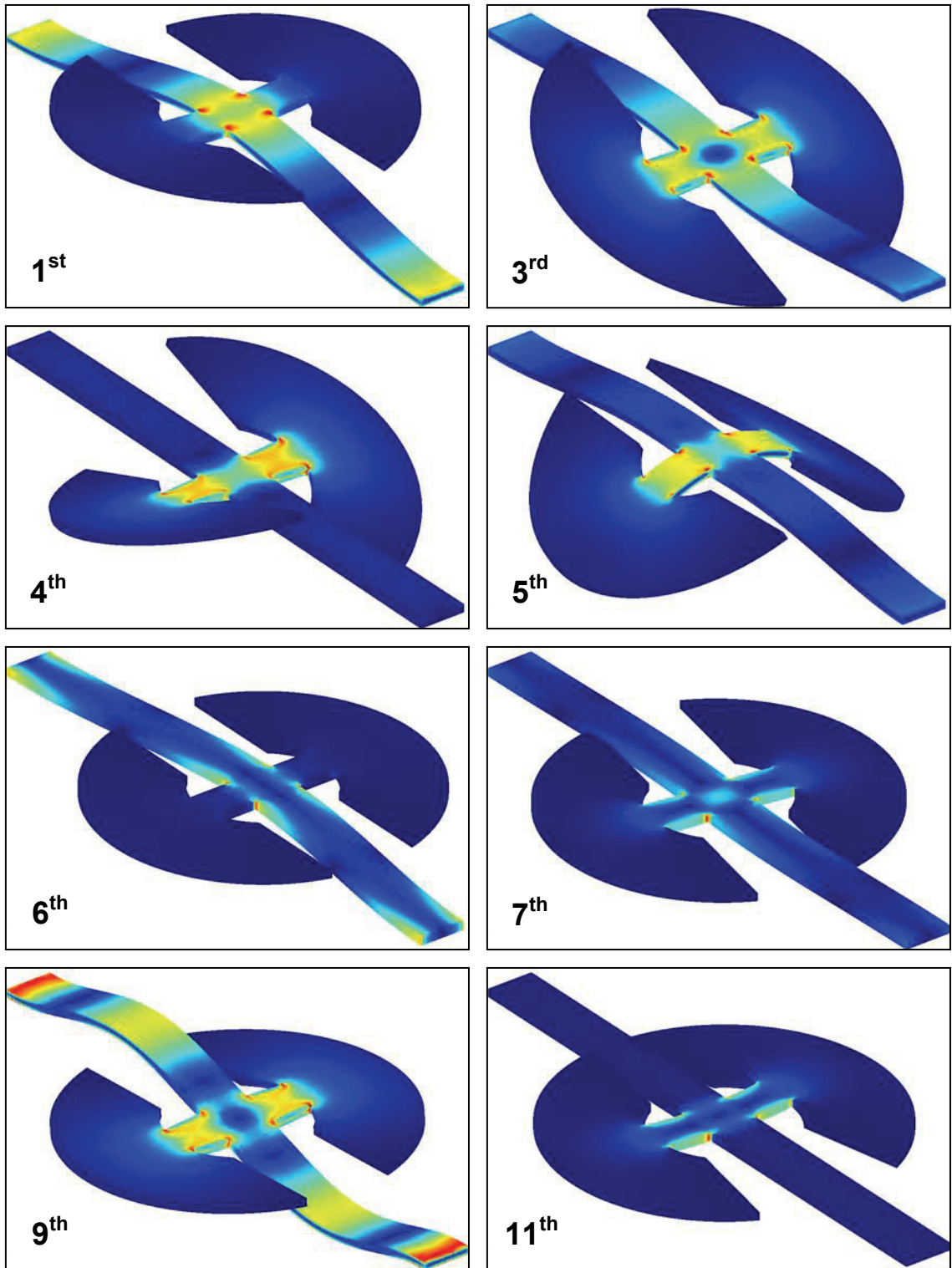
Figure 3.2: Resonance mode shapes of a disk resonator simulated with FEM software FEMLAB; the color coding indicates the stress distribution.

Among the three in-plane vibration mode shapes shown in Figure 3.2 (6th, 7th and 11th eigenmode), the two rotational vibration modes (7th and 11th modes) have been selected in this work. These two resonance mode shapes are illustrated in Figure 3.3; the mode shapes are characterized by having the half disks vibrate either in-phase (a) or out-of-phase (b).

| (a) | (b) |
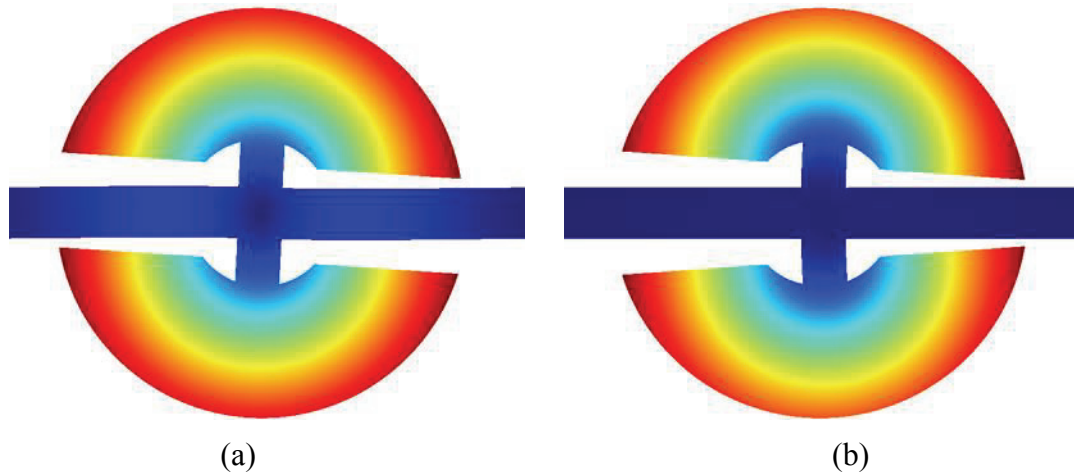
Figure 3.3: Two rotational in-plane mode shapes of a disk resonator simulated with FEMLAB; the two semi-disks vibrate either in-phase (a) or out-of-phase (b); the color code represents the total displacement.

At first glance, the out-of-phase resonance mode shown in Figure 3.3(b) looks attractive for achieving a high Q-factor, because the forces and moments acting on the two support beams cancel out each other at the center of the anchor beam. This is similar to the case of the anti-phase vibration mode of a tuning fork. However, in case of the out-of-phase vibratory mode, the center of gravity moves back and forth in the direction of the anchor beam, thus introducing additional anchor loss [60]. In addition, the possibility of turbulent flow generation is potentially higher if a disk resonator is operated in the out-of-phase resonance mode instead of the in-phase mode. Therefore, the current research is focusing primarily on the in-phase resonance mode shown in Figure 3.3(a).

3.2.2 Structure Dimensions

Microresonators intended for use as a sensor should have a clean resonance spectrum free of mode couplings, as non-linear frequency responses or frequency jumps may be produced by resonance mode couplings [22, 60]. To avoid this, the structure dimensions should ensure that the resonance mode of interest is far away from other resonance modes of the resonator. Moreover, considering structure aging, background noise floor and power consumption of digital circuitry [48, 49], high frequency resonance modes are not desirable for sensing applications. To avoid these challenges associated with high frequency resonance modes, the dimensions of the disk resonator were selected to have resonance frequencies less than 1 MHz.

Microstructures with different dimensions have been designed to investigate the influence of the resonator geometry on the Q-factor. The chosen design parameters are shown in Figure 3.4.
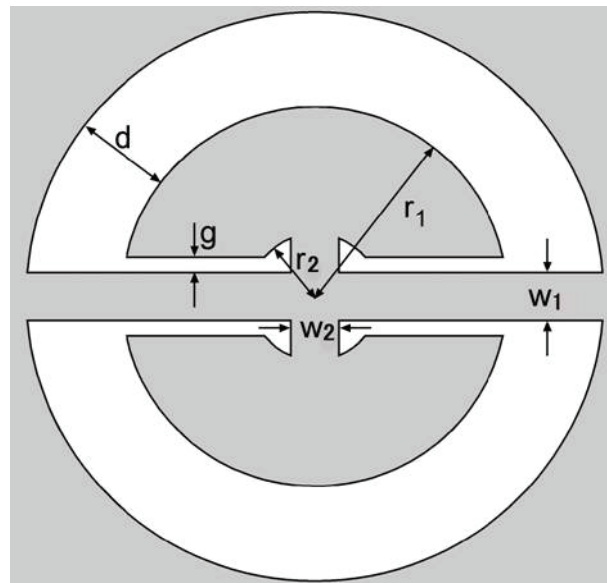
Figure 3.4: Schematic of disk resonator with the notations of key structure dimensions.

Here, r_1 is the radius of the disk, r_2 is the radius that determines the length of the disk support beams, w_1 is the width of the anchor beam, w_2 is the width of the support beam that connects the two semi-disks, g is the gap between semi-disk and anchor beam, t is the thickness of the structure, d is the length of the opening from semi-disk edge to substrate, and $l=2\times(r_1+d)$ is the length of the central anchor beam.

With a disk radius between 120 and 150 µm, sufficient surface area for the deposition of chemically or biologically sensitive films is provided and in-plane rotational resonance frequencies between 350 and 1,000 kHz are obtained from the FEM simulation results with FEMLAB. The designed resonator dimensions are summarized in Table 3.1 along with the range of simulated resonance frequencies.

Table 3.1: Dimensions of the designed resonators.

	r_1 : 120, 140, 150 µm
	r_2 : 40, 50 µm
	g : 5, 10, 15, 20 µm
Dimensions (see Figure3.4)	d : 50, 100 µm
	t (thickness): 8± 2µm
	w_1 : 35, 40, 45 µm
	w_2 : 30, 40 µm
Resonance frequency	350 ~ 1,000 kHz

3.2.3 Excitation and Detection Principles

Many different excitation and detection principles have been utilized for mechanical microresonators. Suitable integrated actuation and sensing elements must be able to excite the structure in the chosen resonance mode and, as far as possible, suppress

unwanted modes. Integrated excitation mechanisms commonly found in resonant microsensors include electrostatic, piezoelectric, electromagnetic, and electrothermal principles [61]. Electrostatic excitation is widely used in high-frequency resonators [62] and microfabricated vibratory gyroscopes [63]. The generation of sufficiently large electrostatic forces, however, requires either large driving voltages or relatively small air gaps. The undesired squeezed film damping in the sub-µm air gaps limits the applicability of electrostatic excitation in an air/liquid environment. Piezoelectric driving mechanisms are common in acoustic wave devices [64], but require either piezoelectric substrates or the deposition of piezoelectric thin films, such as PZT or ZnO, which are not standard materials found in industrial IC processes. Magnetic driving principles benefit from longer-range magnetic forces and are typically driven by currents [65-67]. Even though their power consumption is likely larger than that of electrostatic actuators, their low-voltage operation is more compatible with the operation voltages of microelectronic circuits. Most magnetic excitation principles rely on the Lorentz force and require an external magnetic field, which is generated by, e.g., a permanent magnet. Electrothermal excitation, on the other hand, has been extensively used in CMOS-based microresonators [7, 68]; it is effective and requires only heating resistors, which are readily available in any CMOS process. For these reasons, electrothermal excitation was mainly used as excitation principle for the designed disk resonators.

3.2.3.1 Electrothermal Excitation

To electrothermally excite mechanical oscillations in a microstructure, an AC excitation signal is superimposed on a DC voltage and applied to the heating resistor. This way, the generated heating power has a component with the same frequency as the applied electrical signal. The heating power P generated by the excitation voltage signal $V_{dc} + V_{ac} \cos \omega t$ is composed of a static component P_S and two dynamic components P_{d1} and P_{d2}:

$$P = P_S + P_{d1} + P_{d2}$$

$$P_S = \frac{V_{dc}^2}{R} + \frac{V_{ac}^2}{2R}, \quad P_{d1} = \frac{2V_{dc}V_{ac}}{R}\cos\omega t, \quad P_{d2} = \frac{V_{ac}^2}{2R}\cos 2\omega t \qquad (3.12)$$

The static heating power P_S contributes to the static temperature elevation of the microstructure and is dissipated mainly by heat conduction through the bulk material. The dynamic heating powers P_{d1} and P_{d2} produce a dynamic temperature variation in close proximity of the heating resistor with frequency ω and 2ω, respectively. The undesired dynamic power P_{d2} with frequency 2ω should be minimized by reducing the AC signal amplitude while increasing the DC offset voltage to maintain a sufficiently large dynamic power P_{d1}.

The temperature variation by the dynamic heating power is confined to a small volume in the vicinity of the heating resistor, because the penetration depth δ of the generated dynamic thermal wave decreases with frequency as [69]

$$\delta = \sqrt{\frac{2\kappa}{\rho c \omega}} \qquad (3.13)$$

where κ, ρ, c are the thermal conductivity, density and heat capacity of the material used, respectively. With the properties of a silicon ($\kappa = 156 W/(m \cdot K)$, $\rho = 2330 kg/m^3$, $c = 0.7 J/(g \cdot K)$), the penetration depth of the thermal wave is estimated to be 5~10 μm when considering operating frequencies in the range of 350 kHz~1 MHz for the designed disk resonators.

To excite the disk resonator in the rotational vibration mode, a thermal bimorph effect exploiting the difference in thermal expansion coefficients between aluminum and silicon is utilized. By placing the two diffused heating resistors asymmetrically along the two support beams as shown in Figure 3.5, the dynamic heating power produces an axial force via the thermal bimorph effect.
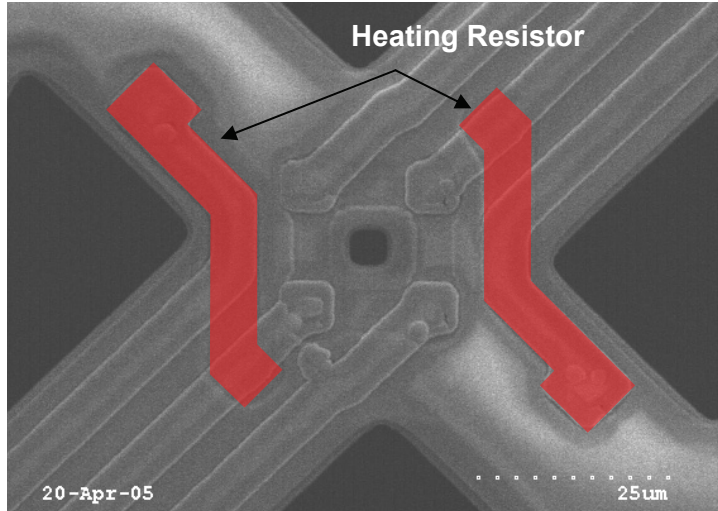
Figure 3.5: SEM image of disk resonator, showing the asymmetric arrangement of the heating resistors.

This force generates the rotational torque that excites the microresonator in the desired in-plane vibration mode as

$$\vec{T} = \vec{r} \times \vec{F} \qquad (3.14)$$

Here, $\vec{T}$, $\vec{F}$, $\vec{r}$ represent the generated torque, applied force, and the vector pointing from the center of rotation to the point of applied force (see Figure 3.6).
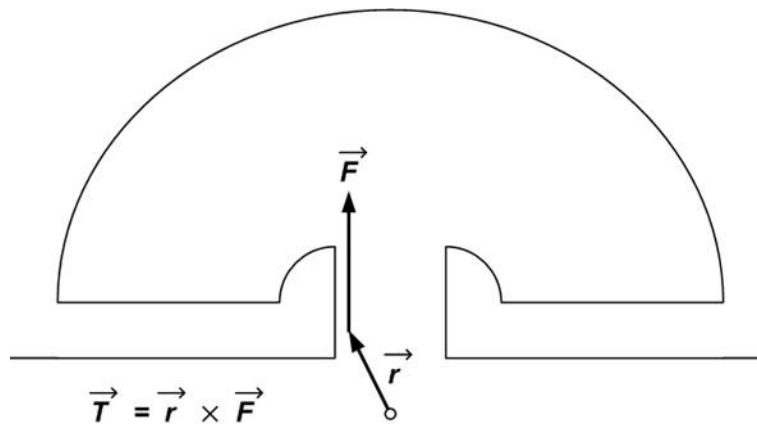
Figure 3.6: Schematic of torque generation by electrothermally induced force.

It should be noted that both an in-plane axial force and an out-of-plane bending moment are generated at the same time by the dynamic temperature variations. To suppress the out-of-plane vibration generated by the bending moment, the heating resistor should be placed as close as possible to the neutral plane (i.e., the center plane of the device in thickness direction) of the support beam. This is, however, difficult to achieve with the IC-compatible fabrication processes used in this work.

Besides the electrothermal excitation method discussed here, a magnetic excitation method has been developed for the disk-type resonators [70]. In this excitation scheme, the electromagnetic force between two current carrying conductors is exploited for driving the disk resonator at the rotational resonance mode.

3.2.3.2 Piezoresistive Detection

On the sensing side, piezoresistive detection of the microstructure vibration offers similar advantages as the electrothermal excitation method. It requires only silicon piezoresistors which are readily available in most silicon-based microfabrication processes. Because of the large piezoresistive effect in single crystalline silicon, the piezoresistive detection method is widely applied in silicon-based transducer design.

The resistance change of a thin film piezoresistor due to an externally applied stress is given by [23]

$$\frac{\Delta R}{R} = \pi_L \sigma_L + \pi_T \sigma_T \tag{3.15}$$

where π_L, π_T, σ_L, and σ_T are the longitudinal and transversal piezoresistive coefficients and the stress components parallel and perpendicular to the current flow, respectively. The piezoresistive coefficients π_L and π_T of single crystalline silicon depend on the resistor orientation, the dopant type, the doping concentration, and the temperature of the resistor. The maximum piezoresistive coefficients of low doped n- and p-type

47

monocrystalline silicon in the (001) plane at room temperature are summarized in Table 3.2.

Table 3.2: Maximum piezoresistive coefficients of
low doped monocrystalline silicon in (001) plane [23].

	n-type	p-type
Direction	<100>	<110>
π_L (10^{-11} Pa^{-1})	-102.2	71.8
π_T (10^{-11} Pa^{-1})	53.4	-66.3

To maximize the sensitivity of the piezoresistive detection, the piezoresistors should be placed at the location where maximum stress is generated by the vibratory motion of the resonator. To compensate for a resistance change originating from a temperature change, the piezoresistors are typically arranged in a Wheatstone bridge configuration. Thereby, a resistance change with opposite sign for the two diagonal resistor pairs of the Wheatstone bridge is desirable to get a stronger output signal.

In order to design the piezoresistive Wheatstone bridge for the disk resonator, FEM simulations were carried out with FEMLAB to estimate the stress distribution in a disk resonator generated by the in-phase rotational motion in Figure 3.3 (a). Figure 3.7 (a), (b) shows a contour plot of the simulated Von Mises stress, when the resonator rotates counter-clock-wise.
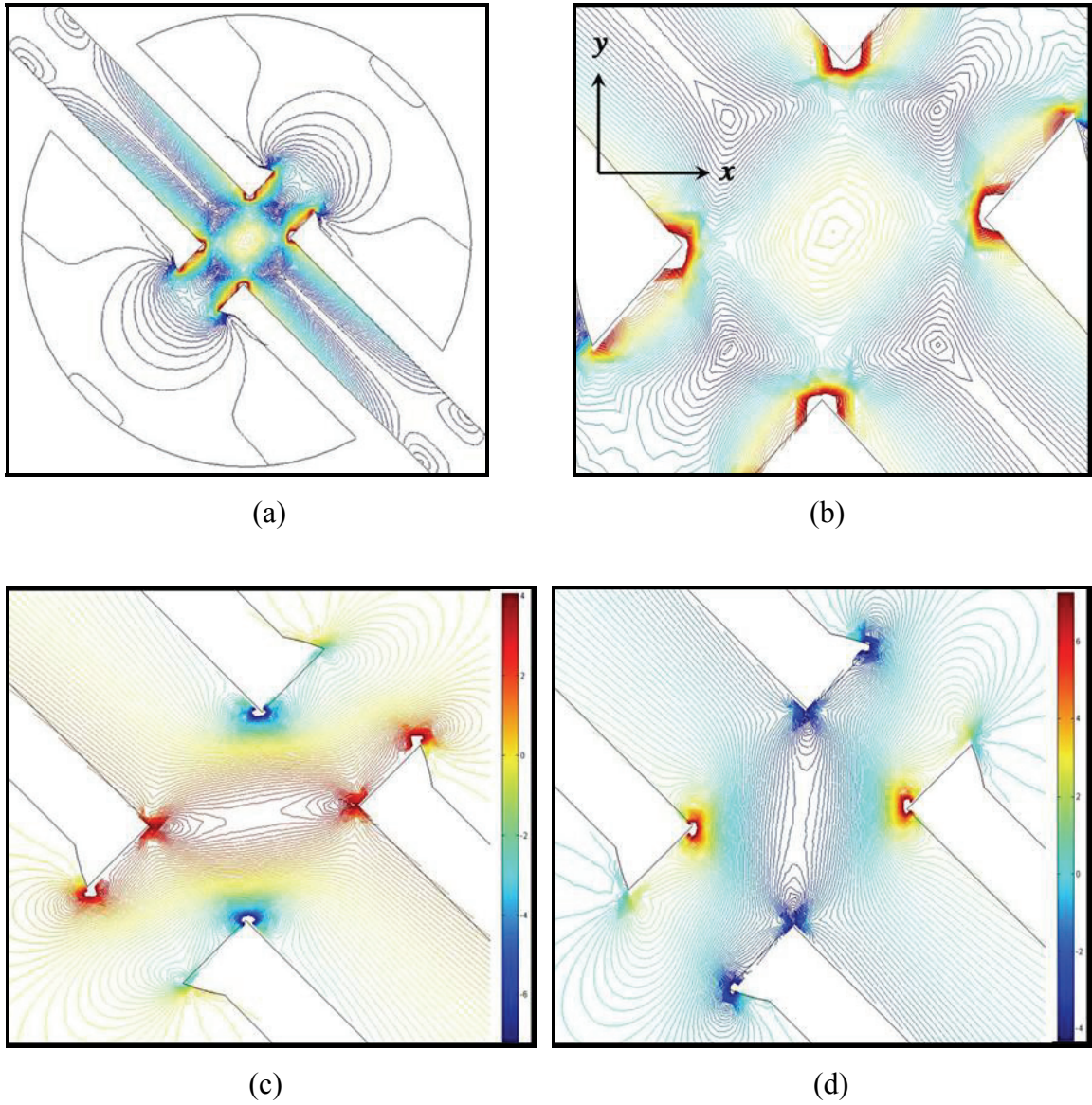
Figure 3.7: Stress distribution during counter-clock-wise rotation of a disk resonator; contour plots of Von Mises stress along the anchor and support beam (a) and around the center of rotation (b); stress component in x-direction (c) and y-direction (d) in the center of the anchor beam.

As expected, the maximum stress appears along the edge of the two support beams. However, since the heating resistors are already located on one side of the support beam, a symmetric arrangement of the Wheatstone bridge is difficult to achieve. Furthermore, if the piezoresistors are placed along the edge of the support beams, the sensor output signal would be sensitive not only to the in-plane modes but also to several out-of-plane vibration modes of the resonator. Another possible location for the sensing elements is the area around the center of rotation. Even though the maximum stress around this area is smaller than in the previous case, the stress distributions in the x- and y-direction are better suited for a piezoresistive Wheatstone bridge configuration, as shown in Figure 3.7(c) and (d). When a piezoresistor is placed along the x-axis, it will experience tensile longitudinal stress and compressive transversal stress while the disk resonator rotates in counter-clock-wise direction, resulting in a positive resistance change if p-type piezoresistors are used. On the other hand, if a piezoresistor is aligned along the y-axis, a negative resistance change will result by the compressive longitudinal stress and the tensile transversal stresses. Thus, the signals will add up if the Wheatstone bridge in the center of the anchor beam is formed with one diagonal resistor pair parallel to the x-axis and one resistor pair parallel to the y-axis.

An SEM image of the designed piezoresistive Wheatstone bridge in the center of the disk resonator is shown in Figure 3.8. This arrangement is only sensitive to the in-phase rotational eigenmodes of interest, while out-of-plane modes are effectively suppressed at the output of the piezoresistive Wheatstone bridge.
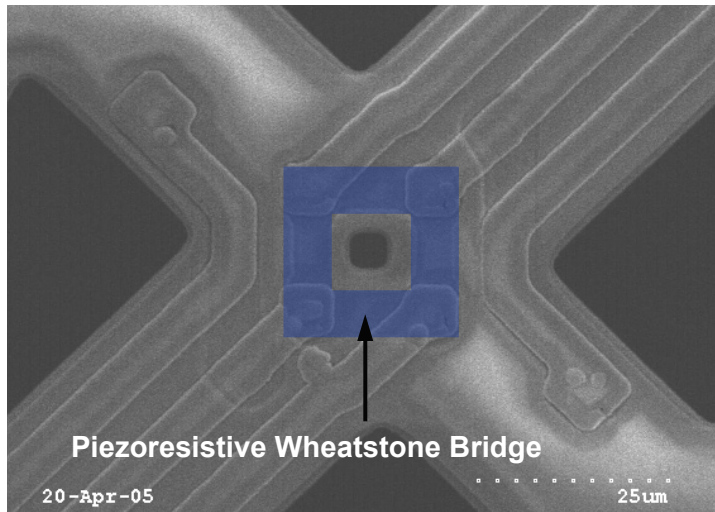
Figure 3.8: SEM image of disk resonator, showing the designed piezoresistive Wheatstone bridge in the center of the anchor beam along with the asymmetric heating resistors in the support beams.

Figure 3.9(a) shows a schematic diagram illustrating the electrical connections to the Wheatstone bridge and the heating resistors. The electrical signals applied to the terminals V_{EX1} and V_{EX2} to excite the in-phase rotational resonance mode are shown in Figure 3.9(b). The output signal of the piezoresistive Wheatstone bridge is sensed differentially from the voltages at terminals V_{S+} and V_{S-}.

(a)

(b)
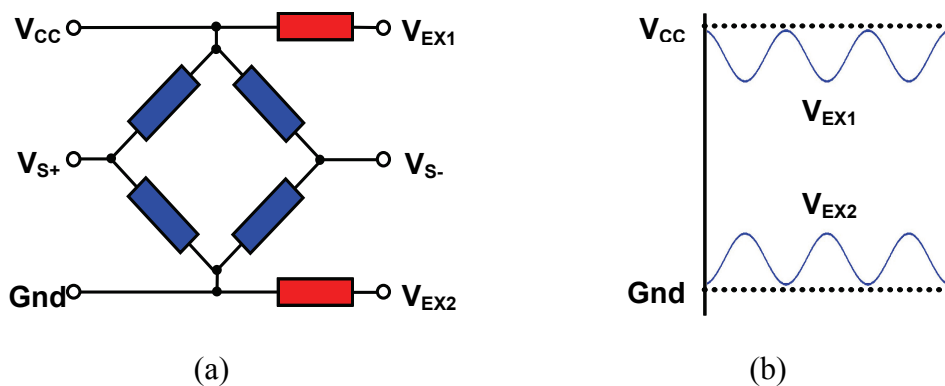
Figure 3.9: (a) Electrical connection scheme of piezoresistive Wheatstone bridge and heating resistors and (b) excitation signals applied to terminals V_{EX1} and V_{EX2}.

3.3 Fabrication Process

The fabrication process is designed to enable later integration of the proposed resonators in a CMOS process [9]. (100) silicon epi-wafers with a 6 μm phosphorous-doped epitaxial layer on top of a p-substrate have been used as starting material. The epi-layer thickness defines the final resonator thickness after anisotropic silicon etching with an electrochemical etch-stop technique. In a CMOS process, the standard n-well can be used as a structural layer instead.

First, a 1 μm silicon dioxide layer is grown thermally in a wet oxidation furnace at 1050 °C. After patterning a silicon dioxide diffusion mask, p-type piezoresistors and heating resistors are diffused as shown in Figure 3.10 (a). To get the highest piezoresistive coefficient, the p-type piezoresistors are aligned with the <110> directions of the wafer. Pre-deposition diffusion was done from boron solid sources at 930 °C for 1 hr, giving a sheet resistance of 150 ohm/square. Drive-in diffusion and thermal oxidation on top of the boron diffused areas were performed at the same time in a thermal oxidation furnace, resulting in a 0.1 μm oxide growth. In a CMOS process, the source/drain implantation of p-channel MOSFETs would be used for doping the heating resistor and piezoresistor area. After etching contact openings with an ICP (Inductively Coupled Plasma) etcher, a 0.8 μm aluminum layer is sputter deposited and patterned by wet etching, followed by sintering in forming gas at 425°C for 40 minutes (Figure 3.10 (b)).

A silicon oxide/nitride layer sandwich with up to 8 layers is deposited by PECVD (Plasma Enhanced Chemical Vapor Deposition) on the top of the wafer as an insulation layer. The final PECVD silicon dioxide layer is used as an etch mask enduring the final structure release. Alternating silicon oxide/nitride layers were found necessary to reduce the possibility of metal corrosion through pinholes in the deposited PECVD films in highly ionic solutions.

(a)

(b)

(c)

(d)

P-substrate   N-epi layer   Boron diffused area

SiO₂   Aluminum   PECVD oxide

PECVD nitride

Figure 3.10: Fabrication process flow for the disk-type silicon resonators.

The number of required silicon oxide/nitride layers and the thickness of each layer have been determined by the desired operating conditions, i.e. in operation air or in water, and by the number of pinholes in the deposited PECVD films. It should be noted that the required passivation thickness strongly depends on the film quality of the used deposition equipment. The deposited PECVD insulation layers are patterned with RIE (Reactive Ion Etching) to define the areas to be etched during the final structure release (Figure 3.10 (c)).

Next, a 700 nm PECVD silicon nitride film is deposited and patterned on the back of the wafer to act as a KOH etch mask. For precise control of the fabricated device thickness, an electrochemical etch-stop technique with a three electrode setup is used during anisotropic silicon etching with a 6 molar KOH solution at 75 °C. A potentiostat (AMMT, Frankenthal, Germany) supplies the necessary potential (1.8V) to reverse bias the pn junction between the epi-layer and the substrate in the KOH solution and monitors the current. As the etching step progresses, the current through the pn junction reaches a peak value and drops down to a steady state value (see Figure 3.11), indicating the termination of the etching by the formation of the anodic oxide. A more detailed description of the electrochemical etch-stop technique can be found in [71].
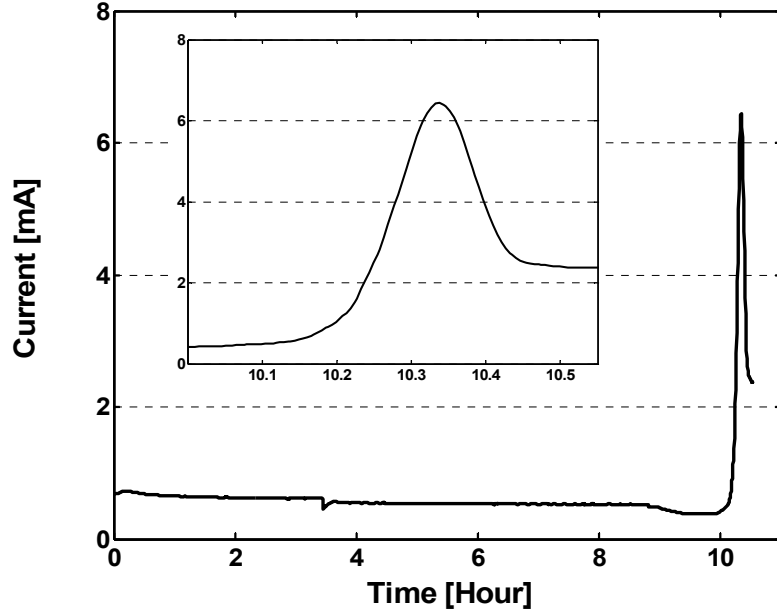
Figure 3.11: Typical current profile during the anisotropic etching in a 6-molar KOH solution using a three-electrode electrochemical etch stop technique at 75°C with 1.8V bias voltage; the inset displays the current at the end of electrochemical etching indicating surface passivation due to the formation of an anodic oxide.

Finally, the microstructures are released by RIE (Reactive Ion Etcher) etching from the top of the wafer (Figure 3.10 (d)). An SEM image of fabricated disk resonators is shown in Figure 3.12. A similar bulk-micromachining sequence has been successfully used for releasing a variety of integrated microsystems as a post-CMOS fabrication sequence [72]. The fabricated resonators exhibited substantial thickness variations (between 6 and 10 μm) from resonator to resonator depending on their location on the wafer. It is believed that a non-uniform etching potential distribution on the wafer caused variations in the depletion region width of the reverse biased pn junction between n-type epi-layer and low-doped p-type substrate (10~20 Ω·cm) and, thus, the thickness variations of the resulting samples. At the same time, the hydrogen bubbles generated on the surface of exposed silicon areas during the KOH etching may block the silicon etching, and contribute to the observed thickness variations. Low temperature etching in

high-concentration KOH solutions and/or sufficient over-etching after the current peak are expected to reduce the thickness variations by the anisotropic KOH etching.
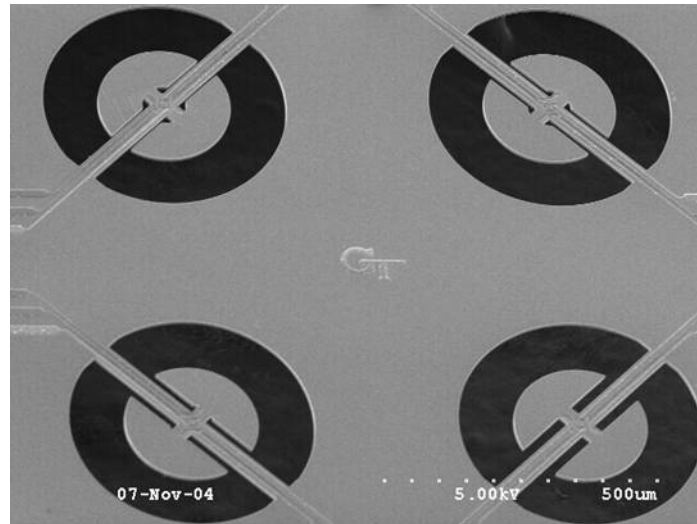
Figure 3.12: SEM image of fabricated disk resonators with different air gaps between 5 and 20µm.

CHAPTER 4

CHARACTERIZATION OF MICRORESONATORS

The present chapter summarizes the fundamental characterization of the fabricated disk-type resonators. The feasibility and efficiency of the designed on-chip electrothermal excitation and piezoresistive detection schemes are assessed. The key parameters of the resonant microstructures determining their performance as mass-sensitive sensing elements are investigated; these include the resonance frequency and its temperature coefficient, the Q-factor in air, liquid and vacuum, as well as the short-term frequency stability of the resonance frequency. The influence of an electrical coupling between the excitation and detection signal on the open-loop characteristics of the resonators and the possibility of subtracting the resulting cross-talk component from the measured data are discussed as well in this chapter.

4.1. Open-Loop Characteristics

The fabricated disk resonators with various dimensions are mounted and wire-bonded to ceramic Dual-In-Line (DIL) packages. For open-loop characterization, a custom-made printed circuit board (PCB, see Figure 4.1) adds a DC offset voltage to the AC excitation signal generated by an Agilent 4395A network/spectrum analyzer and the resulting excitation signals are supplied to the heating resistors of the disk resonator as discussed in Chapter 3.2.3. The integrated piezoresistive Wheatstone bridge is biased at $3V_{DC}$ and the detection signal is read out differentially using a commercially available THS-4012 high bandwidth buffer amplifier. To reduce cross-coupling between the

excitation and detection signal within the PCB itself, excitation and detection signals are processed separately using two identical PCB. The buffered Wheatstone bridge output signal is fed to the network/spectrum analyzer and the open-loop transfer characteristic of the disk resonator is recorded.
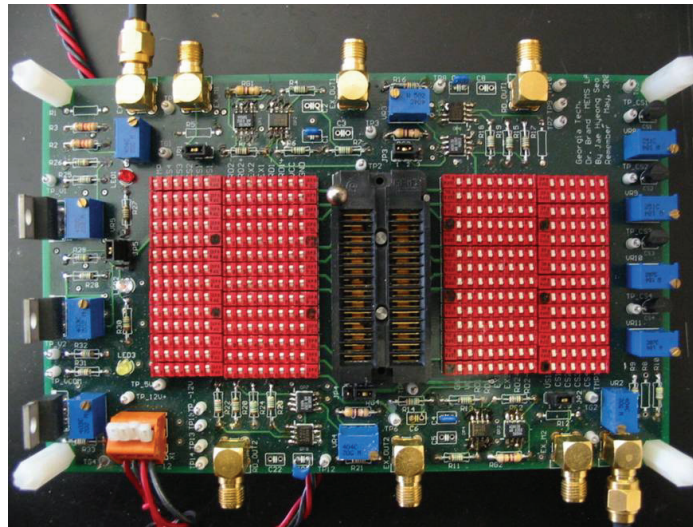
Figure 4.1: Printed circuit board used for the measurement of the open-loop characteristics of the disk resonators.

4.1.1 Frequency Spectrum

A typical amplitude transfer characteristic of a disk resonator, measured using the piezoresistive Wheatstone bridge output signal, is shown in Figure 4.2. In this particular example, the frequency of the excitation signal is swept from 100 kHz to 1 MHz.
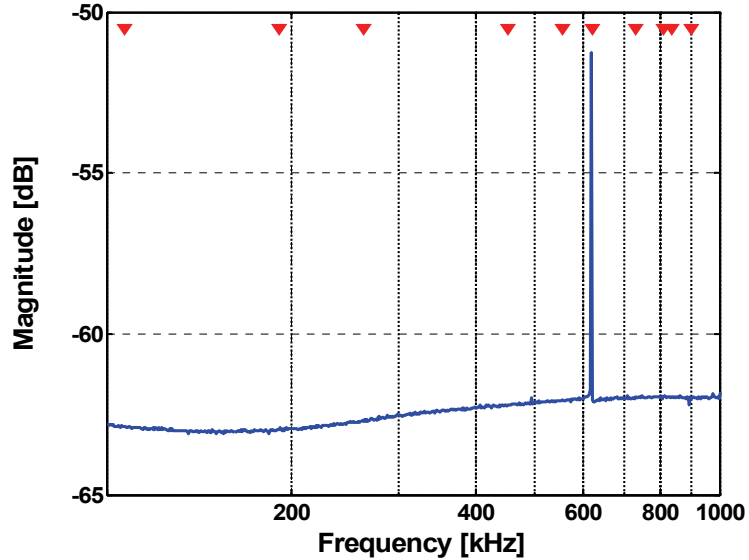
Figure 4.2: Amplitude transfer characteristic of disk resonator with $r_1 = 120$ µm, $r_2 = 50$ µm, $g = 15$ µm and $d = 100$ µm from 100 kHz to 1 MHz, measured using the integrated piezoresistive Wheatstone bridge.

Only one resonance mode around 600 kHz is visible in the frequency spectrum of Figure 4.2. The triangles in Figure 4.2 indicate the eigenfrequencies of a disk resonator with $r_1 = 120$ µm, $r_2 = 50$ µm, $g = 15$ µm and $d = 100$ µm, as obtained from FEM simulations using FEMLAB. The observed resonance peak corresponds to the simulated resonance frequency of the in-phase rotational resonance mode of interest. Further experiments have been carried out to confirm that the observed resonance peak is indeed originating from the in-phase rotational vibration mode. The disk resonator was excited at the out-of-phase resonance mode shown in Figure 3.3 (b) by modifying one of the excitation signals: the polarity of the DC-offset voltage applied to one of the excitation signals is changed (see Figure 4.3). Thus, the dynamic heating powers generated in the heating resistors by the two excitation signals have a 180° phase difference to each other and excite the resonator at the out-of-phase resonance mode. To be able to detect this resonance mode, the voltage signals from each half bridge of the Wheatstone bridge are added up using external operational amplifiers as shown in Figure 4.3. Therefore, the disk

59

resonator can be excited at both of the rotational eigenmodes and each of the corresponding vibration modes can be detected and compared with corresponding FEM data.
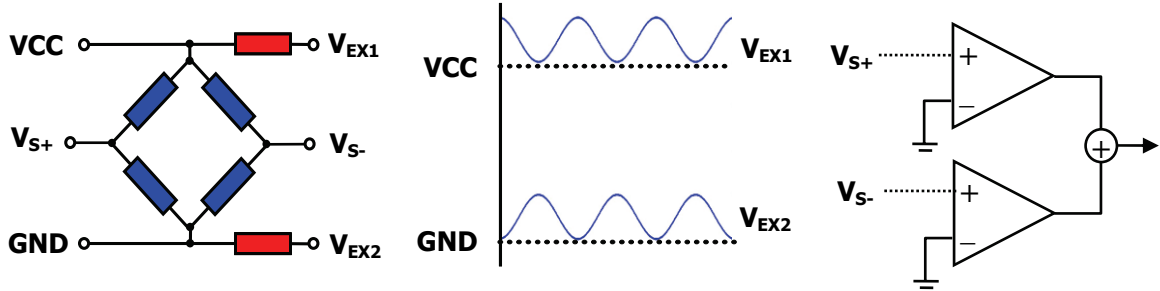
Figure 4.3: Excitation and detection scheme for out-of-phase resonance mode of the disk resonator; shown from the left are a schematic of the electrical connection of piezoresistors and heating resistors, the applied excitation signals and the external circuit for detection.

Figure 4.4 shows the frequency response of a disk resonator with $r_1 = 140$ μm, $r_2 = 40$ μm, $g = 15$ μm and $d = 100$ μm. Based on the FEM simulation result, the in-phase and out-of-phase resonance modes are expected to have resonance frequencies of 415 kHz and 604 kHz, respectively. When it is excited at the in-phase vibration mode, the resonance peak at 412 kHz is clearly visible in the frequency spectrum of the resonator (see Figs. 4.4 (a) and (b)), which agrees well with the simulation result.
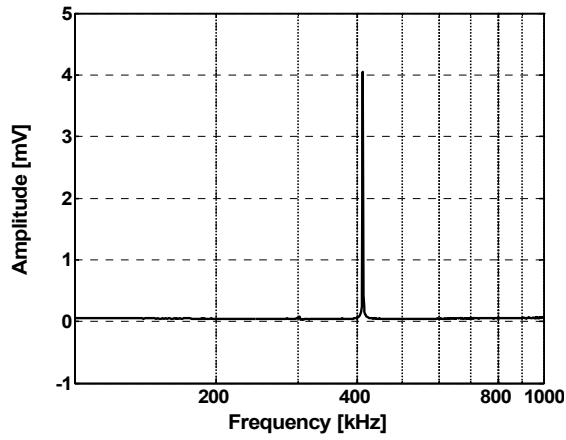
(a)
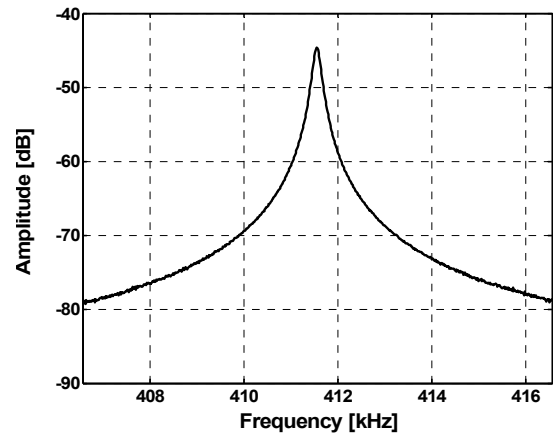
(b)
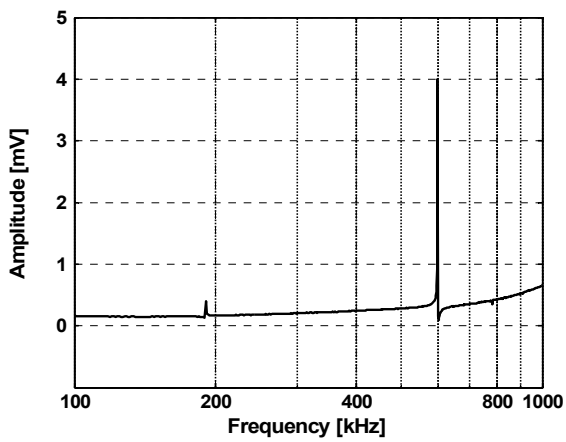
(c)
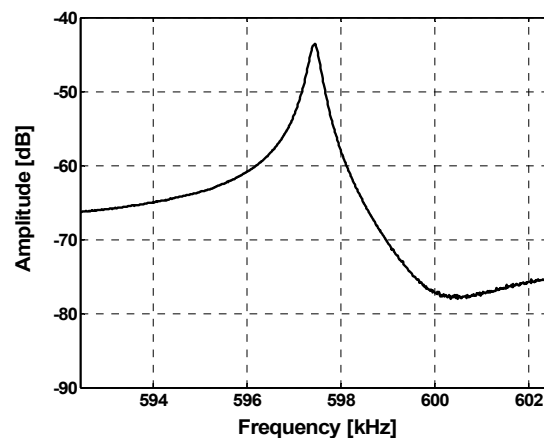
(d)

Figure 4.4: Amplitude transfer characteristics of in-phase ((a) and (b)) and out-of-phase ((c) and (d)) resonance modes of a disk resonator with $r_1 = 140$ µm, $r_2 = 40$ µm, $g = 15$ µm and $d = 100$ µm.

On the other hand, when the disk resonator is excited at the out-of-phase resonance mode, the resonance peak at 412 kHz disappears and a resonance peak at 597 kHz becomes dominant in the frequency spectrum as shown in Figs. 4.4 (c), (d). The measured in-phase and out-of-phase resonance frequencies of a disk resonator match well with those from FEM simulation results and the resonator responds to each of the excitation signals as expected. This experiment confirms at least partially that the high amplitude resonance peak, e.g. in Figure 4.2, corresponds to the in-plane rotational vibration mode. The higher noise floor of the out-of-phase resonance mode is caused by the common mode noise amplification of the modified detection circuitry in Figure 4.3.

The experimental results confirm that almost all low frequency, out-of-plane resonant modes are efficiently suppressed by the chosen actuation and detection scheme. The successful suppression of unwanted resonance modes greatly simplifies the operation of the resonators in an amplifying feedback loop. Moreover, the clean frequency spectrum around the rotational in-phase resonance frequency improves the frequency stability of the resonators.

4.1.2 Quality Factor in Air

The Q-factors of the rotational in-phase resonance mode of the fabricated resonators are extracted from the 3dB-bandwidth of the resonance. Figure 4.5 shows amplitude and phase of the Wheatstone bridge output signal around the resonance frequency in air, obtained from resonators with different dimensions.
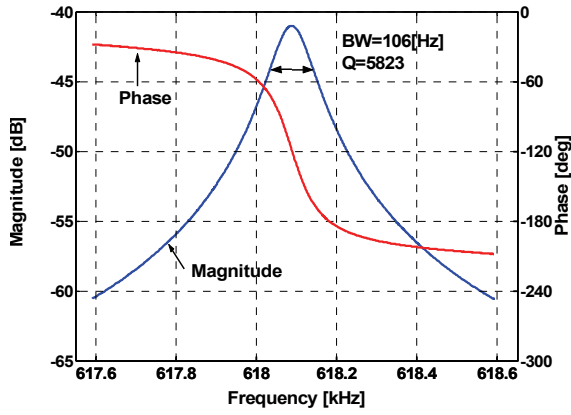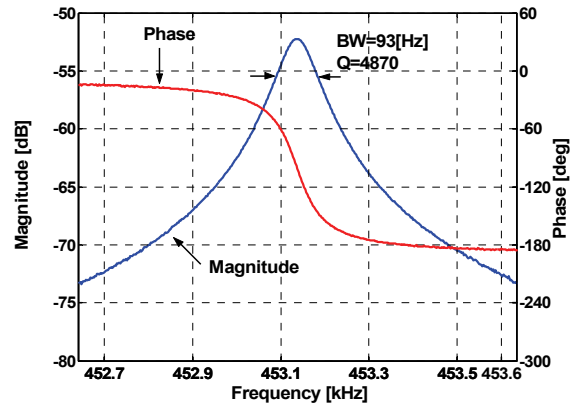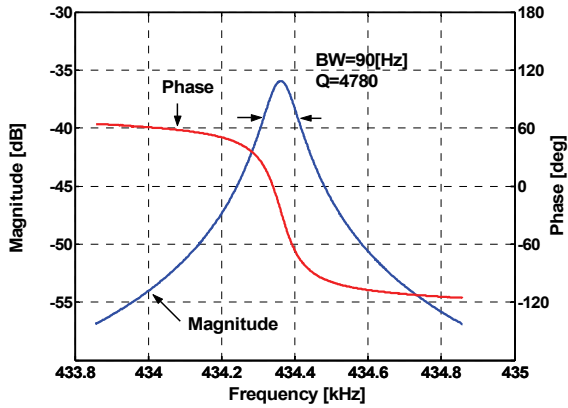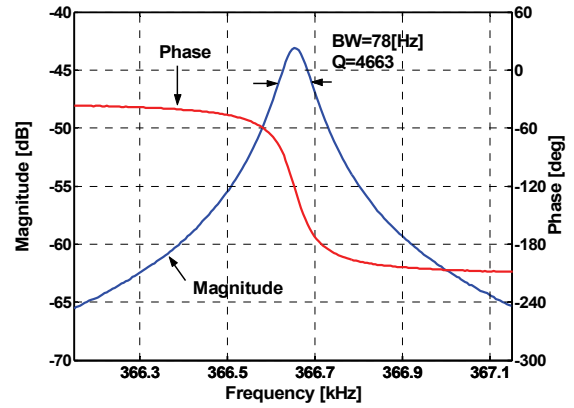
Figure 4.5: Magnitude and phase of the piezoresistive Wheatstone bridge output signal around the in-plane resonance frequency of disk resonators with different dimensions: (a) $r_1 = 120$ μm, $r_2 = 50$ μm, $d = 100$ μm, (b) $r_1 = 140$ μm, $r_2 = 50$ μm, $d = 50$ μm, (c) $r_1 = 140$ μm, $r_2 = 40$ μm, $d = 100$ μm, (d) $r_1 = 150$ μm, $r_2 = 40$ μm, $d = 100$ μm.

The open-loop characteristics of the resonators showing the highest Q-factors for specific structure dimensions are shown in Figure 4.5. The resonator with dimensions $r_1 = 120\ \mu m$, $r_2 = 50\ \mu m$, $g = 15\ \mu m$ and $d = 100\ \mu m$ shows the highest Q-factor of 5823 in air amongst the devices tested in this work.

To assess the influence of the air gap g on the Q-factor, the amplitude transfer characteristics of disk resonators with air gaps ranging from 5 to $20\mu m$ are shown in Figure 4.6, while keeping all other dimensions the same ($r_1 = 120\ \mu m$, $r_2 = 50\ \mu m$, $d=100\ \mu m$). It should be noted that all four resonators are located on the same silicon chip, i.e. they all have a comparable device thickness.
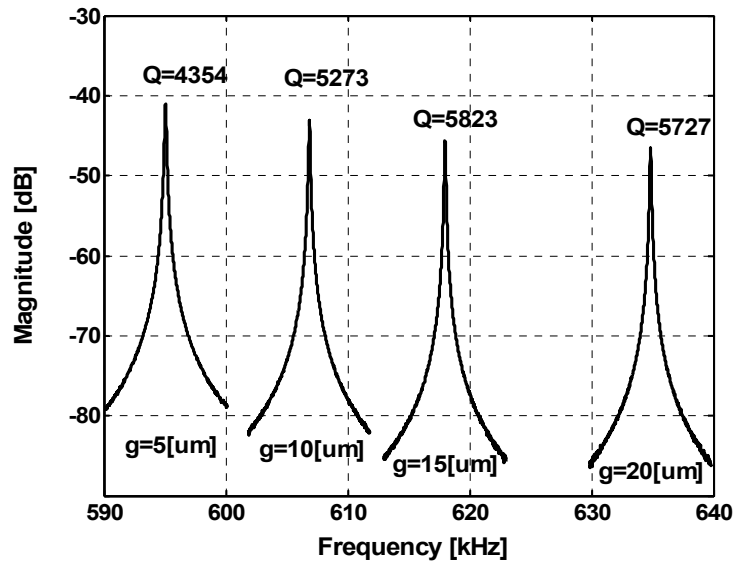
Figure 4.6: Frequency response of disk resonators ($r_1 = 120\ \mu m$, $r_2 = 50\ \mu m$, $d = 100\ \mu m$) with increasing air gap $g = 5$-$20\ \mu m$.

The resonance frequency increases with increasing air gap (g) because of the resulting mass decrease of the semi-disks. The squeezed film damping seems to contribute a substantial energy loss compared to the shear film damping at small air gap

even though the device thickness is relatively small, thus lowering the Q-factor as the air gap (g) decreases. A cross-talk component has been subtracted from the Wheatstone bridge output signal in this plot to display the resonance behavior more clearly. This cross-talk component affects the measured amplitude transfer characteristic but can be subtracted mathematically as will be explained later in Section 4.3.

The measured Q-factors in air are summarized in Figure 4.7 as a function of the resonance frequencies of the fabricated disk resonators. Depending on the material and thickness of the used passivation layers but also on the fabrication batch, substantial variations in measured Q-factors are observed.
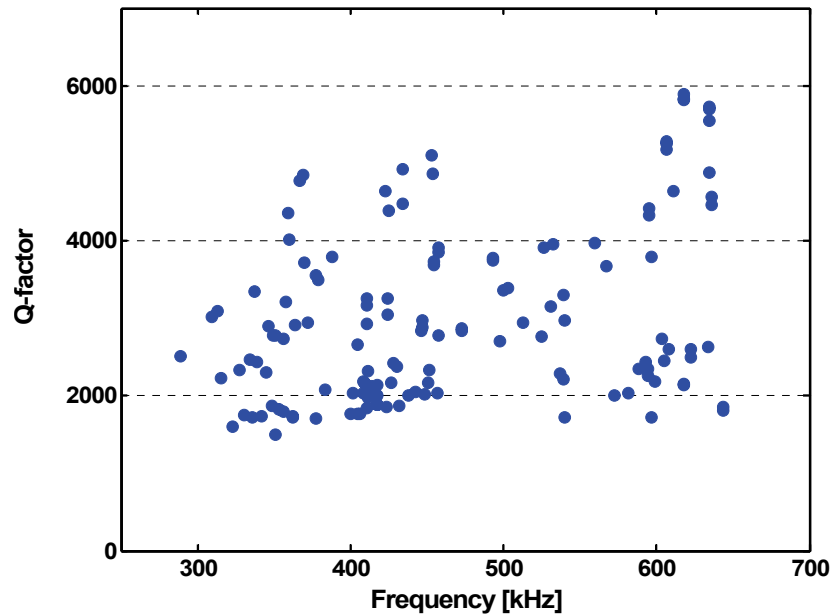
Figure 4.7: Plot of measured Q-factor as a function of resonance frequency for all disk resonators tested in this work.

We mainly attribute these variations to device thickness variations and different passivation layer compositions and thicknesses; generally higher Q-factors were measured for thicker resonators covered with a thinner passivation layer sandwich. It

65

should be noted that the data points shown in Figure 4.7 includes disk resonators with 0.1 μm total passivation thickness but also many devices with over 3 μm passivation layer, optimized for stable operation in liquid environment. By improving the uniformity of each fabrication step and by keeping the thickness and composition of the used passivation layers the same, the Q-factor variation of the disk resonators is expected to be minimized.

4.1.3 Quality Factor in Water

For the Q-factor measurements in liquid environment, the aluminum pads of the resonators and the bonding wires connecting the resonator with the DIL package are protected with UV curable epoxy (OZ116 from Epoxy Technologies) as illustrated in Figure 4.8. DI (de-ionized) water is dropped onto the resonator with a pipette and the frequency response is measured.

(a)   (b)
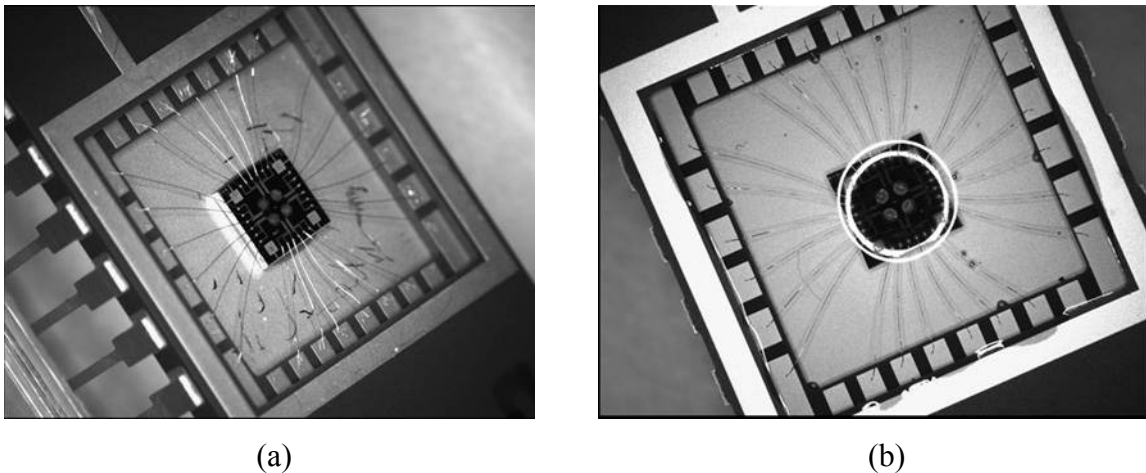
Figure 4.8: Sample preparation for the Q-factor measurements in water; (a) resonator chip mounted in a DIL package after wire-bonding, (b) DIL package after encapsulation of wire bonds and pads with UV curable epoxy.

When resonators with only two layers of PECVD silicon oxide/nitride passivation layers are immersed in water, instantaneous corrosion of the aluminum lines is observed due to pin-holes in the deposited PECVD films. To avoid this problem, a 1 μm protective parylene film is used as an additional insulation layer for stable operation in water. Parylene is known to form a pin-hole free, conformal coating by a vapor deposition process [73]. The Q-factor in air is lowered by a factor of almost five compared to the case before parylene coating, as shown in Figure 4.9. This means that the internal frictional energy loss caused by the additional polymer coating becomes almost 5 times larger than the energy loss by the viscous damping of the resonator. Despite the substantial decrease of the Q-factor in air caused by the polymer coating, the parylene-coated resonator showed a Q-factor of 94 in water. The small vibration amplitude of the resonator in water, paired with the high dielectric constant of water reduces the signal-to-noise ratio of the Wheatstone bridge output signal dramatically compared to the case in air. In Figure 4.9, a capacitive cross-talk signal has been mathematically removed from the measurement result in water to show the resonance behavior more clearly.
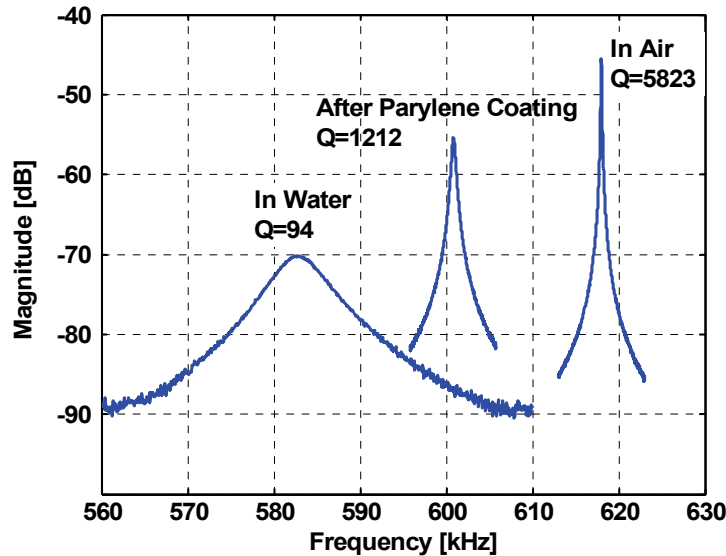
Figure 4.9: Wheatstone bridge output signal around in-plane resonance frequency of disk resonator (i) in air, (ii) in air after parylene coating, and (iii) in water.

The 1 μm thickness of the parylene coating was found to be sufficient to protect the aluminum metallization for short-term measurements in water. Thicker parylene coatings should be used for long-term measurements in water. In an attempt to minimize the decrease in the Q-factor by the polymer coating, multiple layers of PECVD silicon oxide and nitride films have been used as passivation layers instead. To prevent the erosion of the aluminum metallization through pin-holes in the PECVD films, 7 layers of oxide and nitride passivation are deposited on both sides (top and bottom surface) of the resonators (total passivation layer thickness of 3 μm), ensuring stable operation of the microresonators in water environment. It should be noted that the optimal thickness and composition of the passivation layer strongly depends on the individual film quality and, thus, on the PECVD process recipe and the deposition equipment. Resonators with thick PECVD passivation layers generally showed higher Q-factors in air than the parylene-coated resonators, but a substantial improvement in the Q-factor in water was not observed. Proper passivation methods with reduced layer thickness and minimum defects are expected to improve the performance of a disk resonator further in liquid environment.

The measured Q-factors of disk resonators in water are summarized and plotted in Figure 4.10 (a) as a function of the resonance frequency. Generally, the Q-factor increases gradually as the resonance frequency increases. However, the measured Q-factors show large variations from sample to sample. Combined with measurement errors caused by the small signal amplitude in water, variations of the hydrophobicity of the resonator surface layer may cause these variations. This will be discussed more in more detail in Chapter. 5. Figure 4.10 (b) shows the ratio of the resonance frequency in water and in air as a function of the resonance frequency in air. The resonance frequency is only slightly (generally less than 3%) lowered in water, because of the relatively small added-mass effect of the in-plane vibration mode.
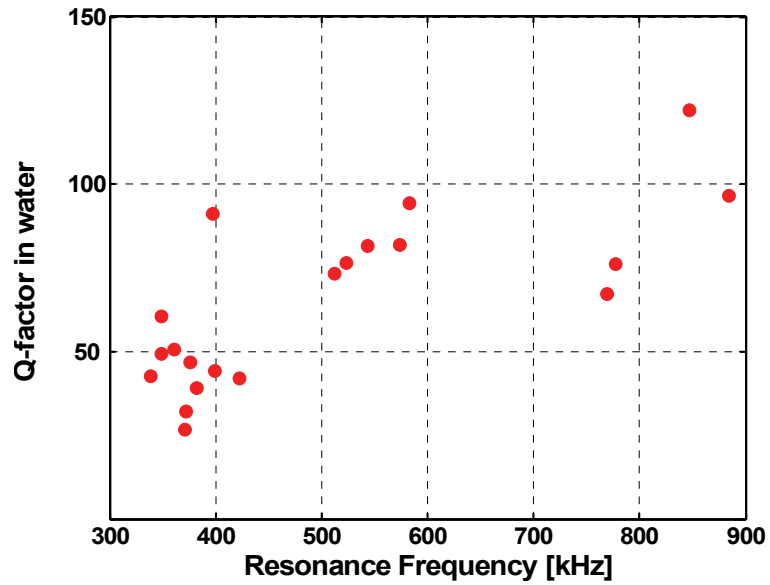
(a)
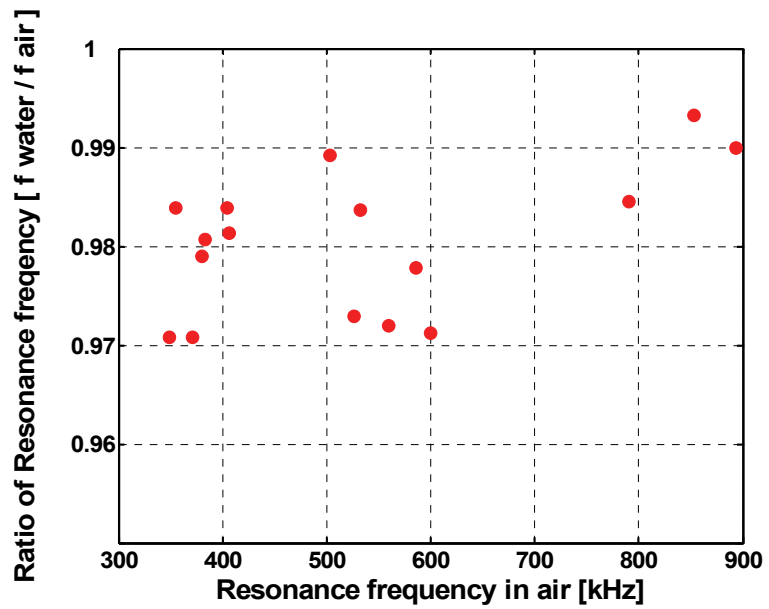
(b)

Figure 4.10: (a) Measured Q-factor in water as a function of resonance frequency, (b) ratio of resonance frequency in water to that in air as a function of the resonance frequency in air.

4.1.4 Quality Factor in Vacuum

The Q-factor of the resonators with thick passivation layers in air is lowered by a factor of 2~3 compared to those with thin passivation layers as can be noted in Figure 4.7. This means that the internal energy loss is no longer negligible compared to the viscous damping. To estimate the energy loss by internal friction compared to the viscous damping loss, the Q-factor of the disk resonators were also measured in vacuum.

Depending on the dominant damping mechanism of the microresonator, the pressure dependence of the Q-factor is generally divided into three regions: the intrinsic, the molecular and the viscous region [69]. In the intrinsic region, the Q-factor is limited by internal damping mechanisms such as thermoelastic damping, support loss, and energy losses associated with volume and surface defects of the resonator. As the pressure increases, the damping caused by random collision of non-interacting air molecules with the vibrating resonator becomes dominant (molecular region). In the viscous region, the air molecules interact with each other and behave like a viscous fluid and the Q-factor is limited by the viscous damping loss.

To estimate the internal damping loss, disk resonators passivated with 3μm PECVD oxide/nitride stacks were placed inside a vacuum chamber and amplitude transfer characteristics were recorded at air pressures below 1 Pascal (intrinsic region). Figure 4.11 shows the Q-factors in vacuum as a function of the resonance frequencies of the used disk resonators along with the Q-factors at atmospheric pressure. The Q-factors in air and in vacuum are marked with diamonds and circles, respectively. The highest Q-factor measured in vacuum is around 9500 and typically the Q-factors in vacuum are only around 2.5 times higher than the ones measured in air.
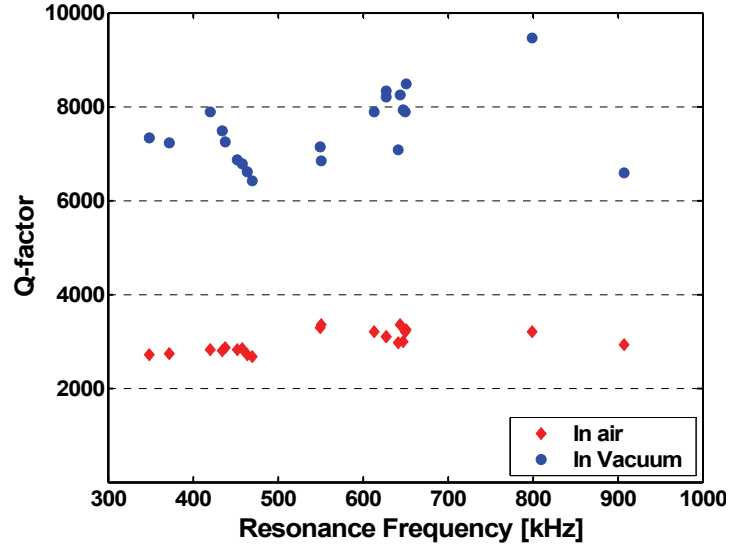
Figure 4.11: Q-factors of disk resonators in vacuum and at atmospheric pressure as a function of the resonance frequency.

The Q-factors associated with the internal damping loss (Q_{int}) and the viscous damping loss ($Q_{viscous}$) are extracted from the measured Q-factors at atmospheric pressure (Q_{air}) and in vacuum (Q_{vacuum}):

$$\frac{1}{Q_{viscous}} = \frac{1}{Q_{air}} - \frac{1}{Q_{vacuum}}$$

$$Q_{int} = Q_{vacuum}$$

(4.1)

Figure 4.12 is the plot of the extracted ratio of $Q_{viscous}$ to Q_{int}. The internal damping is 55~75% of the viscous damping when 3 μm PECVD passivation layers are used. This means that the internal energy loss constitutes a substantial part of the total energy loss. These issues will be further discussed in Section 5.3.2.
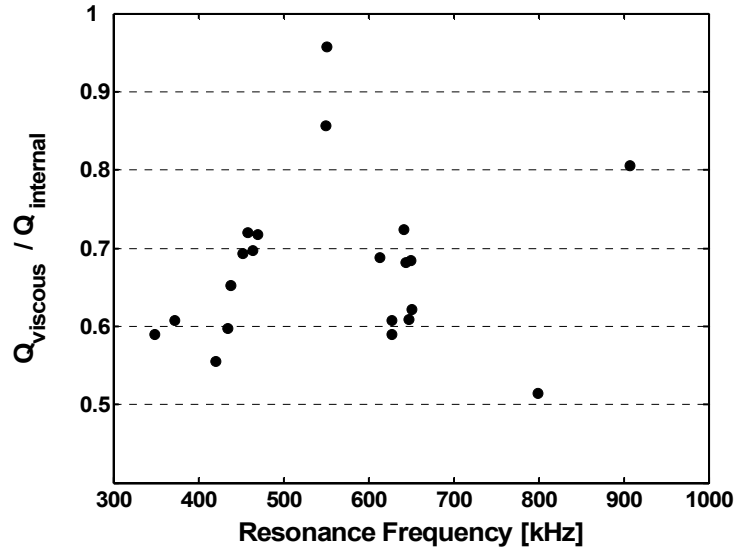
Figure 4.12: Extracted ratio of Q-factor by viscous damping to that by internal damping.

4.2. Closed Loop Characteristics

For the application as a resonant sensor, the microresonators are generally incorporated as the frequency-determining element in a self-oscillating, amplifying feedback loop. The resonance frequency of a resonator in a feedback loop fluctuates continuously not only caused by the measurand but also either by mechanical or electrical disturbances. The frequency fluctuation by these disturbances sets the limit for the minimum detectable frequency change of the resonator. The minimum detectable frequency change or frequency resolution of the designed disk resonators is estimated in this section by measuring the short-term frequency stabilities using the Allan variance method [74].

Besides its short-term frequency stability, the temperature coefficient of the resonance frequency (Tcf) is another important property of the resonator. Changes in temperature influence the frequency output and can be misinterpreted as a change in measurand, thus affecting the sensor resolution. The Tcf of the disk resonators is

estimated by measuring the resonance frequency change subject to varying temperature from -30~70°C.

4.2.1 Short-Term Frequency Stability

To estimate the short-term frequency stability of the disk resonators, an amplifying feedback loop is implemented on a printed circuit board as shown in Figure 4.13.
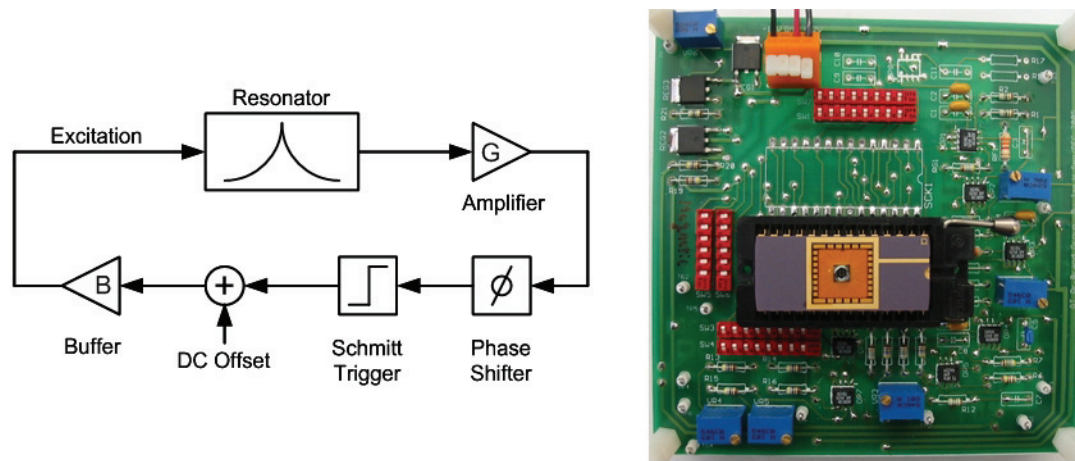
Figure 4.13: Schematic of amplifying feedback and printed circuit board designed for frequency stability measurements; G: Amplifier, B: Buffer.

The piezoresistive Wheatstone bridge signal is amplified and fed to a phase adjusting circuit (all-pass filter) to ensure the overall system acts as a positive feedback loop at the resonance frequency. The phase-tuned signal is then applied to an output voltage limiting Schmitt-trigger circuit, which extracts the phase information of the signal and at the same time adjusts the amplitude of the generated square-wave signal. Thereafter, a DC bias voltage is added to the square-wave signal and applied to the heating resistors, thus closing the loop. A more detailed description of the feedback loop will be given in Chapter 6. Because the frequency spectrum of the integrated Wheatstone

bridge signal exhibits a strong signal only at the chosen resonance frequency (see Figure 4.2), stable operation of the resonators in an amplifying feedback loop is realized without any additional filter circuits, thus simplifying the implementation of the positive feedback loop.

The short-term frequency stability of the designed resonators is measured both in air and in water using the Allan variance method [74] with an integration time (gate time) of 1 sec. The Allan variance (σ) is defined as

$$\sigma^2(\tau, m) = \frac{1}{2m} \sum_{n=1}^{m} (\gamma_{n+1} - \gamma_n)^2 \, , \, \gamma_n = \frac{f_{n+1} - f_n}{f_n} \tag{4.2}$$

where τ is the gate time, and m the number of measured data points.

The piezoresistive Wheatstone bridge with 450 Ω resistors is biased with 1.5 V_{DC} and a square wave AC signal with 0.4 V peak amplitude superimposed with a 0.5 V_{DC} offset voltage is applied to the 900 Ω heating resistors for the measurement in air. The estimated static power dissipations for biasing the Wheatstone bridge and for the thermal excitation are 5 mW and 0.7 mW, respectively, in this case. Thirty minutes were allowed for system warm-up before starting the resonance frequency measurements to ensure the circuit board and frequency counter reach their thermal equilibrium condition and, thus, to minimize the influence of the equipment on the frequency stability measurement. At the same time, at least 10,000 data points (= 10,000 sec) were recorded to improve the reliability of the estimated Allan variance.

To extract the short-term frequency stability in water, a PMMA flow cell (for details see Chapter 7) is mounted on top of the DIL packages with the bonding wires and metal pads protected with epoxy, as explained in Figure 4.8. During the measurement, the water flow rate through the flow cell is kept constant at 8 μL/min using a syringe pump.

The measurement results for resonators with different dimensions are summarized in Table 4.1, showing that Allan variances in the low 10^{-8} range are generally achieved in air. Frequency stabilities as low as 1.07×10^{-8} and 2.3×10^{-6} are extracted from the

measurement results in air and in water, respectively. Compared to the frequency stability of cantilever type resonators of up to 9×10^{-8} (τ=1sec) [75], the designed disk resonators showed an almost 10 times better short-term frequency stability. Figure 4.14 shows the Allan variance in air and water as a function of the gate time. To obtain the Allan variance for gate times larger than 1 sec, neighboring data points from the measured data with 1 sec gate time have been averaged. The calculated Allan variance of the disk resonators is getting worse with increasing gate time as shown in Figure 4.14. This is likely due to resonance frequency drift with time. As the resonators are operated in an uncontrolled environment during the experiment, temperature induced frequency drift may cause such an increase in the calculated Allan variance at longer gate times.

It is worth mentioning that the measured short-term frequency stability depends not only on the mechanical resonator itself but also on the electronic circuitry used for implementing the feedback loop. Therefore, an improved feedback loop circuitry would potentially improve the measured frequency stability of the resonators.

Table 4.1: Summary of measured short-term frequency stability in air/water
with gate time of 1 second.

Dimensions [µm]	Resonance Frequency	Allan Variance	
r_1=140, r_2=50, w_1=35, w_2=30, g=15, l=480	411.0 kHz	1.50×10^{-8}	in air
r_1=140, r_2=40, w_1=35, w_2=30, g=15, l=480	421.5 kHz	2.62×10^{-8}	in air
r_1=140, r_2=40, w_1=35, w_2=30, g=20, l=480	426.2 kHz	1.07×10^{-8}	in air
r_1=140, r_2=50, w_1=45, w_2=40, g=10, l=380	644.3 kHz	1.21×10^{-8}	in air
r_1=120, r_2=50, w_1=40, w_2=40, g=10, l=340	886.5 kHz	2.14×10^{-8}	in air
r_1=150, r_2=50, w_1=35, w_2=30, g=20, l=500	321.5kHz	2.59×10^{-6}	in water
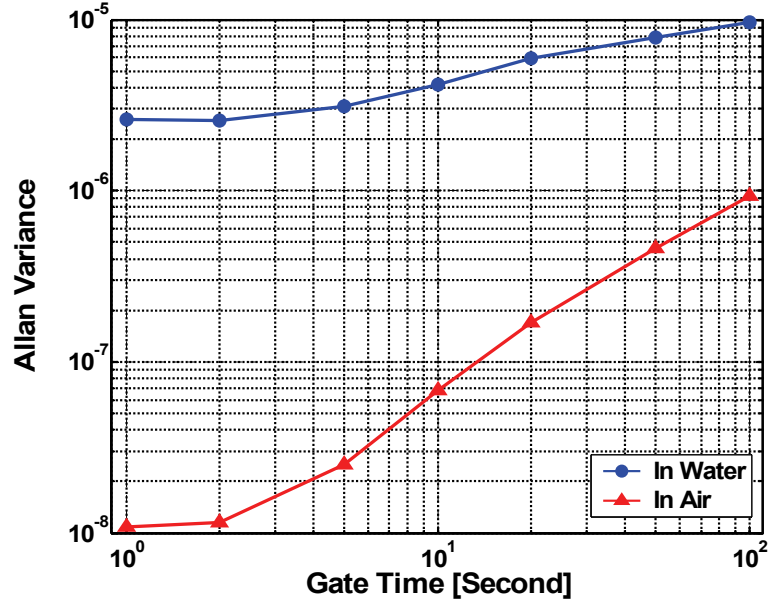
Figure 4.14: Allan variance σ in air and in water as a function of gate time.

4.2.2 Temperature Coefficient of Resonance Frequency

The frequency output of a resonant mass-sensitive sensor is affected by different environmental factors, such as temperature and humidity. Temperature is considered the most dominant cause for the drift of the resonance frequency of a mechanical resonator. The frequency sensitivity to temperature is represented by the temperature coefficient of the resonance frequency (TCf), and TCf values of -30 ~ -180 ppm/°C have been reported for silicon resonators [76].

The temperature dependence of the resonance frequency of a silicon resonator is affected by four major factors [77]: i) the vibration mode shape, ii) possible thin film coatings on the resonator surface, iii) temperature induced mechanical stress, e.g., due to the packaging, and iv) the crystal orientation of the silicon substrate. Depending on the vibration mode shape, e.g. longitudinal, shear, flexural or torsional modes, the resonance frequency is affected by different combinations of the moduli of elasticity, the Poisson's ratio, the density and the dimensions, each of which has different temperature

coefficients. Different thermal expansion coefficients of silicon substrate, thin film coatings, die-attach adhesive and packaging materials generate mechanical stress and, thus, also cause changes of the resonance frequency with temperature. In addition, the temperature coefficient of the Young's modulus depends on the silicon crystal orientation (-46 ~ -80 ppm/°C) as well [78].

To determine the TCf of the disk resonators investigated in this work, they are operated in an amplifying feedback loop and the resonance frequencies are measured as a function of temperature from -20°C to +70°C. During the measurement, the printed circuit board with the feedback circuit is kept outside the temperature chamber and connected to the resonator placed inside the chamber with a cable. To exclude the initial aging effect of the resonators, they are initially operated at a constant temperature until the frequency output stabilizes. To exclude the influence of the packaging on the measurement, photoresist is used as die-attach adhesive and is removed with acetone after wire bonding, thus not constraining the resonator chip to the (ceramic) substrate. The temperature of the test chamber is changed slowly during the measurement to assure that the resonator temperature is the same as the chamber temperature.

Figure 4.15 shows the resonance frequency change of a sample resonator (r_1 = 120 μm, r_2 = 50 μm, g = 15 μm) as a function of temperature. A TCf of ≈ -33 ppm/°C is extracted from the measurement, which is equivalent to a -66 ppm/°C relative stiffness change of the resonator. This temperature coefficient of the relative stiffness change is close to the temperature coefficient of the Young's modulus of a single crystalline silicon in the (100) direction [78]. However, depending on the dimensions and also on the fabrication process of the disk resonators, slight variations in TCf are observed with values ranging from -30 ~ -60 ppm/°C.
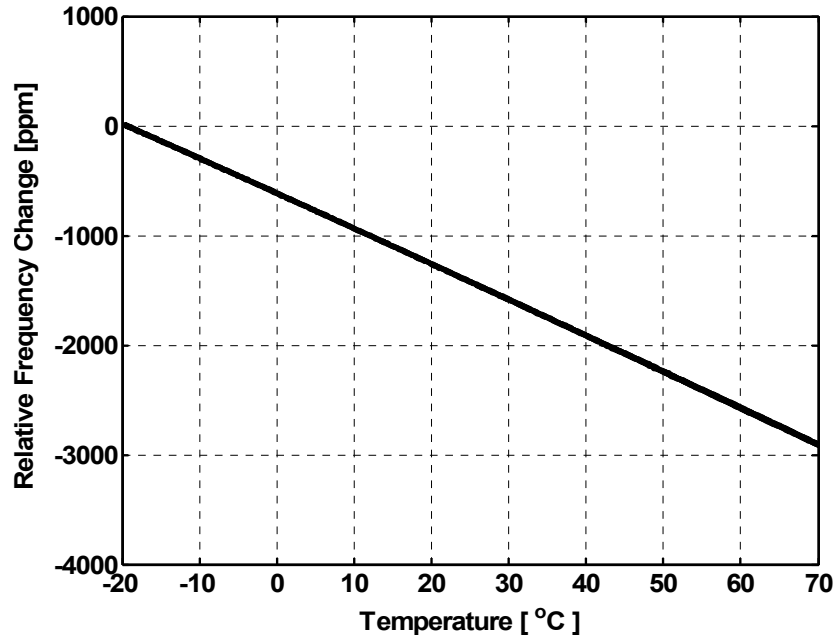
Figure 4.15: Relative resonance frequency change of a disk resonator ($r_1 = 120\mu m$, $r_2 = 50\mu m$, $g = 15\mu m$) as a function of temperature.

4.3. Parasitic Signal Coupling

A non-mechanical coupling between the excitation signal and the read-out signal of the resonators is unavoidable when using integrated excitation and detection elements, even though the magnitude of the crosstalk component can be reduced by careful design and layout of the excitation and detection elements. Electrical (e.g., via a small parasitic capacitance) and thermal (e.g., via the thermal bimorph effect) crosstalk are the possible coupling mechanisms. The capacitive crosstalk component of the detection signal increases with increasing operation frequency and depends on the way the excitation and detection elements are biased electrically. If the parasitic coupling signal is dominant compared to the signal originating from the resonator vibration, the transfer characteristic becomes distorted and the properties of the mechanical resonator (e.g., resonance frequency and quality factor) are difficult to extract experimentally. Furthermore, the

cross-talk signal might limit the operation of the resonator in an amplifying feedback loop.

One possible way of removing the crosstalk component mathematically is described in the following. Figure 4.16(a) shows the amplitude and phase response of a resonator in the complex plane. The vector $\vec{V}_{cp}$ (assumed to be frequency independent) denotes the crosstalk component in a detection signal and is added to the signal from the resonator, thus shifting the measured amplitude and phase response of a resonator as shown in Figure 4.16(b). In this case, the measured amplitude response of the resonator will exhibit a negative peak instead of a positive peak at the resonance frequency, as illustrated in the inset of Figure 4.16(b).

(a)   (b)
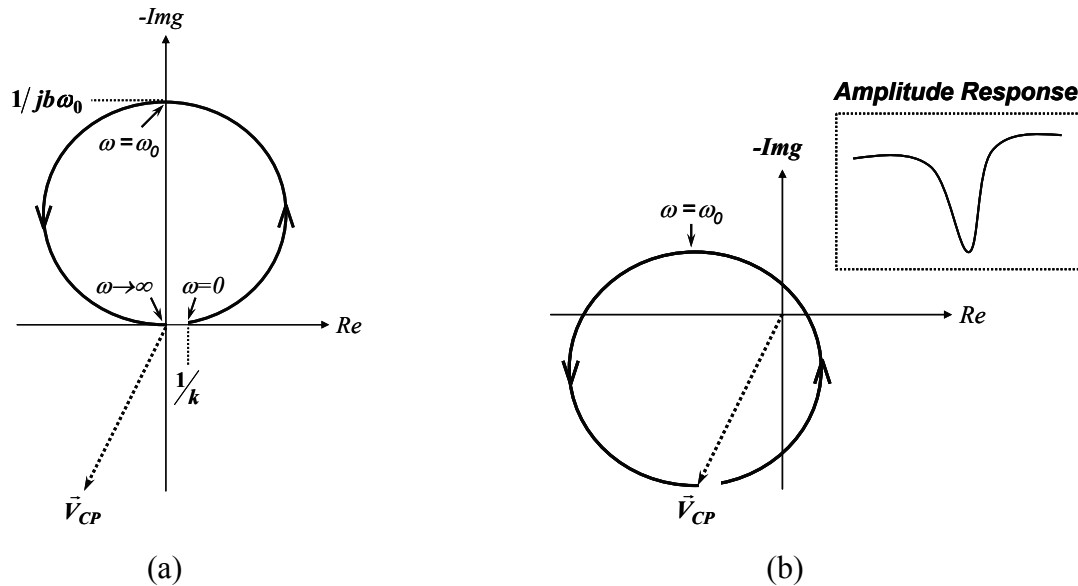
Figure 4.16: Influence of parasitic signal components on the measured frequency response of a resonator; (a) real and imaginary part of the transfer characteristic in the complex plane with the arrows indicating increasing excitation frequency, (b) distortion of the measured frequency response by a constant crosstalk component V_{CP}.

If the magnitude and phase of the crosstalk signal can be identified from the measured data, the undistorted frequency response of the resonator can be extracted mathematically. Let us assume that the measured amplitude and phase response of the resonator are given as shown in Figure 4.17. M_1, M_2, Φ_1, and Φ_2 denote the measured amplitude and phase response at frequencies f_1 and f_2, respectively. If f_1 and f_2 are far away from the resonance frequency, then M_1, M_2, Φ_1, and Φ_2 can be considered to be mainly coming from the crosstalk components.
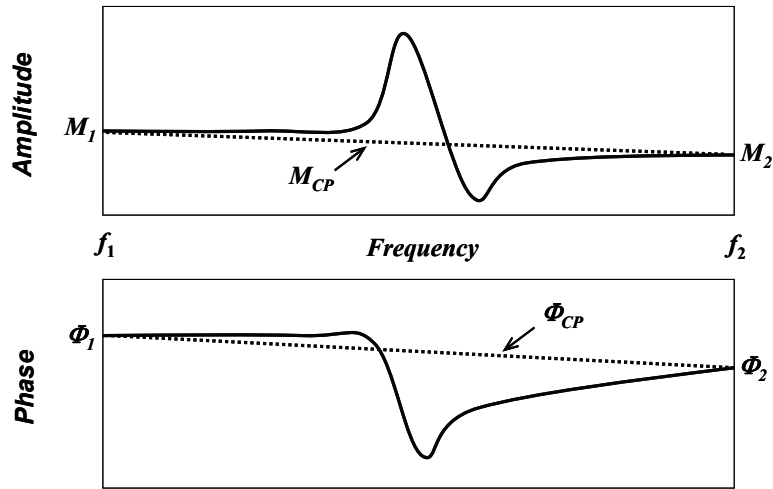
Figure 4.17: Magnitude and phase of the transfer characteristic of a resonator distorted by a crosstalk component.

Then the crosstalk component around the resonance frequency can be approximated as:

$$M_{CP}\angle\Phi_{CP} = \frac{M_1\angle\Phi_1 + M_2\angle\Phi_2}{2} \qquad (4.3)$$

Therefore, this crosstalk signal can be subtracted from the measured frequency response of the resonator. Figure 4.18 shows the measured frequency response (amplitude and

phase) of a disk resonator before and after subtraction of the coupling signal as explained above, demonstrating the effectiveness of this mathematical crosstalk elimination.
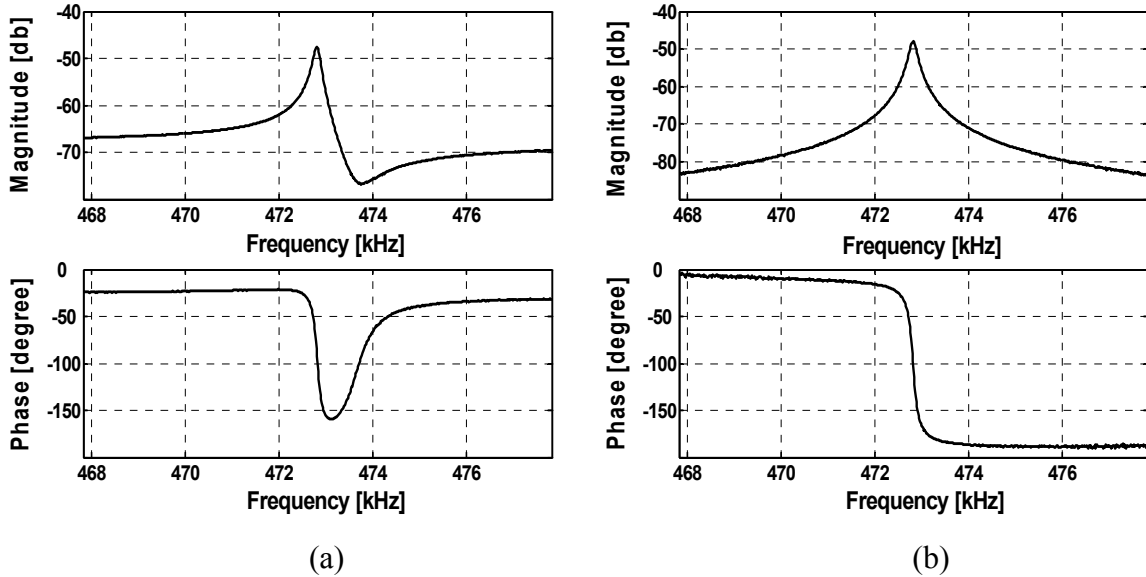
Figure 4.18: Mathematical subtraction of crosstalk components from the measurement result; (a) measured frequency response of a resonator, (b) frequency response after subtraction of cross-coupling component.

It should be noted however that such a mathematical procedure can not be applied in case of the closed-loop operation of the resonators. Here, a proper design must ensure minimal signal crosstalk, so that stable operation of the resonator in the feedback circuit can be achieved. To reduce mechanical cross-coupling, the resonance mode of interest should be far away from all other resonance modes by proper selection of structure dimensions to minimize interferences between resonance modes. And for reduced electrical cross-coupling, parasitic capacitances between excitation and detection elements, and also capacitance between conductor lines carrying excitation and detection signals should be minimized by allowing sufficient distances between them. Furthermore, proper selection of passivation materials with low dielectric constant is another way to

reduce coupling capacitances, i.e. silicon dioxide is preferred over silicon nitride as the first passivation layer.

4.4. Discussions and Conclusions

The disk resonators were extensively characterized in terms of their Q-factor, their short-term frequency stability and their temperature coefficient of the resonance frequency. Compared to transversally vibrating resonators, i.e. cantilever-type resonators, the disk-type resonator showed improved performance both in air and in water. However, the Q-factor dependence on the chosen fabrication processes needs to be characterized in more detail for further performance improvement of the disk resonator. Moreover, it is worth investigating the out-of-phase resonance mode in detail in the future by proper modification of the piezoresistive Wheatstone bridge layout.

CHAPTER 5

ANALYTICAL MODELING

In the preceding chapter, the experimental characterization of the designed disk resonator both in air and in water has been summarized, showing that measured quality factors and resonance frequencies are closely related to the resonator dimensions. While general design guidelines can be obtained from the experimental data, optimization of the microstructure dimensions solely based on the measured characteristics is challenging. For proper design optimization, the experimental data must be complemented by appropriate numerical and/or analytical simulation results. While numerical modeling approaches, such as finite element modeling (FEM), can be used to accurately predict e.g. the resonance frequencies and vibration modes of even complex microstructures (see Chapter 3), they are generally less suitable for a design optimization, as geometrical dependencies can not be directly extracted. In addition, numerical methods are often time consuming and resource intensive. On the other hand, analytical modeling approach can provide a more direct and flexible path to structure optimization, establishing mathematical relationships between the properties of interest (in this work, the resonance frequencies and the quality factors) and the microstructure dimensions. Even though a precise analytical model is not easy to develop, a simplified analytical model derived under simplifying assumptions can be sufficient for design optimization, especially when combined with the accuracy of numerical modeling methods.

In this chapter, analytical models for the resonance frequency and Q-factor of the investigated disk resonators are presented. The mechanical system constants, which determine the resonance frequencies of the resonators, are derived from simple beam bending theory. Moreover, the quality factor of the resonators is derived using the

83

Navier-Stokes equation under the assumption that the viscous damping becomes the dominating energy dissipation source, when the disk resonators are operated in air or a liquid environment. The obtained analytical expressions and values are compared both with FEM data and experimental results.

5.1. Modeling of Mechanical System Constants

The analytical system modeling of the disk-type resonators is based on the torque or moment equation for an object executing rotational motion around its axis of rotation

$$J\ddot{\theta} + B\dot{\theta} + K\theta = T \tag{5.1}$$

where J, B, K, θ and T are the rotational moment of inertia, the damping coefficient, the torsional spring constant, the angular displacement and the externally applied torque, respectively. The mechanical system constants, J and K of Equation (5.1), and the resonance frequencies of the in-phase and the out-of-phase resonance modes are derived in the following under the assumption of weak damping.

5.1.1 Rotational Spring Constant

To derive an expression for the rotational spring constant of the in-phase resonance mode shape shown in Figure 3.3(a), the proposed microstructure is assumed to be composed of two spring systems connected in series: K_θ and K_S denote the rotational spring constants of the anchor beam and the support beam of Figure 3.1, respectively. In contrast, the rotational spring constant of the out-of-phase resonance mode shown in Figure 3.3(b) is determined by K_S only, because the anchor beam is not moving in this case.

The rotational spring constant of the anchor beam K_θ, defined by the ratio of the applied torque to the resulting angular displacement at the center of the beam, is derived

from well-defined stress-deflection relationships of a clamped-clamped beam structure [79, 80].
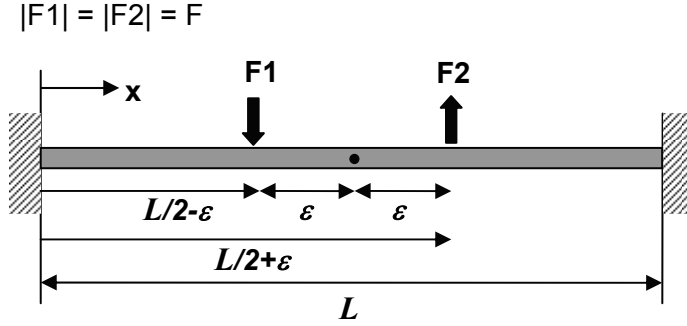
Figure 5.1: Derivation of rotational spring constant K_θ of the anchor beam from force-deflection relationships of clamped-clamped beams.

The analytical expression for the deflection $y(x)$ of a clamped-clamped beam (as a function of distance x from the clamped edge), subject to forces $|F_1| = |F_2| = F$ as shown in Figure 5.1, is [80]

$$y(x) = -\frac{F}{EI}\left(\frac{(\frac{L}{2}+\varepsilon)\cdot(\frac{L}{2}-\varepsilon)\cdot\varepsilon}{L^2}x^2 - \frac{(\frac{L}{2}+\varepsilon)^2\cdot(L-\varepsilon)-(\frac{L}{2}-\varepsilon)^2\cdot(L+\varepsilon)}{3L^3}x^3 + \frac{1}{6}(x+\varepsilon-\frac{L}{2})^3 \right) \quad (5.2)$$

where F, E, I, L and ε denote the magnitude of the applied force, the apparent Young's modulus, the moment of inertia, the beam length, and the distance from the beam center to the point of the applied force, respectively. Then, the slope dy/dx at the center of the beam is determined by

$$\left.\frac{dy(x)}{dx}\right|_{x=L/2} = -\frac{F}{EI}\left(\frac{(\frac{L}{2}+\varepsilon)\cdot(\frac{L}{2}-\varepsilon)\cdot\varepsilon}{L} - \frac{(\frac{L}{2}+\varepsilon)^2\cdot(L-\varepsilon)-(\frac{L}{2}-\varepsilon)^2\cdot(L+\varepsilon)}{4L} + \frac{1}{2}\varepsilon^2 \right) \quad (5.3)$$

Therefore, the anchor beam's rotational spring constant K_θ is derived as

$$K_\theta = \frac{T}{\theta} = \lim_{\varepsilon \to 0} \left(\frac{2\varepsilon F}{\tan^{-1}\left[\left. \dfrac{dy}{dx} \right|_{x=L/2} \right]} \right) = \frac{16 \cdot E \cdot I_1}{L} \quad \text{with} \quad I_1 = \frac{t \cdot w_1^3}{12} \qquad (5.4)$$

with the thickness t and width w_1 of the anchor beam.

While deriving the rotational spring constant K_S of the support beam shown in Figure 3.1, shear stresses have to be considered in addition to bending stresses, because the support beam has small a aspect ratio (length-to-thickness ratio = $(r_2 - w_1/2)/w_2$) [80]. In case of long beams with aspect ratios larger than 10, shear stresses are much smaller than the bending stresses and can generally be neglected in estimating the total deflection [80]. Considering the small aspect ratio of the support beams between 0.75 ~ 1, the rotational spring constant K_S can be determined as:

$$K_S^{-1} = \alpha^{-1} \left(\left[\frac{2 \cdot E \cdot I_2}{l_S} \right]^{-1} + \left[\frac{E \cdot t \cdot w_2 \cdot l_S}{2 \cdot (1 + v_m)} \right]^{-1} \right)$$

$$I_2 = \frac{t \cdot w_2^3}{12}, \quad l_S = r_2 - \frac{w_1}{2} \qquad (5.5)$$

where $E, t, w_1, w_2, l_S,$ and v_m are the Young's modulus of the beam, the beam thickness, the width of the anchor beam, the support beam width, the effective support beam length, and the Poisson's ratio, respectively. The first term of the right-hand side of Equation (5.5) originates from the deflection due to beam bending, while the second term accounts for the deflection due to beam shearing.

However, the shear deflection of short beams with aspect ratios less than 3 does not follow the simple theory of flexure, which is based on a linear stress distribution [79, 80]. To account for the non-linearity of the shear deflection at small aspect ratio [81] and to obtain a more accurate analytical model for the rotational spring constant K_S of the support beam, a correction factor α is introduced to Equation (5.5). The value of the correction factor α is derived using numerical FEM simulation. For the FEM simulation,

a clamped-free beam with length l_S is used. A concentrated mass m with small volume but high mass density is attached at the tip of the beam for direct estimation of the effective mass moment of inertia. From the simulated eigen-frequency of the beam, the correction factor α is extracted. As the correction factor depends on the beam length l_S, i.e for l_S = 22.5 μm, α = 1.39 and for l_S = 32.5 μm, α = 1.69, the mean value of the extracted correction factor of α=1.5 is used for further mechanical system modeling.

5.1.2 Mass and Rotational Moment of Inertia

Figure 5.2 illustrates the approach taken to estimate the mass M and the rotational moment of inertia J of the disk-type microstructure. Only the two semi-disks and the two support beams are considered in deriving M and J, assuming that the inertial energy stored in the anchor beam does not contribute to the total inertial energy of the structure at the chosen in-plane resonance modes. Under this assumption, the effective inertia for the two resonance modes shown in Figure 3.3 has the same value. At the same time, the device thickness is considered to be small compared to the other structure dimensions in the calculation of J. Mass and rotational moment of inertia are first calculated for a full disk with radius r_1 (see Figure 5.2, schematic (1)). Subsequently correction terms are introduced (see Figure 5.2, schematics (2) through (5)) to more accurately model the real device geometry.
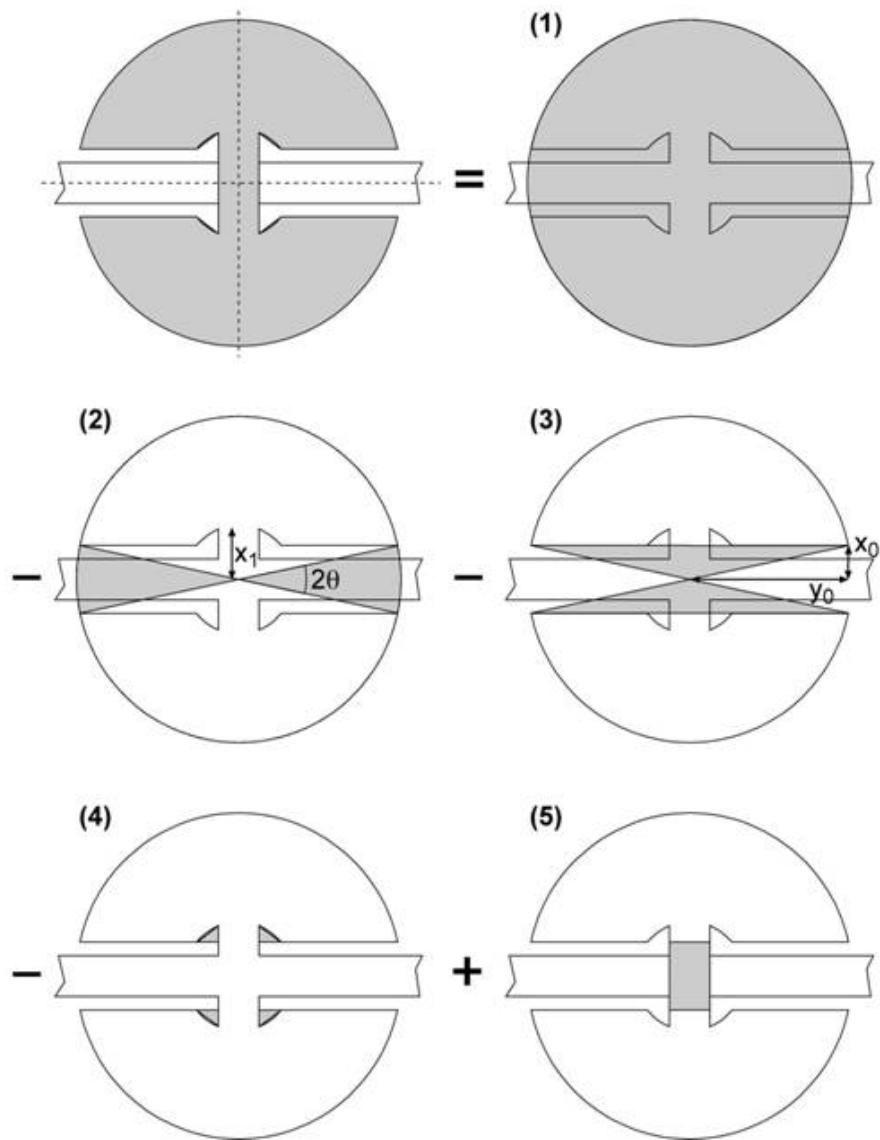
Figure 5.2: Schematic of the disk resonator showing the approach used to calculate the mass, rotational moment of inertia and viscous friction; the calculations start with the assumption of a full disk (1) and then introduce correction terms (2) through (5) to more closely model the real geometry. In case of the viscous damping, (4) and (5) are neglected, but the viscous damping caused by the side walls is considered.

With the variables defined in Figure 3.4 and Figure 5.2, the mass of a proposed microstructure is expressed by

$$M = \rho \cdot t \cdot \left[\pi \cdot r_1^2 - 2 \cdot \theta_0 \cdot r_1^2 - 2 \cdot x_0 \cdot y_0 - 2 \cdot (x_1 - x_0)^2 + 2 \cdot x_0 \cdot w_2 \right]$$

$$x_0 = \frac{w_1}{2} + g, \quad x_1 = \sqrt{r_2^2 - \left(\frac{w_2}{2}\right)^2}, \quad y_0 = \sqrt{r_1^2 - x_0^2}, \quad \theta_0 = tan^{-1}\left(\frac{x_0}{y_0}\right)$$

(5.6)

where ρ is the density of a resonator. The individual terms in Equation (5.6) correspond to the contributions of the respective gray areas in the schematics (1) through (5) of Figure 5.2.

From the definition of the moment of inertia J, where r is the distance from the rotation axis to the differential mass element dm, the rotational moment of inertia of the resonator is calculated in a similar way

$$J = \int r^2 dm$$

$$= \rho \cdot t \cdot \left[\frac{\pi}{2} r_1^4 - \frac{\theta_0}{2} r_1^4 - x_0 y_0 \left(x_0^2 + \frac{y_0^2}{3} \right) - \left(\frac{2}{3} x_1^4 + 2 x_0^4 - \frac{8}{3} x_0^3 x_1 \right) + \frac{w_2 x_0}{6} (4 x_0^2 + w_2^2) \right]$$

(5.7)

Again, the individual terms correspond to the shaded areas in schematics (1) through (5) of Figure 5.2.

5.1.3 Resonance Frequency of a Disk Resonator

The rotational spring constants of the proposed resonators in the two rotational in-plane eigenmodes are expressed by

$$K_{IPR}^{-1} = K_\theta^{-1} + K_S^{-1}$$
$$K_{OPR} = K_S$$

(5.8)

where K_{IPR} and K_{OPR} denote the spring constants of the in-phase and out-of-phase resonance modes shown in Figure 3.3, respectively. Based on the derived rotational spring constant K and the rotational moment of inertia J, the resonance frequencies of the two in-plane eigenmodes are determined. The resonance frequencies of the in-phase

resonance mode ω_{IPR} and out-of-phase resonance mode ω_{OPR} are derived from Eqs. 5.7 and 5.8 as

$$\omega_{IPR} = \sqrt{\frac{K_{IPR}}{J}}, \qquad \omega_{OPR} = \sqrt{\frac{K_{OPR}}{J}} \qquad (5.9)$$

5.2 Modeling of Quality Factor

5.2.1 Viscous Damping

To estimate the viscous damping of the designed disk resonator, a plane disk, subject to rotary harmonic oscillations with small amplitude, immersed in an incompressible linear viscous fluid is considered here. If the disk radius is much larger than the penetration depth δ of the shear wave generated in the surrounding fluid, edge effects can be neglected and the fluid velocity profile caused by the disk movement can be calculated similar to the case of a disk with "infinite" radius. The penetration depth δ

$$\delta = \sqrt{\frac{2 \cdot \nu}{\omega}} \qquad (5.10)$$

is the distance from the oscillating solid surface, at which the amplitude of the fluid velocity decays by a factor of e^{-1} [82-84]. The penetration depth is a function of the oscillating frequency ω of the solid body and the kinematic viscosity ν of the fluid which is defined as

$$\nu = \frac{\eta}{\rho} \qquad (5.11)$$

where η is the dynamic viscosity and ρ is the density of the fluid. Values for the kinematic viscosity ν and the dynamic viscosity η of air and water are summarized in Table 5.1 along with the resulting penetration depth δ of the shear wave at two specific oscillation frequencies.

Table 5.1: Kinematic and dynamic viscosity of air and water at 20˚C
and penetration depth of the shear wave at 300 kHz and 1 MHz.

Fluid	Dynamic Viscosity (η) [Pa·s]	Kinematic Viscosity (v) [m^2/s]	Penetration Depth (δ) @ 300kHz/1MHz [μm]
Air	1.82×10^{-5}	1.51×10^{-5}	4.0 / 2.19
Water	1.002×10^{-3}	1.004×10^{-6}	1.03 / 0.56

A disk of radius $r \gg \delta$ is assumed to execute rotary oscillations with a small angular rotation amplitude θ_i ($\theta_i \ll 1$), i.e. $\theta = \theta_i \cos(\omega t)$. In cylindrical coordinates, with the axis of rotation parallel to the z-axis, the resulting fluid velocity field u must satisfy the following conditions [82, 83]

$$u_\phi = r \cdot \Omega(z,t) \quad with \quad \Omega(z,t) = f(z) \cdot e^{-j\omega t}$$
$$u_R = u_Z = 0$$

(5.12)

where u_ϕ, u_R and u_Z are the velocity components of the fluid in angular, radial and z direction, respectively, and the angular velocity $\Omega(z,t)$ is a function of the distance z from the solid surface (normal to the surface of oscillating disk) and time t.

The fluid velocity profile is determined by the Navier-Stokes equation [82]

$$\frac{\partial u}{\partial t} + u \cdot \nabla u = -\frac{\nabla p}{\rho} + v\nabla^2 u$$

(5.13)

with the velocity vector u and the hydraulic pressure p. By assuming small amplitude oscillations and zero pressure gradients due to laminar flow, the second term on the left hand side and first term on the right hand side of Equation (5.13) can be neglected and the Navier-Stokes equation is simplified to

$$\frac{\partial u}{\partial t} = v\nabla^2 u$$

(5.14)

By combining Equation (5.12) with (5.14), the angular velocity Ω is described by the following differential equation in cylindrical coordinates:

$$\frac{\partial \Omega(z,t)}{\partial t} = v\left(\frac{\partial^2 \Omega(z,t)}{\partial z^2} - \frac{\Omega(z,t)}{r^2}\right) \tag{5.15}$$

Under the assumption of an infinite disk radius ($r \gg \delta$), the second term on the right hand side of the above equation is neglected in the further derivation, and Equation (5.15) can be simplified:

$$\frac{\partial \Omega(z,t)}{\partial t} = v\frac{\partial^2 \Omega(z,t)}{\partial z^2} \tag{5.16}$$

The trial solution $\Omega(z,t) = f(z)\cdot e^{-j\omega t}$ in Equation (5.12) is used to find a solution for Equation (5.16). By assuming that the angular displacement of the fluid on the resonator surface is $\theta(0,t) = \Re\{\theta_i \cdot e^{-j\omega t}\} = \theta_i \cos(\omega t)$, the angular velocity of the fluid is determined by $\Omega(z,t) = \Re\{f(z)\cdot e^{-j\omega t}\}$. Equation (5.16) and the boundary conditions, $\Omega(z{=}0) = d\theta/dt = -\omega\theta_i \sin(\omega t)$ and $\Omega(z{=}\infty) = 0$, can be rewritten in terms of $f(z)$:

$$v\frac{\partial^2 f(z)}{\partial z^2} + j\omega f(z) = 0$$
$$f(z=0) = -j\omega\theta_i \tag{5.17}$$
$$f(z=\infty) = 0$$

The solution $f(z)$ is derived from the eigenvalues (λ) of the above equation as

$$\lambda = \pm\sqrt{\frac{-j\omega}{v}} = \pm\frac{1}{\delta}(1-j)$$
$$f(z) = -j\omega\theta_i e^{-\frac{1}{\delta}(1-j)z} \tag{5.18}$$

Then, the resulting angular velocity profile of the fluid, generated by the vibrating disk, is determined as:

$$\Omega(z,t) = \Re\left\{-j\omega\theta_i e^{-\frac{1}{\delta}(1-j)z} e^{-j\omega t}\right\} = \Re\left\{-\omega\theta_i e^{-\frac{z}{\delta}} e^{j\left(\frac{\pi}{2}+\frac{z}{\delta}-\omega t\right)}\right\} = -\omega\theta_i e^{-\frac{z}{\delta}} \sin\left(\omega t - \frac{z}{\delta}\right) \tag{5.19}$$

The shear stress $\sigma_{\phi z}$ in the fluid can be derived from the equation of motion for a linear incompressible viscous fluid [82]:

$$\sigma_{\phi Z} = \eta \left(\frac{\partial u_\phi}{\partial z} + \frac{1}{r} \frac{\partial u_z}{\partial \phi} \right) = \eta \frac{\partial u_\phi}{\partial z} = \frac{\sqrt{2} \eta \cdot r \cdot \omega \cdot \theta_i}{\delta} \cdot e^{-\frac{z}{\delta}} \cdot sin \left(\omega t - \frac{z}{\delta} + \frac{\pi}{4} \right) \tag{5.20}$$

Finally, the frictional energy loss on the disk surface per oscillation cycle is obtained by [82, 84, 85]

$$E_{loss} = \frac{1}{\omega} \int\limits_0^{2\pi} \left(\int \sigma_{\phi z}(z=0) \cdot u_\phi(z=0) \cdot ds \right) \cdot d(\omega t) \tag{5.21}$$

with the differential area of the disk surface dS.

5.2.2 Quality Factor

In this section, an analytical expression for the quality factor of the disk resonator is derived under the assumption that viscous damping is the dominant loss mechanism. The procedure of extracting the net energy loss E_L of the microstructure using Equation (5.21) is described in Figure 5.2. The energy loss E_{L1} of a full disk with radius r_1 is calculated first and the contributions E_{L2} and E_{L3} (shaded areas (2) and (3) of Figure 5.2) are subsequently subtracted. The energy loss E_{L4}, originating from viscous losses along the outer sidewalls of the two semi-disks, is considered as well in estimating the total energy loss E_L. Thus, the energy loss is ultimately obtained by integrating only over the surface area of the two semi-disks and not the surface area of a full disk. It should be noted, that the viscous damping on the support beam and anchor beam area is assumed negligible compared to the energy loss on the surface of the two semi-disks. Eqs. (5.22) through (5.25) are derived from Equation (5.21) considering frictional energy losses on both sides of the structure.

$$E_{L1} = \frac{\eta \pi^2 \omega \theta_i^2}{\delta} \cdot r_1^4 \tag{5.22}$$

$$E_{L2} = \frac{2\eta \pi \omega \theta_i^2 \theta_0}{\delta} \cdot r_1^4 \tag{5.23}$$

$$E_{L3} = \frac{2\eta\pi\omega\theta_i^2}{\delta}\left(\theta_1 r_1^4 - r_1^4 \cdot cos^{-1}\left(\frac{x_0}{r_1}\right) + \frac{r_1 x_0 \left(r_1^2 + 2x_0^2\right)}{3}\sqrt{\frac{r_1^2 - x_0^2}{r_1^2}}\right) \quad (5.24)$$

$$E_{L4} = \frac{4\eta\pi\omega\theta_i^2}{\delta} \cdot \theta_1 t_1 r_1^3 \quad (5.25)$$

Finally, the Q-factor is derived from the ratio of the maximum stored kinetic energy E_S to the energy loss per cycle E_L at the resonance frequency ω_0:

$$Q = 2\pi \frac{E_S}{E_L} \approx \left.\frac{J\omega^2\theta_i^2\pi}{\left(E_{L1} - E_{L2} - E_{L3} + E_{L4}\right)}\right|_{\omega=\omega_0} \quad (5.26)$$

The mass loading effect by the fluid and the squeezed film damping appearing at the air gap between the semi-disk and the anchor beam are not included in this equation. By approximating the two semi-disks as a full circular disk, where $M \approx \pi \cdot \rho_{si} t \cdot r_1^2$ (ρ_{Si} : density of silicon), $J \approx r_1^2 \cdot M/2$ and $E_L = E_{L1}$, Equation (5.26) can be further simplified. Then, the Q-factor can be approximated as

$$Q \approx \frac{\omega_0 \delta J}{\eta\pi R_1^4} \approx \frac{\omega_0 \delta M}{2\eta\pi R_1^2} \approx \sqrt{\frac{v\omega_0}{2}} \cdot \frac{\rho_{si} t}{\eta} = \frac{\rho_{si}}{\rho_a} \cdot \frac{t}{\delta} \quad (5.27)$$

where ρ_a is density of the fluid. Equation (5.27) implies that the Q-factor is proportional to the device thickness and the square root of the resonance frequency. Therefore, to improve the Q-factor of the disk-type resonator at a given resonator mass or inertia, structures should be designed to have a high rotational spring constant.

5.3 Comparisons with Experimental Results

5.3.1 Resonance Frequency

Using the developed analytical model, the resonance frequencies of disk resonators with various dimensions have been calculated and compared with values obtained from FEM simulations and experimental data for both of the in-plane eigenmodes. The

following mechanical properties of (100) single crystalline silicon are used for the analytical calculations and the numerical simulations: Young's modulus $E = 120$ [GPa], Poisson's ratio $\nu = 0.27$ and density $\rho = 2330$ [kg/m^3]. The chosen Young's modulus is lower than the literature value for silicon ($E = 130$ [GPa] in <100> direction [78]) to account for the passivation layers in the model. The FEM model is based on a homogeneous single material disk. This way, the Young's modulus plays the role of a fit parameter to match experimental and FEM data. To experimentally detect the out-of-phase resonance frequency, the excitation signals and the external circuitry to read-out the piezoresistive Wheatstone bridge signal was modified as described in Chapter 4.1 (see Figure 4.3).

The measured in-phase and out-of-phase resonance frequencies of various disk resonators are plotted in Figure 5.3 along with the frequencies obtained from analytical calculations and numerical simulation results. The resonance frequencies estimated from the analytical model match quite well with those from the FEM simulation and the measurement results, demonstrating the applicability of the developed analytical model. It should be noted that FEM simulation results are used in deriving the analytical expression for the resonance frequency to account for the non-linear shear deflection of the short support beams. Therefore, the correction factor α in Equation (5.5) must be modified properly when the aspect ratio of the support beam is changed substantially from the current structure dimensions.

(a)

(b)
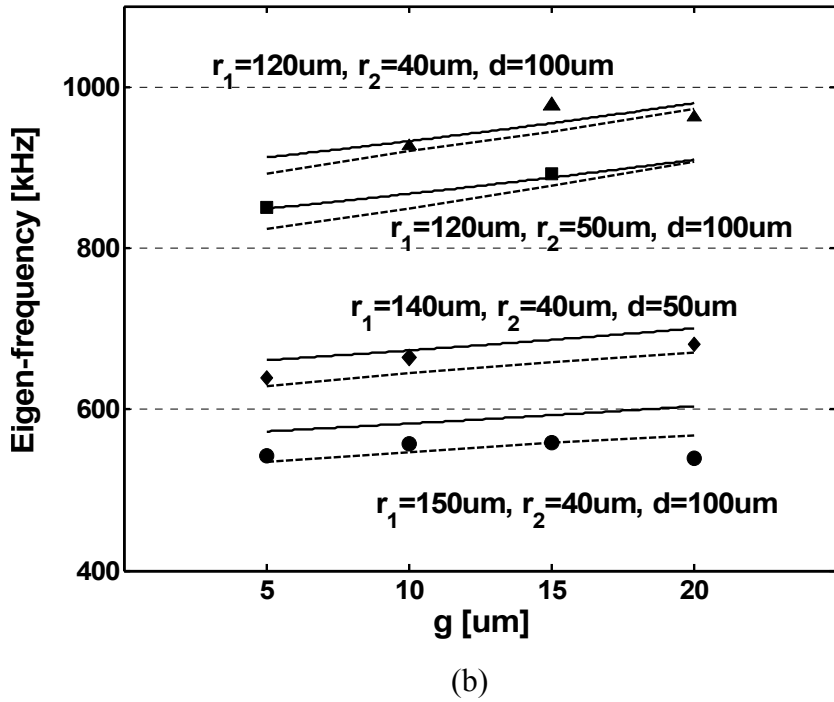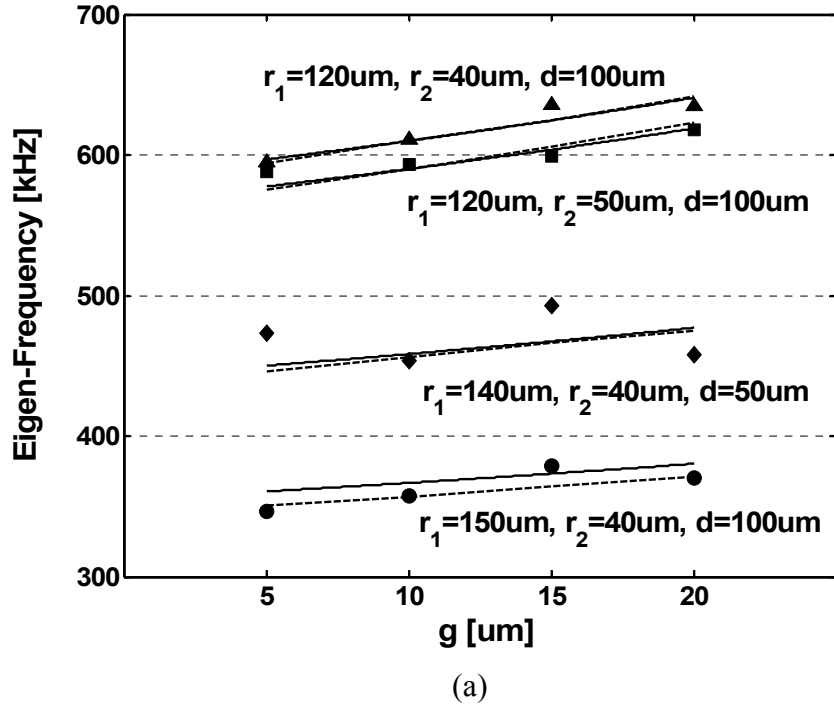
Figure 5.3: (a) In-phase and (b) out-of-phase rotational resonance frequency of disk resonators with different dimensions r_1, r_2, d as a function of the gap size g; solid line: analytical solution, dashed line: FEM simulation results using COMSOL, symbols: experimental data.

5.3.2 Quality Factor

As indicated in Equation (5.27), the Q-factor of a disk resonator is a function of its density and resonance frequency and also depends on the density and viscosity of the surrounding fluid. If the deposited passivation layer is thin compared to the thickness of the silicon resonator, the mechanical properties of single crystalline silicon can be used in Equation (5.26) without causing large errors. However, if the passivation layer thickness becomes comparable to the resonator thickness, the mechanical properties of the used passivation layer should be taken into consideration in the calculation of the effective density and stiffness of the resonator.

Figure 5.4 shows measured Q-factors of various disk resonators in air as a function of the air gap g; the estimated Q-factors from Equation (5.22) to (5.26) are marked with dashed lines. To account for device thickness variations caused by the fabrication process, the estimated Q-factors based on the analytical model are plotted for two device thicknesses. Again, the mechanical properties of (100) single crystalline silicon ($E = 120$ GPa, $\nu = 0.27$, $\rho_{si} = 2330$ kg/m^3) and the properties of an air ($\rho_{air} = 1.2$ kg/m^3, $\eta = 1.82 \ 10^{-5}$ Pa·s) are used in this plot.
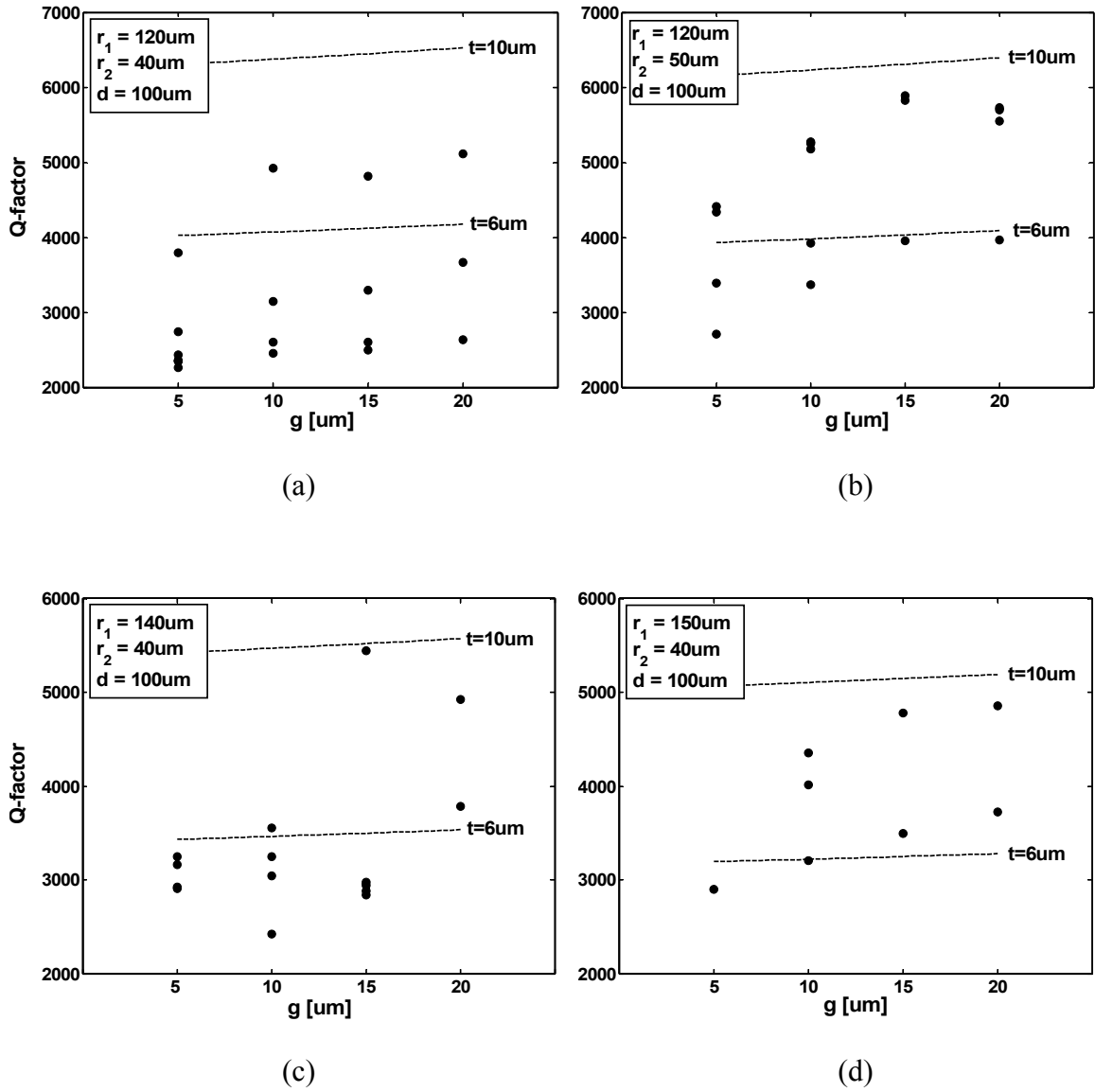
Figure 5.4: Q-factor of in-phase rotational mode as a function of the air gap g for four different resonator geometries (the other dimensions are identical: $w_1 = 35\mu m$, $w_2 = 30\mu m$); the dashed lines represent analytical solutions for two device thicknesses $t = 6$ and 10 μm.

The considerable variations seen in the measured quality factors are likely caused by different device thicknesses and compositions of the passivation layer. Generally, the resonators with 0.1 μm thin PECVD silicon nitride passivation show the highest Q-factors. As the thickness of the passivation layers (consisting of alternating silicon oxide/nitride layers) increases up to 3 μm, a substantial decrease in the Q-factors is observed. The additional passivation layers increase the internal energy losses and decrease the effective resonator density. At the same time, the decrease of the effective mechanical stiffness with increasing passivation layer thickness shifts the resonance frequency to lower values, thus also decreasing the Q-factors of the resonators ($Q \propto \sqrt{\omega}$) due to viscous damping.

Despite of the uncertainties stemming from thickness variations and from the mechanical property changes by additional passivation layers of the fabricated resonators, the calculated Q-factor seems well suited to determine an upper limit for the designed disk resonators.

The influence of passivation layer thickness on the measured Q-factor can be excluded by extracting the Q-factor stemming from viscous damping using Equation (4.1). Figure 5.5 is the plot of the extracted Q-factors (symbols) by viscous damping as a function of the resonance frequency using the data of Figure 4.11. From a least square curve fit (solid line in Figure 5.5), the relation of Q-factor as a function of resonance frequency is extracted, giving $Q = 212\sqrt{f}$ (f in kHz). The simplified analytical expression for the Q-factor in Equation 5.27, yields $Q = 168\sqrt{f} \sim 280\sqrt{f}$ for 6 and 10 μm resonator thicknesses (see dashed lines in Figure 5.5). Considering the device thickness variations originating from fabrication process, the derived analytical model for the Q-factor appears to be sufficient for design optimization of the disk resonators.
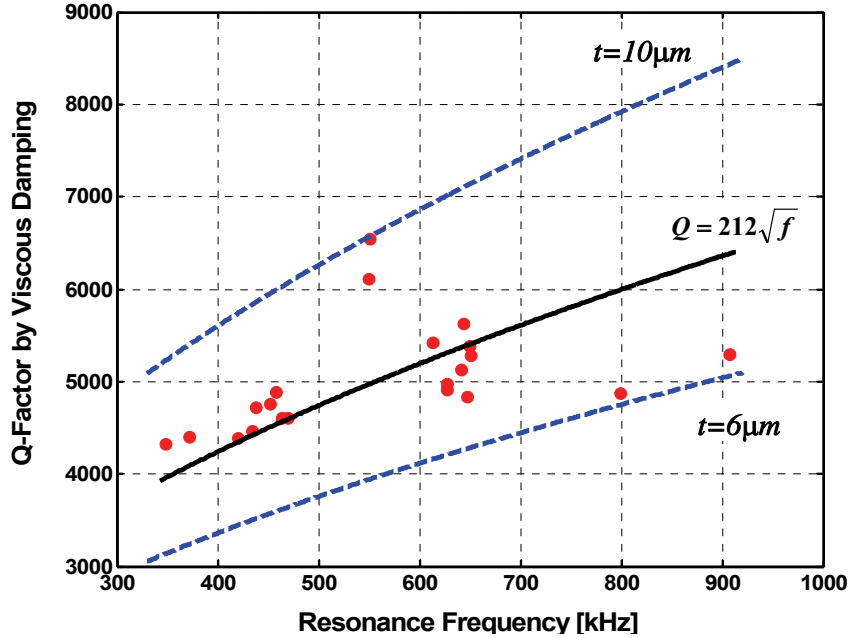
Figure 5.5: Q-factors stemming from viscous damping only as a function of resonance frequency; symbols: experimental data, solid line: curve fit, dashed lines: analytical solutions according to Equation (5.27) at two device thicknesses of 6 and 10 μm.

To compare the Q-factors obtained from the analytical model with the measurement results in liquid environment, experiments have been carried out with disk resonators immersed in water. To this end, DI (de-ionized) water was dropped onto the resonators with a pipette and the open-loop characteristics were recorded (see also Section 4.1.3).

Compared to the measurements in air, the experiment in water are more challenging because of the following two reasons. First, the deposition of thick passivation layers is mandatory for reliable experiments in water. In a first trial, the resonators were coated with a 1 μm parylene layer after wire bonding. Parylene is known to form pin-hole free uniform coatings by a vapor deposition process [86]. However, the 1 μm parylene coating was found just sufficient to protect the aluminum metallization for a short-term measurement in water. Thicker parylene coatings should be used for long-term measurements in water, but they would result in a substantial decrease of the Q-factor as described in Chapter 4.1. To minimize the decrease in Q by the deposited passivation

layers, multiple alternating silicon oxide and silicon nitride films were deposited with a PECVD system. With seven silicon oxide and nitride passivation layers on both sides (top and bottom surface) of the resonators (for a total passivation layer thickness of 3 μm; see Figure 5.6 for details), stable operation of the resonators in water environment was achieved. It should be noted that the optimal thickness and composition of the passivation layer highly depends on the PECVD process recipe and the used deposition equipment.

N	0.3 μm
Ox	0.1 μm
N	0.2 μm
Ox	0.1 μm
N	0.2 μm
Ox	0.1 μm
N	0.2 μm
Ox	0.4 μm

Top Passivation Layer

n-type Si

Bottom Passivation Layer

Ox	0.3 μm
N	0.25 μm
Ox	0.1 μm
N	0.2 μm
Ox	0.1 μm
N	0.2 μm
Ox	0.1 μm
N	0.2 μm

Ox : PECVD Silicon Oxide
N : PECVD Silicon Nitride
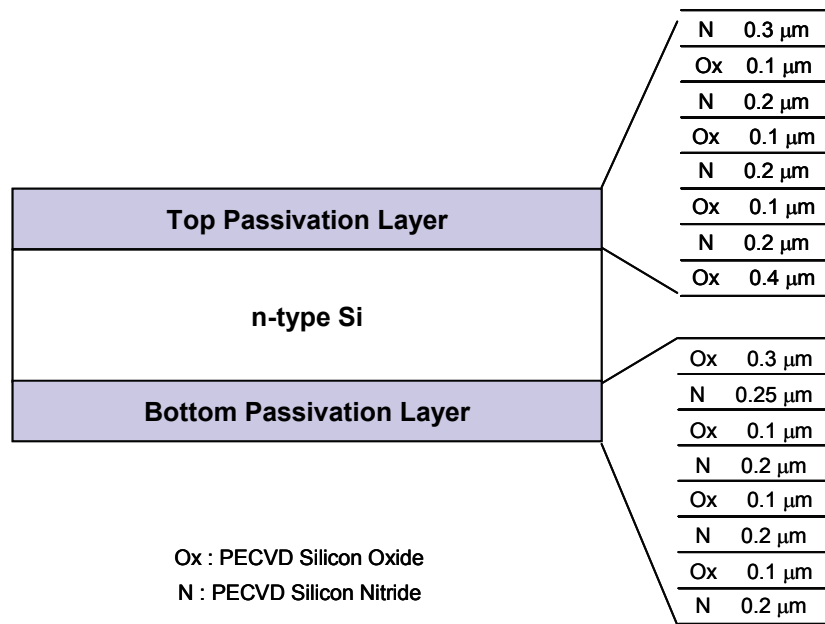
Figure 5.6: Composition of PECVD passivation layers deposited on top and bottom of the disk resonator for stable operation in liquid; the overall PECVD oxide thickness is 1.3 μm, the overall PECVD nitride layer thickness 1.75 μm.

A second challenge of measuring the Q-factor in water is the high dielectric constant of water compared to that of air, resulting in a drastic increase in the electrical coupling between the excitation and detection elements. Combined with the lower signal amplitudes due to the lower Q-factors in liquid, a substantial noise component in the Wheatstone bridge output signal causes variations in the measured Q-factor.

For the analytical estimation of the Q-factors in water, the mechanical properties of the deposited PECVD oxide/nitride passivation layer are taken into consideration to estimate the effective Young's modulus, Poisson's ratio and density of the disk resonators. The mechanical properties used are $E_{si} = 130\,\text{GPa}$, $\nu_{si} = 0.27$, $\rho_{si} = 2330\,\text{kg/m}^3$ for (100) silicon, $E_{ox} = 70\,\text{GPa}$, $\nu_{ox} = 0.165$, $\rho_{ox} = 2200\,\text{kg/m}^3$ for silicon oxide and $E_{ni} = 160\,\text{GPa}$, $\nu_{ni} = 0.253$, $\rho_{ni} = 2500\,\text{kg/m}^3$ for silicon nitride, even though the mechanical properties of PECVD oxide and nitride layers vary widely depending on the gas composition and temperature of the deposition process. The effective mechanical properties of the disk resonators are estimated as:

$$E_{eff} = \frac{E_{si}t_{si} + E_{ox}t_{ox} + E_{ni}t_{ni}}{t_{si} + t_{ox} + t_{ni}} = 127 \sim 128\,[GPa] \tag{5.28}$$

$$\nu_{eff} = \frac{\nu_{si}t_{si} + \nu_{ox}t_{ox} + \nu_{ni}t_{ni}}{t_{si} + t_{ox} + t_{ni}} = 0.252 \sim 0.257 \tag{5.29}$$

$$\rho_{eff} = \frac{\rho_{si}t_{si} + \rho_{ox}t_{ox} + \rho_{ni}t_{ni}}{t_{si} + t_{ox} + t_{ni}} = 2340 \sim 2344\,[kg/m^3] \tag{5.30}$$

The measured Q-factors of disk resonators in water shown in Figure 4.10 are plotted again in Figure 5.7 along with the least square curve fit ($Q = 2.91\sqrt{f}$, f in [kHz]). The measured Q-factors are almost 70% higher than expected from the simplified analytical model of Equation (5.27) ($Q = 1.7\sqrt{f}$, f in [kHz]). For a more accurate comparison of the analytical model with the measured Q-factors, the Q-factor estimated from Equation (5.22) ~ (5.26) is compared with the measured data. Figure 5.8 displays the measured Q-factors in water of disk resonators with two different dimensions along values obtained from the analytical model (solid lines) as a function of the air gap g. The mechanical properties summarized in Equation (5.28) ~ (5.30) and the appropriate water properties ($\rho_{water} = 997\,\text{kg/m}^3$, $\eta = 1.002\,10^{-3}\,\text{Pa·s}$) have been used to calculate the Q from Equation (5.26).
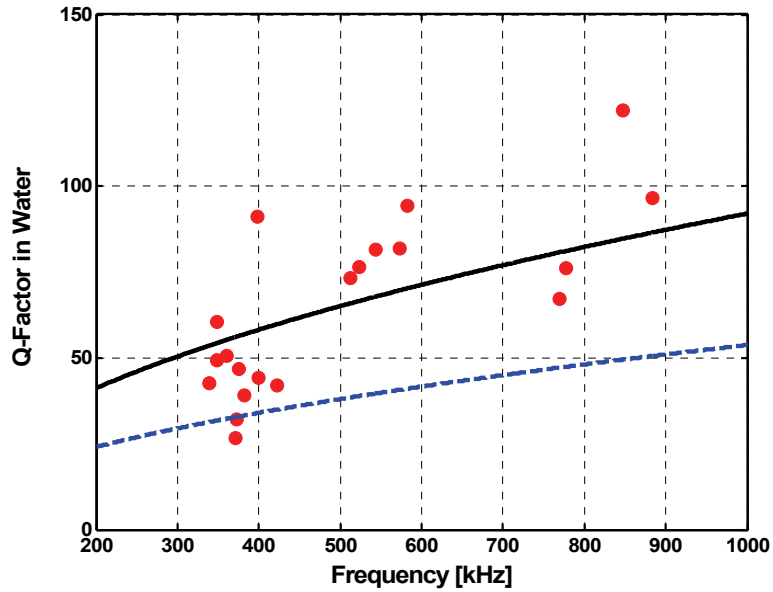
Figure 5.7: Q-factor in water as a function of the resonance frequency of the disk resonators; symbols: experimental data, solid line: curve fit, dashed lines: analytical solution according to Equation (5.27).

(a)

(b)
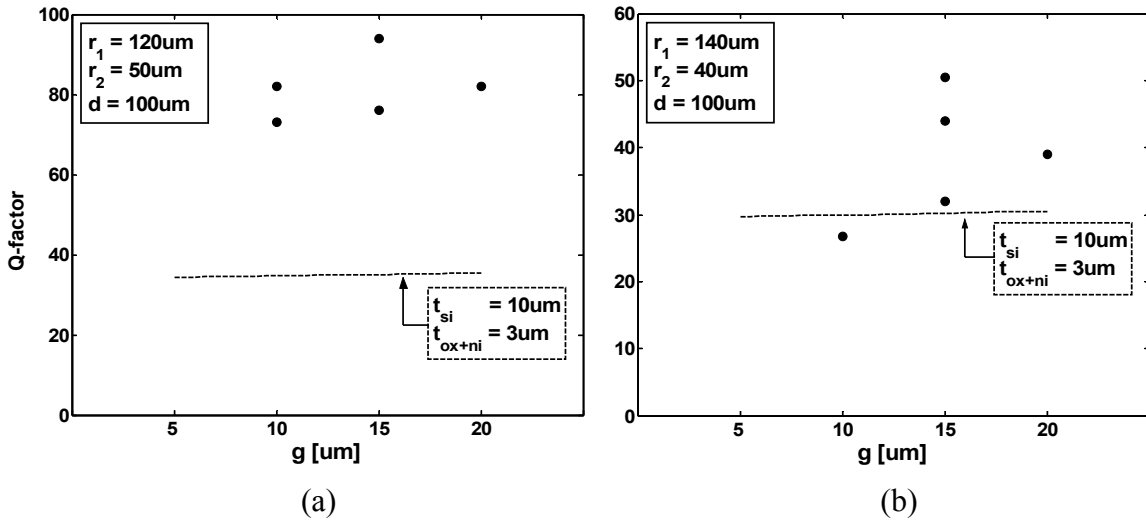
Figure 5.8: Q-factor in water as a function of the air gap g for disk resonators with two different dimensions: (a) $r_1 = 120$ μm, $r_2 = 50$ μm, d = 100 μm, (b) $r_1 = 140$ μm, $r_2 = 40$ μm, d = 100 μm; the symbols represent experimental data, while the solid line corresponds to the analytical results.

As shown in Figure 5.7 and Figure 5.8, the measured Q-factors of the disk resonators are generally larger than those calculated from the analytical model. These –at first sight- unexpected results suggest careful review of the assumptions used in estimating the energy loss by the vibratory motion of the disk resonator. Possible explanations for the discrepancy between analytical calculations and measurement results are discussed below.

It is recognized in the literature that TSM devices do not behave ideally in liquid environment as predicted by the corresponding theoretical equations. Many research results reveal that the viscous damping of the shear mode resonators is highly dependent on the hydrophobicity of the resonator surface and that the bulk liquid properties are not adequate to explain the behavior of TSM devices at high operating frequencies or high fluid viscosities. Resonators with hydrophobic surfaces showed less damping than those with hydrophilic surfaces [87, 88] and a spontaneous formation of a thin gas gap is observed on the resonator surface when a hydrophobic surface is immersed in water [89, 90], which may reduce the viscous damping as well. Moreover, the assumption of non-slip boundary conditions at the resonator surface, i.e. the assumption that the fluid velocity at the solid-liquid interface is same as the vibration velocity of the resonator, has also been questioned by several researchers [90, 91]. They concluded that there exists slip, a discontinuity between the solid and liquid velocities at the interface, if the resonator surface is partially wetted (i.e. hydrophobic surface). The amount of slip depends strongly on the vibration velocity and the onset of slip varies systematically with the contact angle and thus the surface properties [90]. This suggests that the fluid velocity profile derived under non-slip boundary conditions could lead to a higher viscous damping loss than what is observed experimentally. In case of a partially wetted object, the hydrodynamic drag force is reduced substantially with increase of vibration frequency, up to 2-4 orders of magnitude less than that expected from non-slip boundary condition

[90]. Some or all of the above mentioned effects might contribute to the deviations of analytically estimated Q-factors from the measurement results in liquid environment.

5.4 Discussions and Conclusions

A high Q-factor and a good mass sensitivity are the ultimate goals in the design of a resonant mass-sensitive sensor. These two conflicting requirements of a resonant microstructure necessitate innovative design of a resonant microstructure. As an attempt to optimize the structure dimensions of the developed disk resonator, analytical models were developed and compared with experimental results in this chapter, demonstrating the applicability of the derived models to design optimization of the disk resonators.

The analytical expression derived for the Q-factor yields the following design criteria for high Q-factor in-plane rotational mode resonators:

i) maximize the volume to surface ratio of a disk resonator.

ii) increase the rotational moment of inertia $J = r^2 m/2$ at a given resonator mass by increasing the distance from the center of rotation to the point where the effective mass is located.

iii) make the anchor and support beams stiffer to increase the resonance frequency while maintaining the signal output strong enough for detection.

iv) use pin-hole free passivation material without degrading the Q-factor of the resonator.

However, the mass loading effect by the fluid and the squeezed film damping effect at the air gaps should be accounted for in more precise analytical models in the future. Finally, the measured Q-factor of the resonators in water cannot be well described by the developed analytical model, thus necessitating more fundamental research on the viscous damping mechanisms of resonant microstructure, which is beyond the scope of this thesis.

CHAPTER 6

TEMPERATURE COMPENSATION

The resonance frequency of a vibrating microstructure is influenced either by mass or stiffness changes of the mechanical structure itself as mentioned in Chapter 3. Microresonators typically show high mass sensitivities inherited from their small mechanical dimensions, but they respond sensitively to other environmental changes as well. Therefore, for a microresonator to be used as a mass-sensitive biochemical sensor, the mass-sensitivity should be maximized while the frequency drift by other environmental effects must be kept as small as possible. However, as the sensitive layer on top of the microresonator is exposed to the surrounding environment to allow interaction with the target analyte, resonance frequency changes caused by a changing environment are difficult to avoid.

Temperature-induced changes in the elastic modulus of the resonator materials and/or dimensional changes of the resonator structure itself are the most well known causes of a resonance frequency drift of a micro-resonator [92, 93]. Humidity [94, 95], surface oxidation with time [96], ionic reactions on the resonator surface [97], and stress induced by the packaging [93] under varying temperature and/or humidity are other environmental effects which can alter the mechanical stiffness of a resonator and, therefore, its mechanical resonance frequency. Finally, aging caused by mechanical fatigue from long-term operation of the resonator contributes to the mechanical stiffness change as well [98, 99]. Therefore, without compensating for the frequency drift caused by stiffness changes, a high mass resolution cannot be achieved, despite the potential high mass sensitivity of the microresonator.

In this chapter, the concept of a compensation method, which can compensate for the above mentioned frequency drift of a resonator by its mechanical stiffness change, is introduced. By a controlled modulation of the mechanical stiffness of the resonator using an additional feedback loop, the quality factor change by surrounding environmental factors is measured and the resonance frequency drift due to mechanical stiffness changes is compensated.

6.1 Temperature Compensation: State of the Art

The output signal of a microsensor is, in general, not only a function of the measurand of interest, but is also affected by internal/external disturbances, such as aging and environmental changes. Suppression and/or compensation for sensor responses caused by these interfering factors are indispensable in order to achieve high sensor resolution. In case of a mass-sensitive resonant microsensor, changes in the surrounding temperature, humidity, and pressure are, as discussed above, well-known environmental disturbances causing a resonance frequency drift. Arguably, the temperature is the most critical environmental factor, which limits the resolution of a mass-sensitive resonant sensor. Several approaches have been investigated to overcome any temperature-induced frequency drift and are briefly highlighted in the following.

One of the standard approaches is to place a temperature sensor close to the microresonator. Thus, the temperature is measured by means of a temperature sensitive device and a pre-measured dependence of the resonance frequency on the temperature is used for compensation [100]. For accurate temperature compensation, not only a precise temperature measurement but also a reproducible relation between temperature and resonance frequency are required. However, thermal time constants, thermal gradients between resonator and temperature sensor, and temperature sensor instabilities can cause inaccurate temperature measurements, thus leading to insufficient temperature

compensation. Furthermore, any hysteresis in the temperature coefficient of the resonance frequency caused by dynamic temperature variations makes the application of this method challenging [92].

A second widely used approach utilizes an additional resonator as a reference to compensate for the temperature-induced frequency drift of the resonator [101-104]. Sensing and reference resonators, with and without sensitive layer coating, respectively, are operated at the same environmental conditions. The basic idea behind this approach is that any environmental change except a mass changes by analyte absorption will cause the same frequency drift to both the sensing and the reference resonator. Therefore, the frequency change by the added mass can be extracted from the frequency difference between the reference and the sensing resonator. Besides temperature, other environmental factors, such as humidity, density and viscosity changes of the surrounding fluid, can be compensated as well with this method [104]. For precise compensation, sensing and reference resonators must have same mechanical properties or at least show the same relative responses to the changing environmental factors [100]. However, every resonator, even if fabricated on the same chip/wafer, has slightly different mechanical properties and thus slightly different resonance frequencies. In addition, mechanical stress and dimensional changes caused by the swelling of the sensitive layer coating upon exposure to analyte and/or humidity might also affect the frequency difference [95]. Finally, temperature differences between reference and sensing resonator might result from a chemical reaction on the sensitive layer or by thermal gradients between the resonators, thus impeding proper compensation.

Another approach is exploiting two resonance modes of a single resonator for temperature sensing [105, 106]. By exciting the resonator at two different resonance modes with different TCf (Temperature Coefficient of frequency) and by monitoring frequency changes of each vibration mode, the temperature can be extracted and the temperature induced frequency drift can be compensated for. This approach has several

attractive advantages over the method of using an external temperature sensor for compensation. As the resonator itself is used for temperature sensing, there is no need for an external temperature sensor and errors caused by e.g. thermal gradients between temperature sensor and resonator are avoided. Moreover, as the frequency can be measured with high precision, high accuracy temperature sensing and compensation over a wide temperature range are possible with this method. In addition to temperature, other environmental factors are expected to be compensated for as well using multiple vibration modes. However, the excitation and detection elements of the resonator must be designed to sustain stable harmonic oscillation at multiple resonance modes, thus limiting its application to certain resonator structures. So far, this compensation method has been mainly used with quartz resonators and its application to silicon resonator is rarely reported up to now.

6.2 Self Oscillating Feedback Loop

For the application as a mass-sensitive sensor, the microresonator is generally incorporated in an amplifying feedback loop as the frequency-determining element, and the added mass can simply be detected by measuring the resonance frequency change of the resonator using a frequency counter. The principle of an amplifying feedback loop for self-sustaining harmonic oscillations is reviewed here with emphasis on the stability of the harmonic oscillation in a feedback loop.

The force-deflection relation of a mechanical resonator, modeled as a simple harmonic oscillator consisting of mass, damper and spring, can be described by the following differential equation:

$$m\ddot{x} + b\dot{x} + kx = F_m \tag{6.1}$$

where m, b, k, x, and F_m are the effective mass, damping coefficient, mechanical spring constant, deflection and excitation force, respectively. When the excitation force F_m is phase matched with the vibration velocity using the feedback loop, i.e., $F_m = b_0 \dot{x}$, Eq. (6.1) can be expressed as

$$m\ddot{x} + \left(b - b_0\right)\dot{x} + kx = 0 \tag{6.2}$$

and, thus, the effective damping coefficient of the resonator is reduced from b to $(b-b_0)$ by the feedback loop. If the damping force $b\dot{x}$ in Eq. (6.2) is completely compensated by the excitation force $F_m = b_0 \dot{x}$, the effective damping coefficient of the closed loop system is zero and a self-sustaining oscillation can be initiated. Under weak or practically zero damping, the resonance frequency of a resonator is determined by

$$f_0 = \frac{1}{2\pi}\sqrt{\frac{k}{m}} \tag{6.3}$$

6.2.1 Stability of a Feedback Loop

The stability of the resonator oscillation is one of the most important factors in designing a self-oscillating feedback loop. Using Eq. (6.1) ~ (6.3), the stability of the harmonic oscillation of a microresonator embedded in a feedback loop is discussed below under the assumption that the resonator shows a linear response around its resonance frequency. Fig. 6.1 shows the feedback loop consisting of a phase shifter and a linear amplifier. If the chosen amplifier is a fully linear element without saturation, stable harmonic oscillation cannot be maintained.
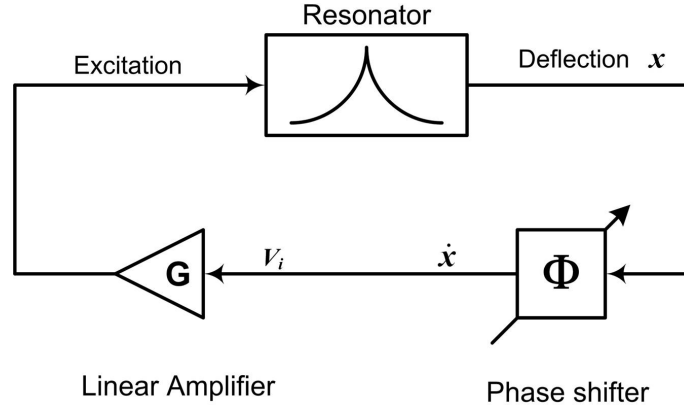
Fig. 6.1: Schematic of a self-oscillating feedback loop with linear amplifier.

Let the feedback amplifier gain G and phase shifter in Fig. 6.1 be adjusted in such a way that harmonic oscillation can be sustained by the feedback loop, i.e. the force generated by the feedback loop $F_m = b_0 \dot{x}$ equals the damping force $b\dot{x}$ of the resonator. Moreover, let us assume that the microresonator is under harmonic oscillation initially and a slight disturbance or noise is given so that the input of the feedback amplifier (V_i in Fig. 6.1) is increased slightly, i.e. from $\dot{x}$ to $\dot{x} + \varepsilon$. Then the generated excitation force $F_m = b_0(\dot{x} + \varepsilon)$ becomes larger than the damping force $b\dot{x}$, thus resulting in a negative effective damping coefficient in Eq. (6.2). Therefore, energy is supplied to the mechanical system and the deflection x of the resonator will be increased, making the excitation force F_m even larger in proportion to the resonator deflection x and so on. On the contrary, if a slight disturbance causes the input signal of the amplifier to decrease slightly, i.e. from $\dot{x}$ to $\dot{x} - \varepsilon$, then the generated excitation force F_m will decrease, resulting in a positive effective damping coefficient. As a result, the stored energy in the mechanical system is reduced and, therefore, the resonator deflection is reduced. This will in turn reduce the excitation force further until the oscillation disappears. Therefore, stable oscillation cannot be sustained using an ideal linear amplifier in the feedback loop.

This instability can be easily avoided by introducing an amplitude-dependent nonlinearity to the amplifier of the feedback loop. One possible way of stabilizing the feedback loop is shown in Fig. 6.2, where linear amplifier is replaced by a voltage limiting comparator.
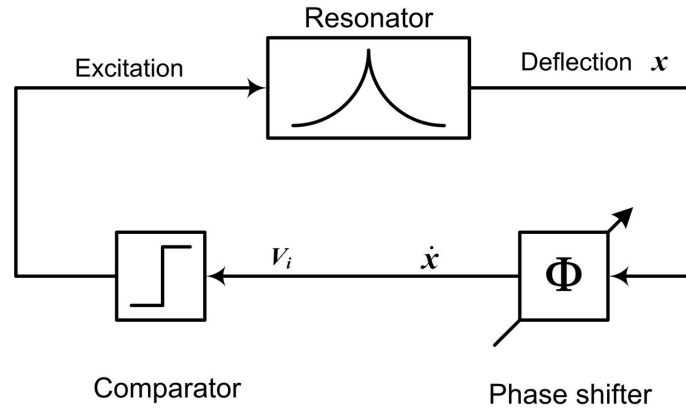
Fig. 6.2: Schematic of a non-linear feedback loop using a comparator.

For the sinusoidal input signal V_i in Fig. 6.2, the comparator generates a square wave signal, which is in phase with the input signal. In other words, phase or frequency information of the input signal are extracted, while the amplitude information is lost by the comparator. The describing function N of a comparator, defined as the complex ratio of the fundamental harmonic component of the output signal V_o to the input sinusoidal signal V_i [107], is given by

$$N = \frac{V_o}{V_i} = \frac{4M}{\pi X} \angle 0^\circ \tag{6.4}$$

X and M in Eq. (6.4) are the amplitudes of the input sinusoidal signal and of the square wave output signal, respectively. The system equation of Fig. 6.2 can be rewitten using the describing function of a comparator as

$$m\ddot{x} + b\dot{x} + kx = \frac{4M}{\pi} \frac{\dot{x}}{|\dot{x}|} \qquad (6.5)$$

$$m\ddot{x} + \gamma\dot{x} + kx = 0, \quad \gamma = \left(b - \frac{4M}{\pi|\dot{x}|}\right) \qquad (6.6)$$

As can be seen from the above equations, the excitation force generated by the feedback loop in Fig. 6.2 becomes constant and is no longer affected by variations of the input signal amplitude.

The stability of a harmonic oscillation with this nonlinear feedback loop can be verified in the same way as discussed above. If the resonator deflection x and therefore $\dot{x} = j\omega x$ is increased by an external disturbances or noise, then the damping force $b\dot{x}$ becomes larger than the constant excitation force F_m as shown in Fig. 6.3, resulting in a positive damping coefficient (operating point A). Therefore, the deflection of the oscillation is decreased back to the original stable operating point C. On the contrary, a decrease in the resonator deflection by a disturbance generates a negative damping in Eq. (6.6), thus energy is supplied to the resonator (operating point B) and the resonator deflection increases back to the steady state value. Therefore, stable harmonic oscillation can be sustained with this feedback loop.
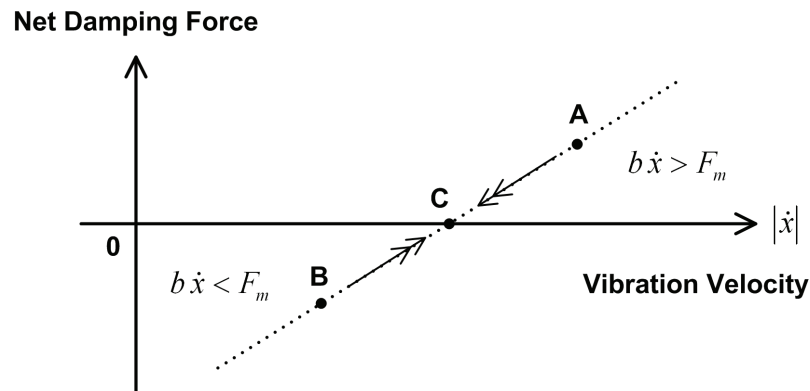
Fig. 6.3: Net damping force of a resonator with stabilized feedback loop operated at point C subject to disturbances in the velocity (or deflection) amplitude.

The resonator response in a feedback loop is now considered when it is subjected to phase/frequency fluctuations. Let us assume that the initial operating point of the resonator is set exactly at the mechanical resonance frequency f_0 by the feedback loop. Then, the deflection signal of the resonator will show a $-\pi/2$ phase delay at f_0 with respect to the applied force as shown in Fig. 6.4.
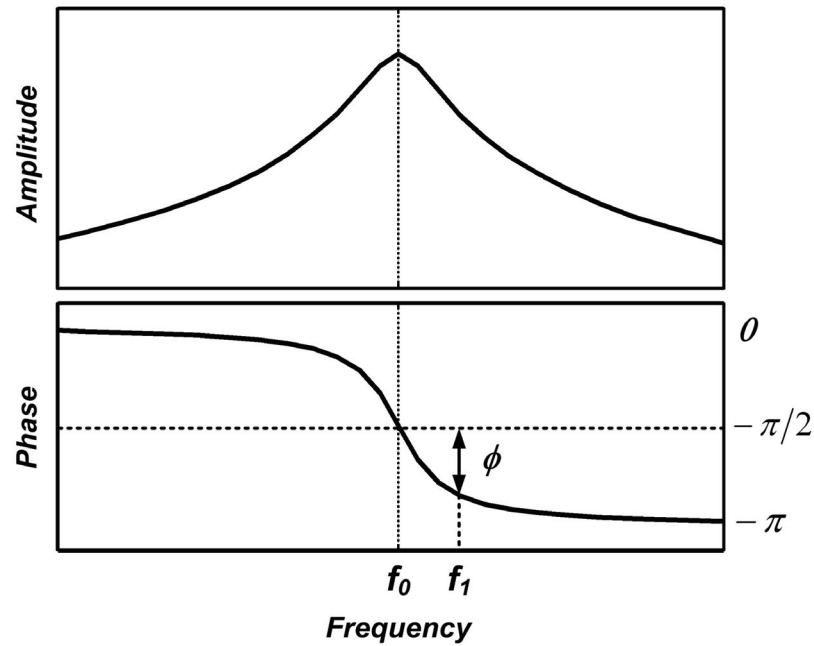
Fig. 6.4: Amplitude and phase response of a resonator around its resonance frequency.

Now, we consider the case that a disturbance with frequency f_1 higher than f_0 is injected to the excitation signal. When this disturbance passes through the resonator, the phase delay by this disturbance becomes larger than $-\pi/2$, i.e. $-\pi/2 - \phi$. This situation can be described by the following equation.

$$m\ddot{x} + b\dot{x} + kx = \frac{4M}{\pi} \frac{\dot{x}}{|\dot{x}|} e^{-j\phi} \tag{6.7}$$

Using the relation of $\dot{x} = j\omega x$, Eq. (6.7) can be expressed as:

$$m\ddot{x} + \left(b - \frac{4M}{\pi}\frac{cos\,\phi}{|\dot{x}|}\right)\dot{x} + \left(k - \frac{4M}{\pi}\frac{sin\,\phi}{|x|}\right)x = 0 \qquad (6.8)$$

Eq. (6.8) indicates that the resonator responds to the disturbance as if it would have a higher effective damping coefficient and a reduced effective stiffness, because of larger phase delay (ϕ in Fig. 6.4) at frequency f_1. Therefore, a disturbance with frequency higher than f_0 is attenuated (higher damping) and decelerated (reduced stiffness) to a lower frequency. On the contrary, disturbances with frequencies lower than f_0 will be accelerated to a higher frequency and their magnitude will again be damped. As a result, stable harmonic oscillation at the resonance frequency of the resonator will be maintained irrespective of the phase noise introduced to the feedback loop.

6.3 Principle of Temperature Compensation

6.3.1 Stiffness Modulation

The effective spring constant of a resonant microstructure can be altered by applying an additional force. If the additional excitation force F_C is in phase with the deflection x of the oscillating resonator, i.e. $F_c = Cx$ and added to Eq. (6.1), then the system equation of Eq. (6.2) is modified as

$$m\ddot{x} + (b - b_0)\dot{x} + (k - C)x = 0 \qquad (6.9)$$

where C is the artificial spring constant generated by additional spring force $F_c = Cx$.

Therefore, the effective stiffness of the resonator is modulated by the additional spring force F_C. Depending on the direction of the applied force F_C with respect to the deflection of the resonator under harmonic oscillation, the effective stiffness of the resonator can be either reduced or increased. As a result, the resonance frequency of the harmonic oscillator is changed in response to the modulated effective stiffness:

$$f_0 = \frac{1}{2\pi}\sqrt{\frac{k-C}{m}} \qquad (6.10)$$

This concept has been utilized for resonant magnetic field sensors where the stiffness modifying force is generated either passively using a permanent magnet [108] or actively using a Lorentz force induced by an ac current in the presence of a (static) magnetic field [109]. The spring constant of the resonator is modified in response to the magnetic field and, thus, the magnetic field can be detected by measuring the resonance frequency change of the resonator. In these cases, the amplitude of the magnetically induced force, which is proportional to the measurand (magnetic field), is detected, even though it is read out via a frequency change.

On the other hand, if the additional force F_c is generated utilizing a signal of an amplifying feedback-loop itself by proper electronic circuitry, the stiffness of the resonator can be modulated by a controlled amount. This fact can be exploited to estimate the stiffness change of a microresonator by environmental factors, and thus to compensate for its resulting frequency drift.

6.3.2 Estimation of Relative Stiffness Change

The schematic diagram of the circuit used to estimate the relative stiffness change of a resonator by a controlled stiffness modulation is shown in Fig. 6.5. A conventional feedback loop (hereafter main loop) is combined with an additional feedback loop (hereafter compensation loop) to modulate the effective stiffness of the resonator. The main loop consists of a phase shifter and a non-linear amplifier. The phase shifter adjusts the electrical signal to have the same phase as the mechanical vibration velocity of the resonator. An automatic gain controller (AGC) or a simple comparator can be used to stabilize the harmonic oscillation of the resonator. The compensation loop consists of a phase shifter, an amplifier, a switch and an adder. The phase shifter of the compensation loop introduces an additional 90° phase delay compared to the main loop signal, thus

generating a signal that is in-phase with the resonator deflection. The linear amplifier gain G sets the magnitude of the additional spring force. Finally, the signal coming from the compensation loop is added to the main-loop signal through a single-pole double-throw switch as illustrated in Fig. 6.5.
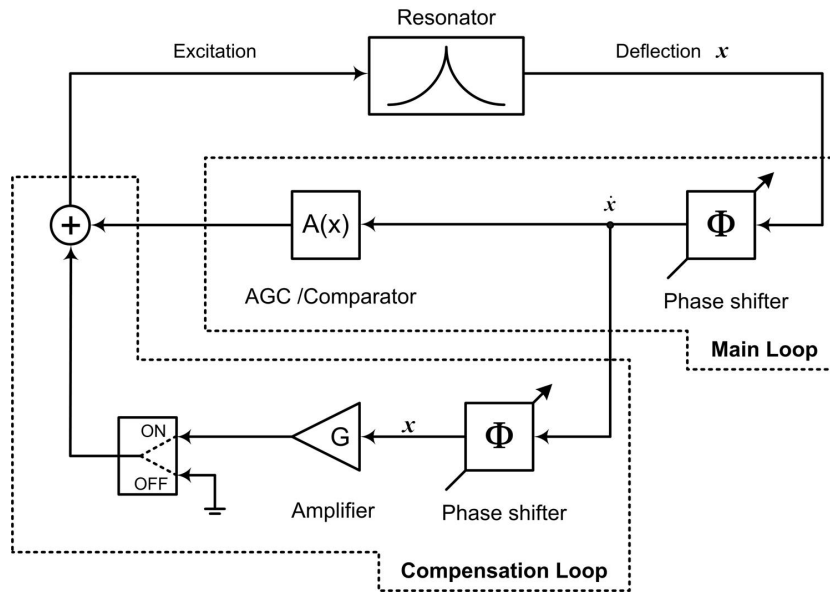
Fig. 6.5: Schematic diagram showing the concept of the compensation method based on the controlled stiffness modulation.

The behavior of the resonator in this closed loop system can be described by the following differential equation:

$$m\ddot{x} + b\dot{x} + kx = \chi\gamma\left(H\dot{x} + Gx\right) \qquad (6.11)$$

where χ, γ, H, and G are the transfer function of the generated mechanical force to an applied electrical excitation signal, the transfer function of the electrical read-out signal to the resonator deflection, and the transfer functions of the main and the compensation loop in Fig. 6.5, respectively.

Under the assumption that the force generated by the compensation loop is equivalent to a spring constant C, i.e. $C = \chi \gamma G$, the modulated resonance frequency ω_0 of a resonator by the compensation loop will be determined from Eq. (6.9) as

$$\omega_0 = \sqrt{\frac{k \pm C}{m}} \qquad (6.12)$$

As the effective spring constant of the resonator can be increased or decreased by the same amount depending on the polarity of the compensation loop gain G, the $\pm$ sign is introduced in Eq. (6.12). Then, the measured resonance frequencies with compensation loop OFF and ON, respectively, become:

$$\omega_{OFF} = \sqrt{\frac{k}{m}}, \quad \omega_{ON} = \sqrt{\frac{k \pm C}{m}} \qquad (6.13)$$

We now assume that the resonance frequency of the resonator changes with time, i.e., the spring constant k and the mass m of the resonator change over time (from t_1 to t_2) from m_1, k_1 to m_2, k_2, respectively, as shown in Fig. 6.6.
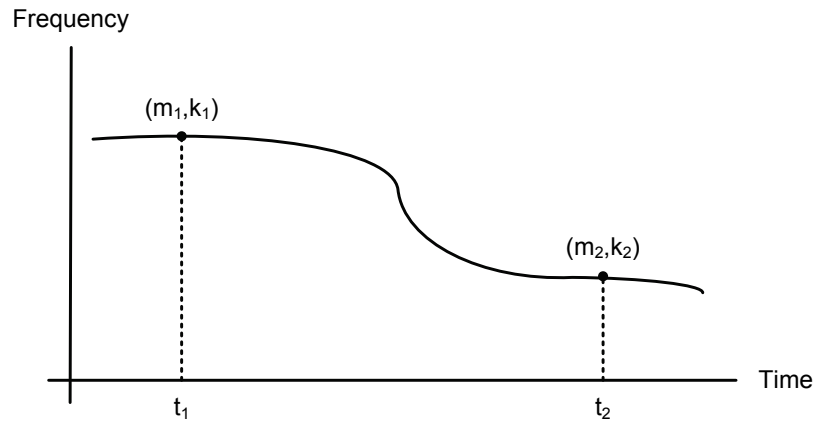
Fig. 6.6: Resonance frequency drift with time induced by mass and stiffness changes of a resonator.

The relative spring constant change can be extracted by periodically enabling and disabling the compensation loop as follows. From the measured resonance frequency ratios of ω_{ON}/ω_{OFF} with and without compensation loop at time t_1 and t_2, following equations are derived.

$$\left(\frac{\omega_{ON}}{\omega_{OFF}}\right)^2\bigg|_{t=t1} = \frac{k_1 \pm C}{k_1} = \alpha \qquad \left(\frac{\omega_{ON}}{\omega_{OFF}}\right)^2\bigg|_{t=t2} = \frac{k_2 \pm C}{k_2} = \beta \qquad (6.14)$$

Then, the relative spring constant change dk/k is derived from Eq. (6.14) as:

$$\frac{dk}{k} = \frac{k_2 - k_1}{k_1} = \frac{\alpha - \beta}{\beta - 1} \qquad (6.15)$$

Once the relative stiffness change of the resonator is extracted from Eq. (6.14) and (6.15), the resonance frequency drift caused by the stiffness variation can be subtracted from the measured frequency change:

$$\frac{d\omega}{\omega_0} = \frac{1}{2}\left(\frac{dk}{k} - \frac{dm}{m}\right) \qquad (6.16)$$

The compensated frequency ω_{comp}, representing the frequency change solely by a mass change of the resonator, is estimated from the measured resonance frequency ω_m as

$$\omega_{comp} = \omega_m\left[1 - \frac{1}{2}\frac{dk}{k}\right] \qquad (6.17)$$

However, to precisely estimate the relative stiffness change using the schematic shown in Fig. 6.5, $C = \chi\gamma G$ in Eq. (6.11) should be maintained constant during operation. In other words, the excitation and read-out elements of the resonator should be insensitive to temperature. A constant amplifier gain G, a noise-free read-out signal from the detection elements, and proper high frequency stability of the resonator are other requirements for the successful temperature compensation with the schematic shown in Fig. 6.5.

6.3.3 Estimation of Relative Quality-Factor Change

The temperature compensation method in the previous section has several critical requirements as mentioned before. Instead of a direct assessment of the relative stiffness change using the feedback system in Fig. 6.5, the relative quality factor change is considered here to compensate for the temperature influence on the resonance frequency.

The quality factor has been shown to be a good temperature sensor and its use for compensating temperature-induced frequency drift of a resonator has been already reported [110]. In this work, the quality factor of the resonator was estimated by measuring the amplitude of the resonator output signal [110]. However, a precise measurement of the resonator amplitude requires a carefully designed circuitry with high signal to noise ratio, and an analog-to-digital converter is needed for compensating the temperature-induced frequency drift of the resonator.

In this section, a feedback system, which can extract the Q-factor of a resonator by measuring its resonance frequency is introduced. Fig. 6.7 shows the schematic diagram of the feedback loop for Q-factor estimation; compared to the compensation loop of Fig. 6.5, the linear amplifier is replaced by a comparator.

The motion of the resonator in this feedback loop can be described by

$$m\ddot{x} + b\dot{x} + kx = \psi_D \frac{\dot{x}}{|\dot{x}|} + \psi_C \frac{x}{|x|}$$

$$\psi_D = \chi\gamma \frac{4M_d}{\pi}, \quad \psi_C = \chi\gamma \frac{4M_c}{\pi}$$

(6.18)

where M_d and M_c are the amplitudes of the square-wave signals generated in the main and compensation loop, respectively. Eq. (6.18) can be rearranged to Eq. (6.19) to extraxt the vibration amplitude of the resonator.

$$m\ddot{x} + \left(b - \frac{\psi_D}{|\dot{x}|} \right)\dot{x} + \left(k - \frac{\psi_C}{|x|} \right)x = 0$$

(6.19)
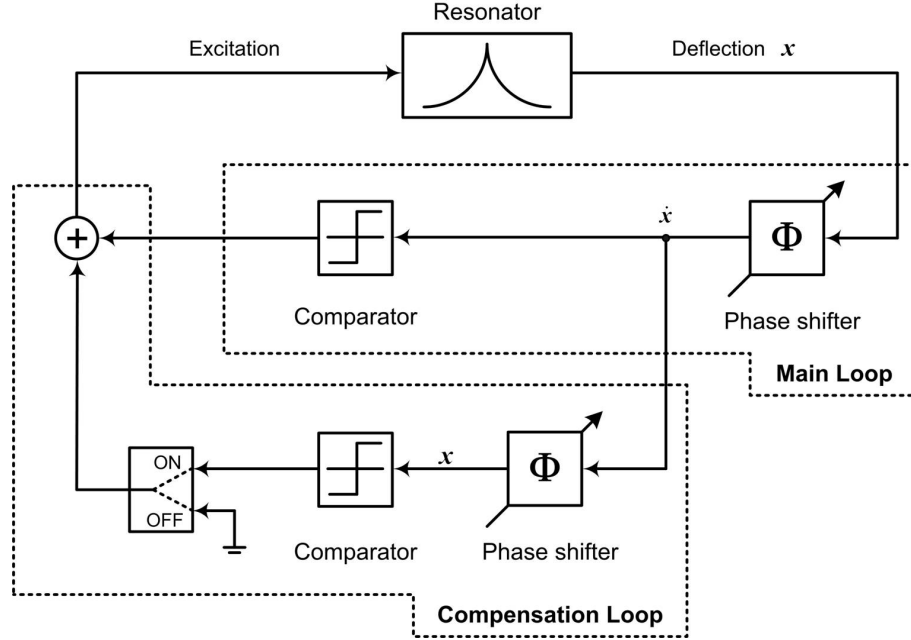
Fig. 6.7: Schematic diagram of feedback loop system to extract the relative Q-factor change of a resonator.

The magnitude of the steady state vibration velocity $\dot{x}$ and vibration amplitude x of the resonator embedded in the feedback circuit are obtained from Eq. (6.19) by forcing the effective damping force (second term in Eq. (6.19)) to zero:

$$|\dot{x}| = \frac{\psi_D}{b}, \quad |x| = \frac{\psi_D}{b\omega_0} \tag{6.20}$$

Then, the differential equation of Eq. (6.19) can be expressed in terms of the Q-factor of the resonator using Eq. (6.20) as:

$$m\ddot{x} + \left(k - \frac{\psi_C}{\psi_D}b\omega_0\right)x = 0 \quad \Leftrightarrow \quad m\ddot{x} + k\left(1 - \frac{\psi_C}{\psi_D}\frac{1}{Q_0}\right)x = 0$$
$$Q_0 = \frac{k}{b\omega_0} \tag{6.21}$$

Eq. (6.21) reveals the interesting fact that the relative stiffness change induced by the feedback loop shown in Fig.6.7 is directly related to the Q-factor of the resonator. Moreover, it does not depend on the absolute magnitude of the additional spring force,

but is proportional to the ratio of the two forces generated by the main loop and the compensation loop.

If the forces generated by the main and the compensation loop are equal, i.e. $\Psi_D = \Psi_C$, Eq. (6.21) is simplified to Eq. (6.22) and the frequency ratios of the resonance frequencies with enabled and disabled compensation loop are determined by Eq. (6.23) at times t_1 and t_2.

$$m\ddot{x} + k\left(1 - \frac{1}{Q_0}\right)x = 0 \tag{6.22}$$

$$\left(\frac{\omega_{ON}}{\omega_{OFF}}\right)^2\Bigg|_{t=t1} = \frac{Q_1 - 1}{Q_1} = \alpha \qquad \left(\frac{\omega_{ON}}{\omega_{OFF}}\right)^2\Bigg|_{t=t2} = \frac{Q_2 - 1}{Q_2} = \beta \tag{6.23}$$

Using Eq. (6.23), a direct measurement of the Q-factor is possible and the relative Q-factor change with time can be derived the same way as in Eq. (6.15).

$$\frac{\Delta Q}{Q} = \frac{Q_2 - Q_1}{Q_1} = \frac{\alpha - \beta}{\beta - 1} \tag{6.24}$$

Once the relative Q-factor change is extracted from Eq. (6.24), then the temperature-induced frequency change of the resonator can be compensated for, if the temperature dependence of the Q-factor is known from a calibration step. Even though this approach requires a pre-calibration step for temperature compensation, it has several advantages over the direct stiffness measurement using the feedback system in Fig. 6.5. These advantages include:

1. The precision of the extracted relative Q-factor change is not affected by temperature dependences of the excitation and detection elements of the resonator.

2. The feedback system is more robust to noise in the output signal of the resonator.

3. The amplitude of the square wave signal of the compensation loop is easier kept constant than the gain of a linear amplifier; moreover, only the ratio of the

comparator output of the main and the compensation loop are to be kept constant.

4. Besides the relative Q-factor change, a direct Q-factor estimation is possible.

5. The Q-factor estimation is done quasi-digitally by means of a frequency measurement.

If the relative damping coefficient change (in addition to the Q-factor change) can be extracted from Eq. (6.20) by means of an amplitude measurement, the required calibration step can be potentially avoided and the relative change of all system constants, i.e. *m*, *k*, and *b*, of the resonator can be extracted.

6.4 Experimental Results

The concept of the temperature compensation method introduced in this chapter is experimentally verified in this section. Disk resonators with on-chip electrothermal excitation and piezoresistive detection elements are used in this experiment. A direct estimation of the stiffness change using the schematic shown in Fig. 6.5 is challenging with the chosen disk resonators, because of the temperature dependence of the resistors used as excitation and detection elements. Therefore, the temperature compensation method based on the estimation of the relative quality factor change using the circuit shown in Fig. 6.7 is mainly tested in this section.

6.4.1 Feedback Circuit and Signal Conditioning

The detailed schematic diagram of the implemented feedback circuitry is shown in Fig. 6.8. In the main loop, the piezoresistive output signal from the resonator is first amplified with an operational amplifier and this signal is fed to a phase adjusting circuit (all-pass filter) to generate a signal that has the same phase as the vibration velocity of the resonator, which is 90° phase leading compared to the deflection signal.
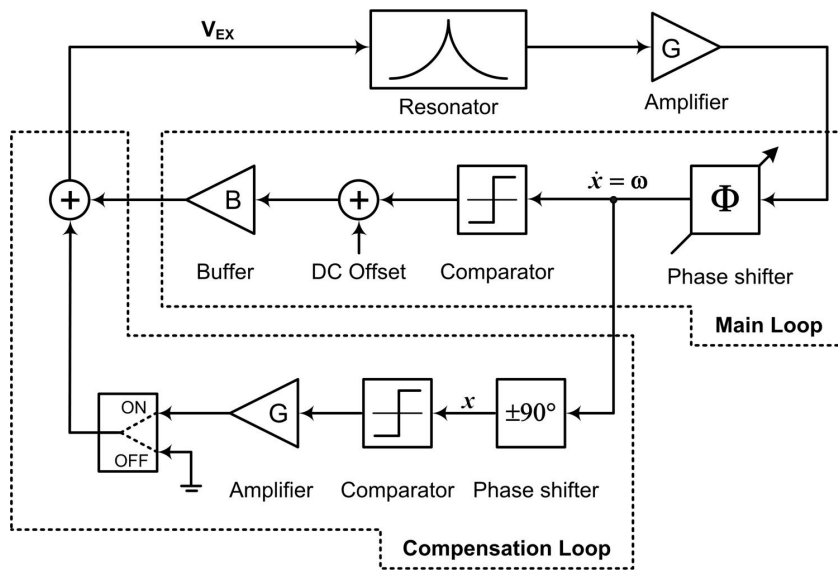
Fig. 6.8: Schematic diagram of the implemented feedback circuitry for temperature compensation.

It should be noted that the electrical output signal of the resonator is generally not in phase with the resonator deflection because of the parasitic electrical coupling between excitation and detection signal (see Section 4.3). Therefore, the signal coming from the resonator is first phase tuned to make it phase matched with the vibration velocity by adjusting the phase shifter until the signal from the resonator reaches its maximum amplitude. The phase-tuned signal is then applied to a Schmitt-trigger circuit which limits the signal amplitude. Thereafter, a DC bias voltage is added to the square wave signal to ensure that the thermally generated force has a component with the same frequency as the Schmitt trigger output signal. The resulting excitation signal is fed back to the resonator, sustaining the harmonic oscillation at the mechanical resonance frequency.

The compensation loop consists of a phase shifter, a Schmitt trigger, an adder and a switch. The phase shifter generates a signal that is in phase with the resonator deflection, which is 90° phase-delayed compared to the phase shifter output signal of the

main loop. The Schmitt trigger limits the signal amplitude to a predefined value and the switch is used to enable or disable the compensation loop.

The increased static power dissipation inside the resonator by the enabled compensation loop can cause a temperature elevation, resulting in a negative resonance frequency change due to the temperature-induced material softening. To keep the static power dissipation of the resonator constant regardless of the switch position, the excitation signal V_{EX} in Fig. 6.8 is adjusted using the operational amplifier circuit shown in Fig. 6.9.
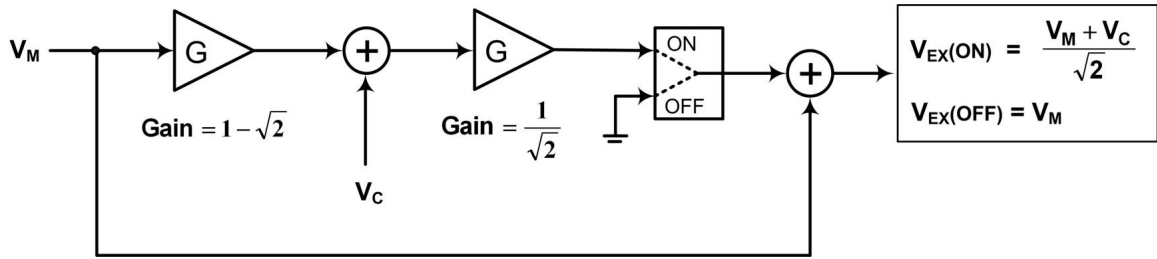
Fig. 6.9: Schematic of electronic circuitry to maintain constant static power dissipation in the resonator excitation elements.

Thus, the excitation voltage V_{EX} depends on the switch position as

$$|V_M| = |V_C|$$

$$V_{EX(ON)} = \frac{V_M}{\sqrt{2}} + \frac{V_C}{\sqrt{2}}$$ (6.25)

$$V_{EX(OFF)} = V_M$$

where V_M, V_C, $V_{EX(ON)}$, and $V_{EX(OFF)}$ are the signal amplitude from the main loop, the signal amplitude from the compensation loop, and the excitation signals when the switch is ON and OFF, respectively.

6.4.2 Measurement Setup and Results

Experiments have been carried out with the test setup shown in Fig. 6.10. The closed loop system of Fig. 6.8 is implemented with a printed circuit board and the detailed circuit is presented in Appendix A.
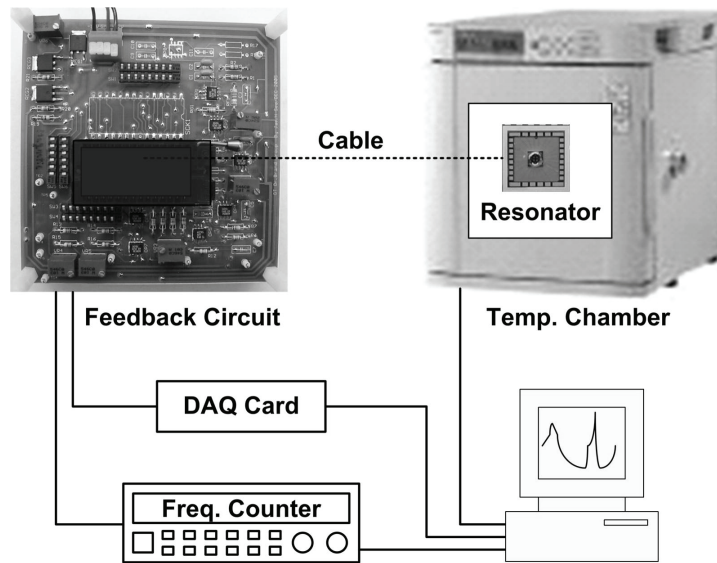
Fig. 6.10: Schematic diagram of the test setup.

The resonator is placed inside an ESPEC SH-241 environmental test chamber and connected through a cable to the printed circuit board located outside of the chamber to avoid temperature effects in the feedback circuitry. A Labview program controls the switch position via a National Instrument DAQ card and records the frequency of the resonator and the temperature of the chamber. To find the relation between the estimated quality-factor change and the measured resonance frequency change for a given resonator, an initial calibration step is carried out under varying temperature. Based on the measured data, a constant coefficient which relates the relative quality-factor change

to the frequency change is extracted and used for subsequent temperature compensation. The test conditions and the properties of the resonator are summarized in Table 6.1.

Table 6.1: Test conditions and properties of the disk resonator
used for temperature compensation experiments.

Resonator dimensions	$r_1 = 120, r_2 = 50, g = 15$ [μm]
Resistance of Wheatstone bridge	460 [Ω]
Resistance of heating resistors	890 [Ω]
Bias voltage for Wheatstone bridge	1.5 [V_{DC}]
DC offset voltage for excitation	0.75 [V_{DC}]
Amplitude of main-loop square wave	400 [mV]
Amplitude of compensation-loop square wave	400 [mV]

The compensation loop is enabled for 2 seconds every 52 seconds for all the experiments and the resonance frequency of the resonator is recorded every second. The signal amplitudes of the main and the compensation loop are both set to 400 mV by the respective voltage limiters. The resonance frequencies of the chosen resonators around 571 kHz are lowered by approximately 106 Hz at 45°C, when the compensation loop is enabled as shown in Fig. 6.11. For an initial calibration, the disk resonator is operated under varying temperature between 40°C and 50°C. The frequency of the resonator is measured and the relative Q-factor change is extracted using the compensation loop. A resonance frequency drift around 191 Hz is observed due to the 10°C temperature variation as shown in Fig. 6.12. The relative Q-factor change extracted using Eq. (6.24) is plotted in Fig. 6.13 as a function of the temperature and of the relative frequency change of the resonator.

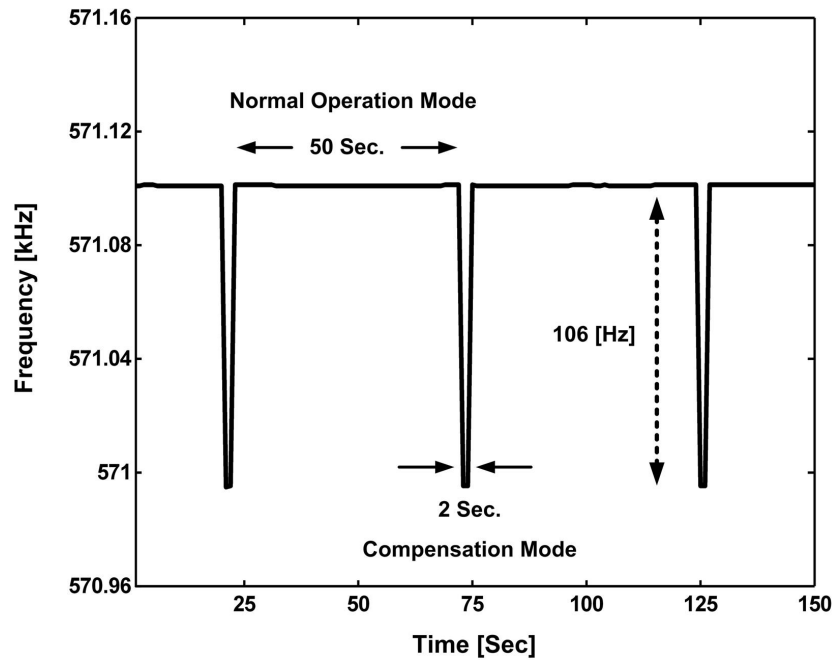Fig. 6.11: Resonance frequency of disk resonator with and without compensation loop.
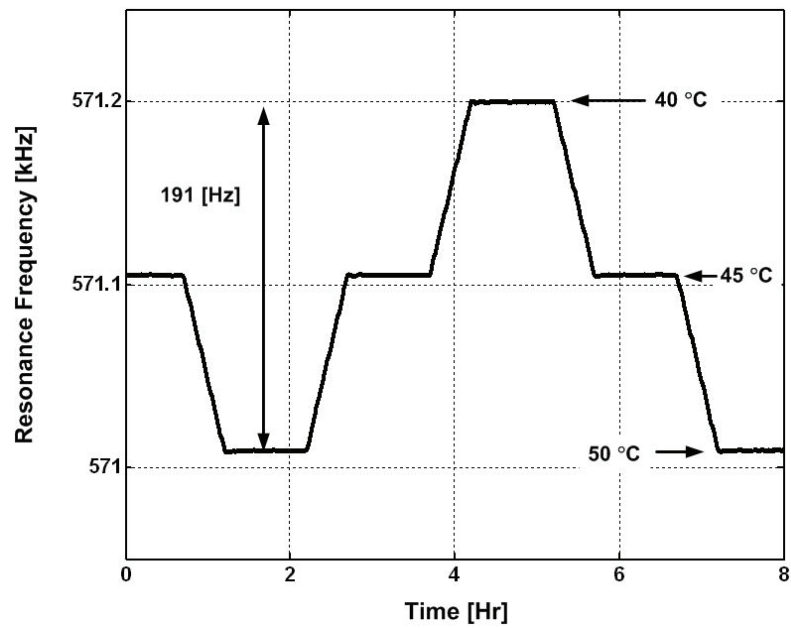
Fig. 6.12: Resonance frequency of resonator when temperature changes from 40~50 °C.
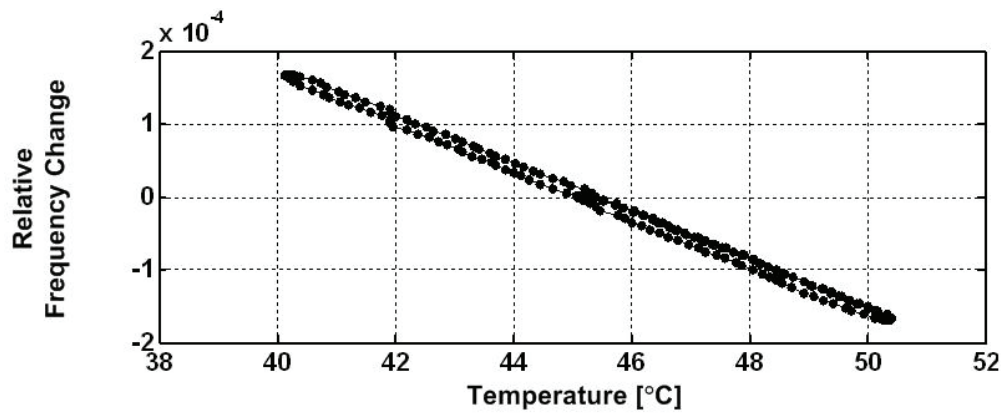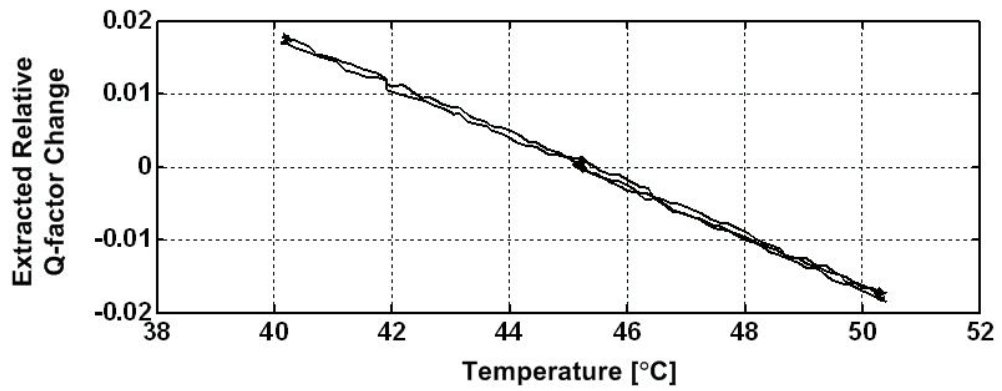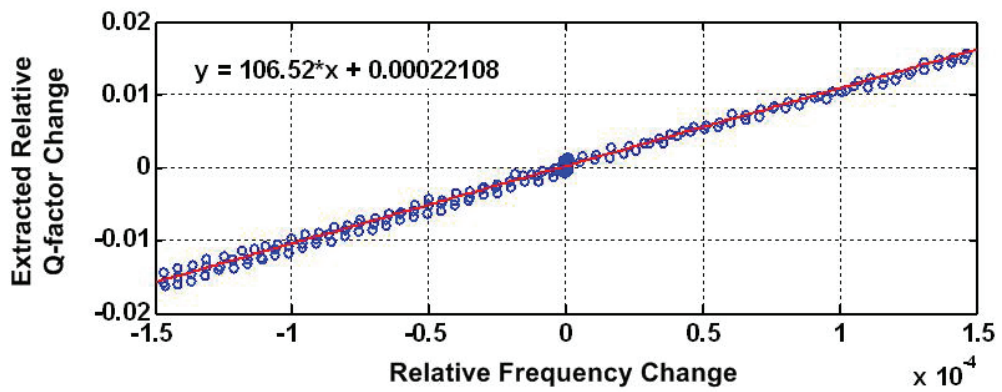
Fig. 6.13: Plot of relative frequency change (a) and extracted relative Q-factor change (b) as a function of temperature, and of relative Q-factor change as a function of relative frequency change (c) for temperatures ranging from 40~50 °C.

129

The relative Q-factor and the relative frequency changes are extracted based on the values at 45°C. The estimated relative Q-factor change and the resonance frequency exhibit a small hysteresis during thermal cycling as can be noted in Fig. 6.13(a) and (b). Changes in thin film stresses during thermal cycling are well known causes of thermal hysteresis in micromachined sensors [111, 112].

For fast calibration and simple temperature compensation without a look-up table, this thermal hysteresis is not considered during subsequent experiments. Instead, the relative Q-factor change and the relative frequency change are assumed to be linearly proportional to each other. From the plot of Fig. 6.13(c), the relation $dQ/Q_0 = 106.5 \times d\omega/\omega_0$ is obtained using a least square curve fit method and the resulting proportionality factor is used to compensate for the temperature induced resonance frequency change of the chosen resonator.

One interesting observation is that the ratio of *relative* Q-factor change to relative frequency change ($dQ/Q_0 = 106.5 \times d\omega/\omega_0$) seems to be related to the *absolute* frequency change (106 Hz in Fig. 6.11) by the enabled compensation loop. Experiments carried out with several other disk resonators showed a similar behavior. However, this observation is not clearly explainable at this point and will be discussed further at the end of this chapter.

Following the initial calibration step, the resonator is operated over a wider temperature range to check the feasibility of the proposed compensation method. Fig. 6.14 highlights the test results when the resonator is subjected to a temperature variation between 30~60°C (see Fig. 6.14a). The relative Q-factor change is extracted from Eq. (6.24) using the Q-factor at 45°C as a base value. The extracted Q-factor change (see Fig. 6.14(b)) follows the temperature change.
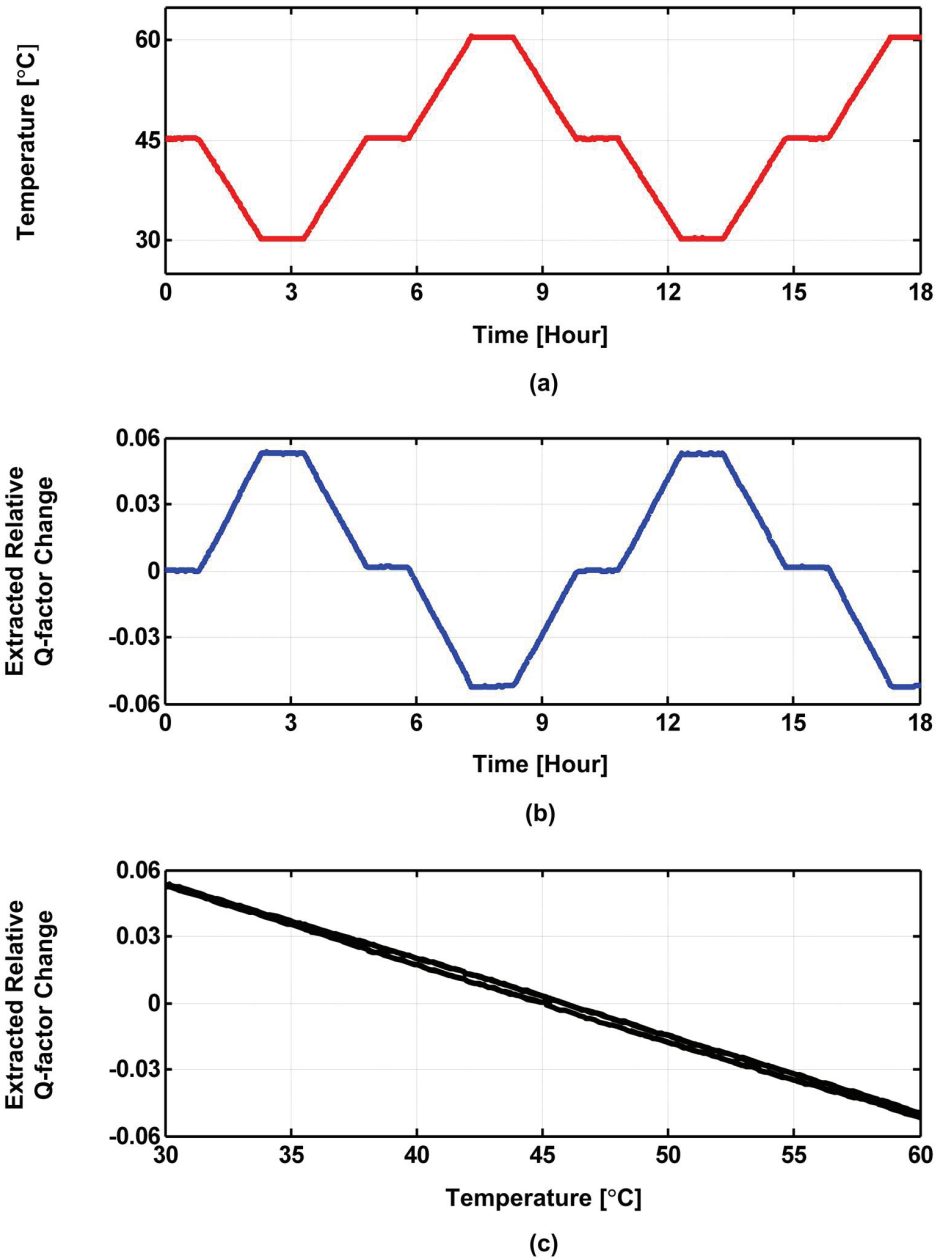
Fig. 6.14: (a) Ambient temperature and (b) extracted relative Q-factor change (from Eq. (6.24)) of a disk resonator subject to a predefined temperature profile; (c) extracted Q-factor change as a function of the ambient temperature.

The temperature compensated resonance frequency change is plotted in Fig. 6.15 along with the measured uncompensated frequency (dashed line). The frequency fluctuation is reduced to less than 15 Hz after compensation, showing that temperature-

induced frequency changes can be effectively compensated for. The temperature coefficient of resonance frequency (TCf) of the resonator is reduced from -33.5ppm/°C to -0.87ppm/°C after compensating temperature induced frequency drift.
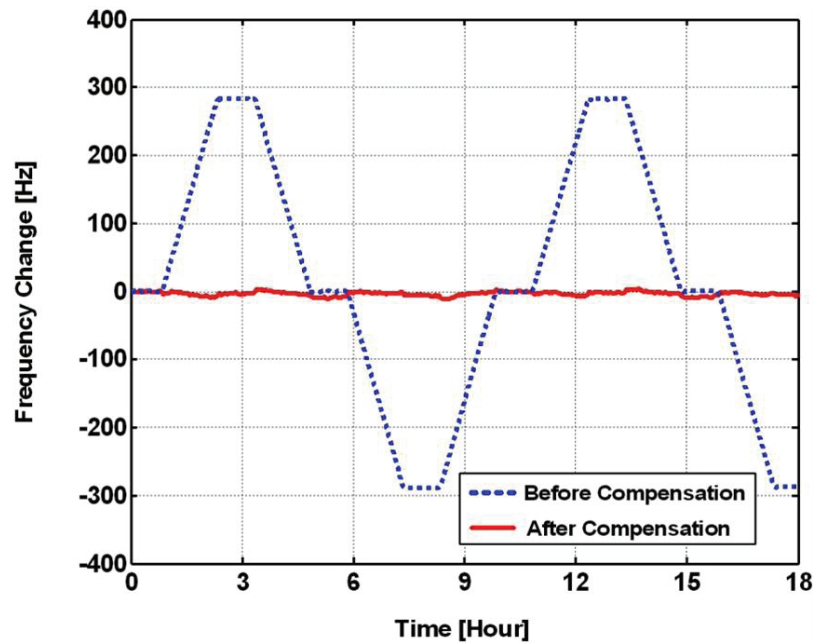
Fig. 6.15: Measured (dashed line) and compensated (solid line) resonance frequency change of disk resonator subject to ambient temperature changes between 30 and 60°C.

Fig. 6.16 plots the measured and estimated relative frequency change of the resonator as a function of the environment temperature. Note that the calculation of the estimated frequency change requires no knowledge of the actual temperature.
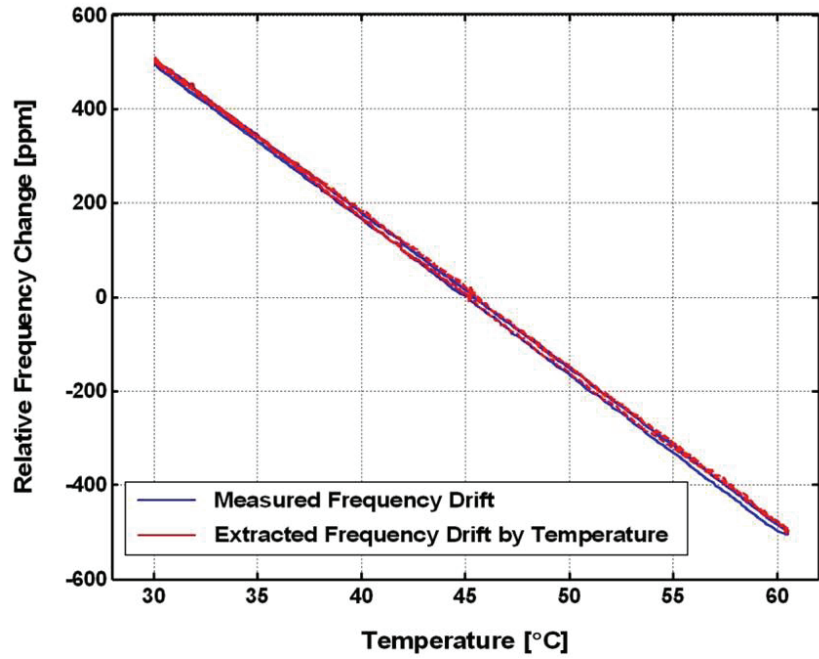
(a)
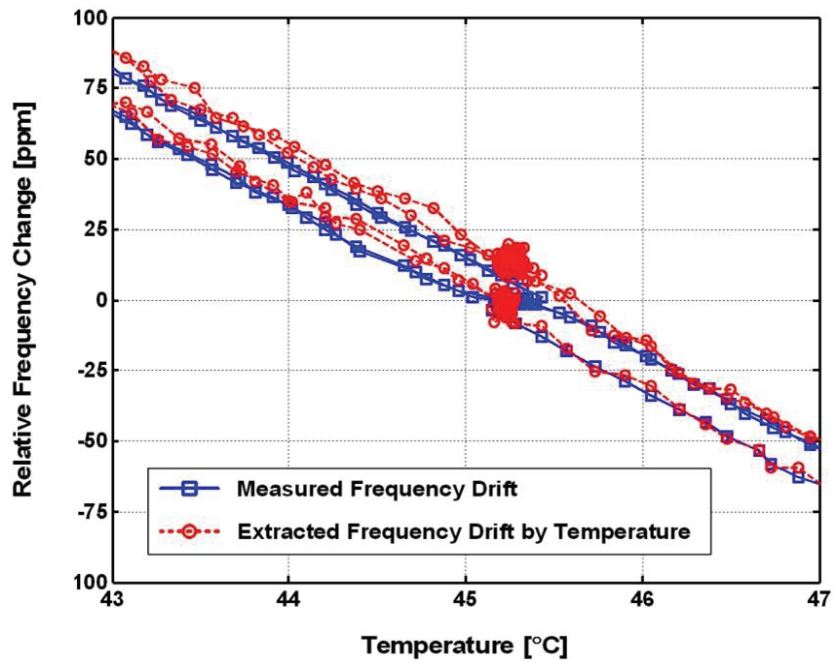
(b)

Fig. 6.16: Frequency change during thermal cycling: (a) measured and extracted frequency change as a function of the ambient temperature; (b) expanded plot of (a) in the temperature range from 43 to 47°C.

The measured frequency change shows a small thermal hysteresis during thermal cycling. Even though this hysteresis is not considered during the calibration step, the extracted relative frequency drift keeps track of this thermal hysteresis pretty well over the temperature range from 35 to 55°C.

To estimate the limit of the proposed method in compensating the temperature-induced frequency drift of a resonator, experiments were carried out under small temperature variations between 43 and 45°C (see Fig 6.17). The temperature compensated resonance frequency shows around 3 Hz variations. With the help of proper data processing techniques, the compensated frequency drift is expected to decrease further in the future and temperature induced frequency drifts of less than 5 ppm appear feasible with the proposed method.
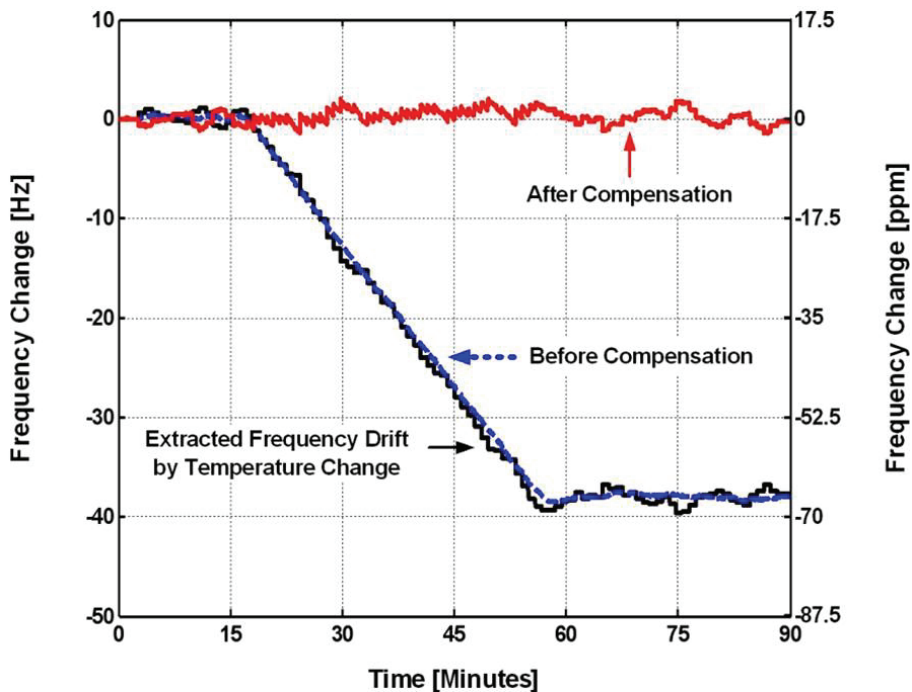
Fig. 6.17: Measured and compensated resonance frequency change of a resonator when subjected to a 2 °C temperature variation.

6.5 Discussions and Conclusions

The temperature compensation method introduced here is promising in compensating for the temperature-induced frequency drift of a resonator. The developed compensation scheme requires only one additional feedback loop, which can be implemented with simple electronic circuitry. Therefore, this method can be applied to any resonant microstructure featuring excitation and detection elements.

In evaluating the compensation method, the frequency change of a resonator under varying temperature is assumed entirely caused by stiffness changes of the mechanical structure. However, as all experiments are carried out under changing environmental conditions, the frequency change by mass uptake may not be negligible compared to the frequency drift by stiffness change. Therefore, the influence of other environmental factors on the proposed compensation method should be more carefully investigated in the future. Moreover, the influence of temperature on the effective resonator mass (due to thermal expansion) might need to be considered and ultimately limits the mass resolution with applied stiffness compensation method.

The ratio of the relative Q-factor change to the relative frequency change is determined during a calibration step as explained before. However, if the extracted relative Q-factor change is normalized by the absolute frequency change with and without compensation loop, the frequency drift of the resonator is compensated without any calibration step. Even though this fact is only based on the measurement results, it is worth investigating in the future.

CHAPTER 7

BIOCHEMICAL SENSING

The performance evaluation of the designed disk resonator as a biological sensor in a liquid environment is executed using the specific binding of β-galactosidase enzyme and anti-β-galactosidase antibody. The β-galactosidase enzyme is covalently immobilized onto the PECVD silicon nitride surface of the resonator and the resonance frequency change caused by anti-β-galactosidase antibody binding is monitored. The enzyme immobilization protocol, the experiment procedures and the measurement results are described in this chapter.

7.1. Enzyme Immobilization Method

Enzymes as biocatalysts have received increasing attention and have been investigated in the development of biosensors in areas such as medical diagnostics and environmental monitoring. Besides enabling catalytic reactions under mild conditions (ordinary temperature, atmospheric pressure and pH $\cong$ 7), their strict substrate and reaction specificity make enzymes more attractive than chemical catalysts for biosensing applications. Compared to soluble enzymes, immobilized enzymes offer several advantages including: i) activity stability over long time periods, ii) reduced sensitivity to environmental changes such as temperature or pH, and iii) activity improvement [113-115].

Depending on the specific binding sites of an enzyme that will be utilized for the biosensing applications, a proper immobilization method must be selected. The selected

method should avoid reactions with the essential binding sites of the enzyme and reduce any damage to the enzyme activities as far as possible. Enzyme immobilization methods are generally classified into three basic categories, namely i) the carrier-binding method, ii) the cross-linking method and iii) the entrapping method [115], and are briefly summarized in the following.

The carrier-binding method, in which the enzyme is immobilized to a water-insoluable solid support, is based on the enzyme binding through physical adsorption, ionic bonding or covalent bonding. Enzyme immobilization methods by adsorption or ionic bonding are relatively simple and can be achieved under mild conditions. However, due to the weak binding forces between enzyme and substrate, enzyme leakage from the substrate can be substantial and depends on changes in temperature or pH of the environment. In contrast, enzymes immobilized by strong covalent bonding are more stable and more resistant to the operating conditions. The solid-support needs a proper surface modification or activation to form covalent bonds to the enzymes. Any reactive components on the enzyme surface, such as amino, carboxyl, thiol or hydroxyl groups, can be used for covalent bonding to the activated or functionalized surface of the support material [116].

In case of the cross-linking method, enzymes are joined together by inter-molecular cross-linking by means of bi-functional or multi-functional reagents. As the enzymes are not attached to a solid support, some of the enzyme's protein material acts as a support, thus resulting in relatively low enzyme activity. The cross-linking method is generally combined with other immobilization methods for stabilizing adsorbed enzyme or preventing leakage [115].

Finally, enzyme immobilization by entrapping is based on the physical confinement of enzyme molecules within the lattice of a polymer matrix or semi-permeable membrane. The enzymes do not bind to the membrane or polymer matrix and, therefore, this method provides a wider flexibility and applicability. However, when a chemical

polymerization reaction is carried out under severe condition, the enzyme activity loss can be substantial and, thus, limits the application of this method [115].

Among these enzyme immobilization methods, the carrier-binding approach based on covalent bonding is most attractive for resonant mass-sensitive sensors, especially when considering their vibratory motion. Enzyme immobilization protocols onto silicon oxide or silicon nitride surfaces have already been widely investigated (see next section for details). Therefore, the covalent immobilization method has been also adopted in this work to immobilize β-galactosidase enzyme onto the PECVD silicon nitride surface of the fabricated disk resonators.

7.1.1 Covalent Enzyme Immobilization

Covalent binding of proteins to sensing surfaces is widely used because it can provide a highly irreversible surface loading and is relatively resistant to the operating conditions [9-11]. The dominant loss mechanism of covalently immobilized protein is the continuous desorption of non-covalently bound protein left from incomplete washing after the immobilization procedure. The possibility of a high surface loading makes the covalent immobilization method attractive for resonant microsensors.

Two covalent immobilization methods have been generally used for attaching enzymes to inorganic surfaces, either using silanes or mono-layered thiols on gold surfaces [117].

Surface treatment with silanes is widely used for bio-molecular immobilization especially to silica surface, because the covalent bonding of the silane to the solid support is readily formed through Si-O-Si bonding. Many of the enzyme immobilization methods use either amino-terminated or thiol-terminated silanes. Covalent binding of the enzymes to the reactive groups of the silanes is carried out using cross-linking agents, such as glutaraldehyde. The successful enzyme immobilization using amine-terminated silane and glutaraldehyde as a cross-linking agent has been demonstrated in [118]. The two

reactive free aldehyde groups (-CHO) of the glutaraldehyde form strong covalent bonds to protein nitrogen with which they come in contact, thus showing a high cross-linking ability. Enzyme immobilization onto glass and platinum surfaces was also demonstrated using a thiol-terminated silane and a heterobifunctional cross-linker [114, 119]. The chemistry includes a covalent bond formation between a hydroxyl group on the sensor surface, a thiol-terminated silane, a heterobifunctional cross-linker, and the enzyme. One end of the heterobifunctional cross-linker reacts with the thiol group on the silane, while the other functional moiety couples to the bio-molecule. With the thiol-terminated silane, a wider variety of cross-linkers can be used for enzyme immobilization [119].

Another method is using thiol monolayers as an anchor layer for the immobilization of enzyme molecules [120]. Thiols are known to form self-assembled monolayers on gold surfaces and the bonding of the thiol groups to gold is sufficiently strong to be stable [121-123]. Several proteins such as DNA, BSA (bovine serum albumin), antibodies and enzymes have been immobilized onto gold surface using thiol monolayers [19, 120, 122, 124]. For the application of these methods to the microresonators, a thin gold or platinum layer must be deposited onto the resonator surface.

7.1.2 Immobilization Protocol for β-galactosidase Enzyme

For the immobilization of the β-galactosidase enzyme on the surfaces of the disk-type microstructures, the protocol suggested by Williams and Blanch [118] was modified. The enzyme loading to PECVD silicon dioxide and silicon nitride surfaces was characterized in collaboration with Dr. Lorena Betancor and Dr. Jim Spain of the School of Civil and Environmental Engineering at the Georgia Institute of Technology. Surface loadings up to 0.045 IU (0.37 μg) were obtained on 5 mm × 5 mm silicon samples coated with the same passivation layers as the microresonators [12]. The immobilization steps

and the chemical reactions involved are summarized in Figure 7.1. A detailed description of each immobilization step used in this work is given below:

1. Prepare a 10% nitric acid (HNO_3) solution in distilled water and drop it onto the sensor surface with a pipette. Incubate the resonator in an oven at 80°C for 20 minutes. This step activates the surface silanol groups (SiOH) on the surface oxide layer of the PECVD silicon nitride as illustrated in Figure 7.1 (a).

2. Clean the sample thoroughly with distilled water.

3. Prepare a 10% aminopropyltriethoxysilane (APTES) solution in distilled water and adjust its pH to 7 with 10% acetic acid (CH_3COOH). Drop the prepared solution onto the resonator and incubate it in an oven at 80°C for 4 hours. Reactive amino groups (NH_2) are provided to the sensor surface after this step as shown in Figure 7.1(b).

4. Clean the resonator again with distilled water.

5. Prepare a 15% glutaraldehyde solution in pH 7, 200mM sodium phosphate buffer (PBS) solution. Drop the prepared solution onto the resonator surface and incubate at room temperature for 8 hours. One of the two aldehyde groups of the glutaraldehyde covalently binds to the reactive amino group on the resonator surface which is provided by APTES.

6. Remove excess glutaraldehyde by rinsing thoroughly with running distilled water.

7. Prepare a 0.01mg/ml enzyme solution in 25mM PBS solution. Drop the enzyme solution onto the resonator and wait 15 minutes at room temperature. A covalent bond between the enzyme and the glutaraldehyde is formed during this time.

8. Remove non-specifically bound enzyme thoroughly with distilled water.

9. Store the enzyme-immobilized resonator in a refrigerator at 4°C.

An SEM image of the silicon nitride surface after the β-galactosidase enzyme immobilization is shown in Figure 7.2.
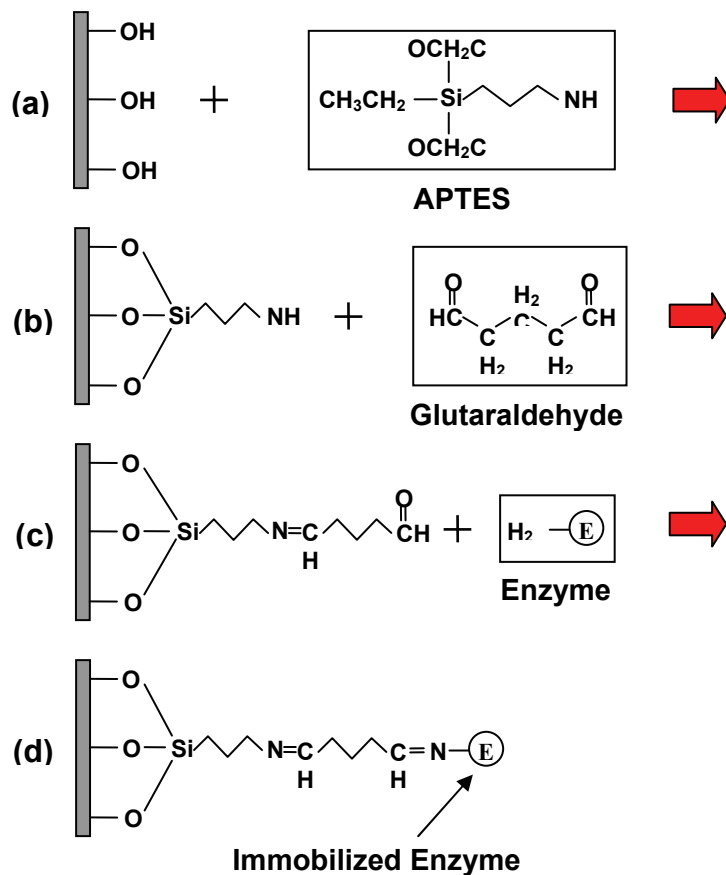
Figure 7.1: Chemical reaction sequence to covalently immobilize β-galactosidase enzyme onto silicon nitride surfaces.
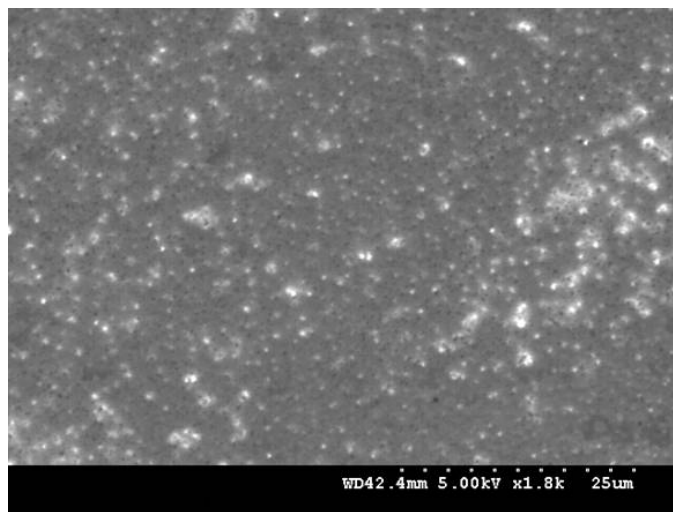
Figure 7.2: SEM image of a silicon nitride surface after β-galactosidase enzyme immobilization.

7.2. Materials and Methods

7.2.1 Materials and Sample Preparation

The fabricated sensor chips are diced and cleaned using an oxygen plasma and acetone, followed by thorough rinsing with DI water. The chips containing four disk resonators are now attached to 28-pin DIL packages using UV curable epoxy (OZ116 from Epoxy Technologies) as die adhesive and electrical interconnects are formed by wire bonding. The enzyme immobilization steps outlined in the previous section are executed on the surface of the wire-bonded chip. As the chemical solutions are handled and dropped onto the chip manually using a pipette, a localized enzyme immobilization only on the disk area of the resonators cannot be achieved. Therefore, adsorbed enzymes or any chemical residues on the pad areas can interfere with the wire bonding after enzyme immobilization. To avoid this problem, the enzyme immobilization is carried out in this study after wire bonding.

Nitric acid (Fisher A200-500), APTES (Fluka 09327) and 25% glutaraldehyde solution (Sigma-Aldrich G5822) are diluted to the necessary concentrations. The β-galactosidase enzyme from Escherichia coli is obtained from Sigma (G2513) and the anti-β-galactosidase IgG monoclonal antibody purified from ascites of a mouse hybridoma is purchased from Promega (Z3781) with a concentration of 2.2 mg/ml in 10 mM Tris-HCl, 150 mM NaCl, and 0.02 % sodium azide.

7.2.2 Measurement Setup

The open-loop frequency response of the resonators is measured at atmospheric pressure and room temperature after wire bonding, and measured again after immobilization to estimate the mass loading by the immobilized enzyme. All bonding wires and pads are sealed with UV (ultra violet) curable epoxy and cured under UV light for 1 hour. The flow cell guiding the antibody solution to the resonator is made of a

PMMA (polymethylmethacrylate) sheet and mounted on top of the DIL packages as shown in Figure 7.3.

<div align="center">(a)   (b)</div>

<div align="center">(c)</div>
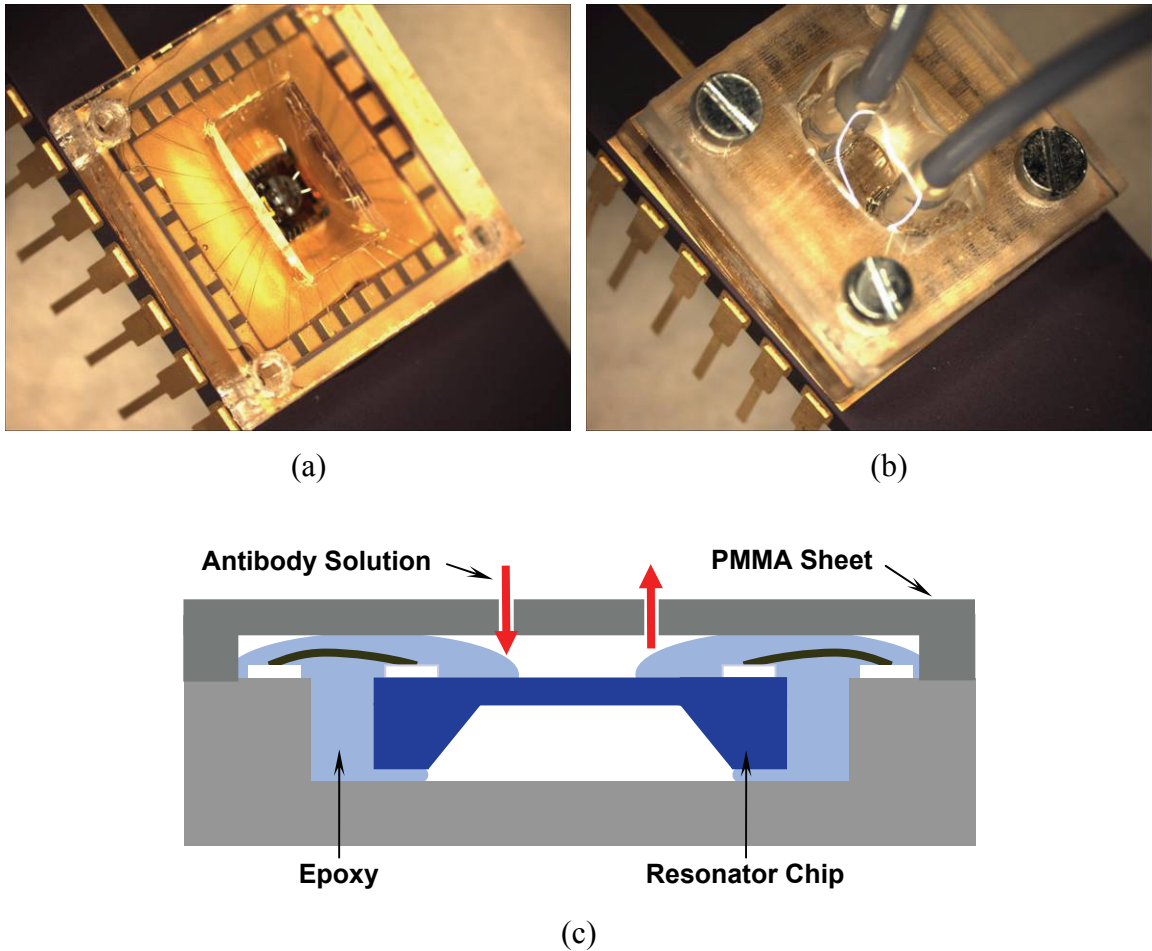
Figure 7.3: PMMA flow cell: (a) flow cell body attached on top of the DIL package, (b) flow cell cover mounted onto DIL package, (c) cross section of the flow cell.

The antibody concentration is adjusted using two computer-controlled syringe pumps, each of which controls the flow rate of a diluted anti-β-galactosidase antibody solution and of water. The syringes containing antibody and water are kept at the same temperature before executing measurement to avoid a temperature change of the solution when mixed together, thus preventing temperature-induced resonance frequency changes

of the resonator. The two solutions from the syringe pumps are mixed at a T-junction and supplied to the flow cell through PEEK (polyetheretherketone) tubing. The resonance frequency of the enzyme-coated resonator operated in an amplifying feedback loop is measured with a frequency counter. The overall measurement setup is shown in Figure 7.4.
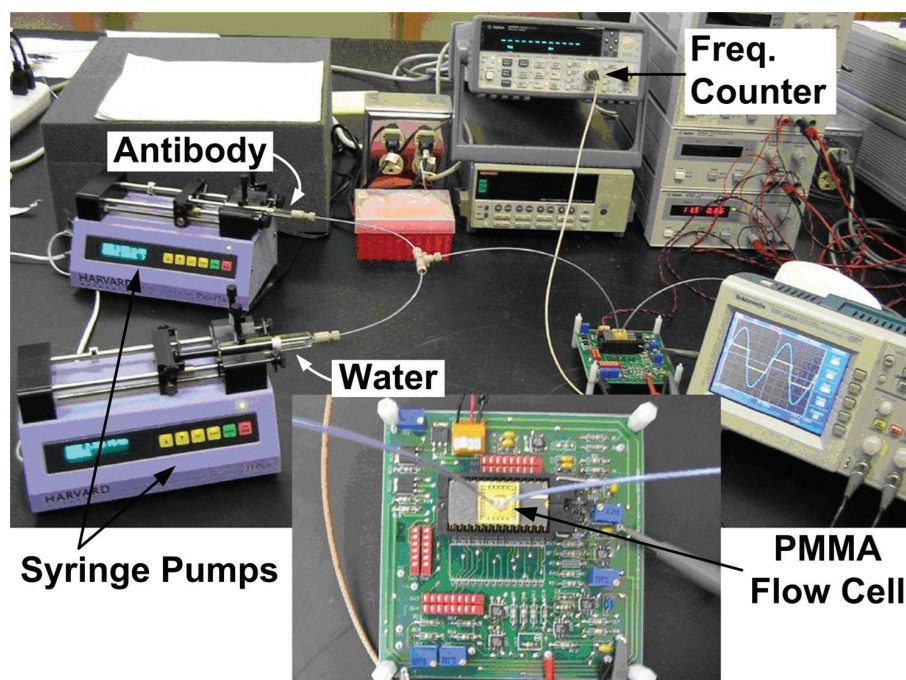
Figure 7.4: Test setup for biochemical sensing with syringe pumps and flow-cell (see close-up) mounted on top of packaged microresonator.

7.3. Measurement Results

7.3.1 Mass-Loading by Immobilized Enzyme

The enzyme loading on the disk resonator surface is estimated by comparing the resonance frequencies before and after enzyme immobilization. The measured relative frequency changes $\Delta f/f$ upon enzyme immobilization are summarized in Figure 7.5.
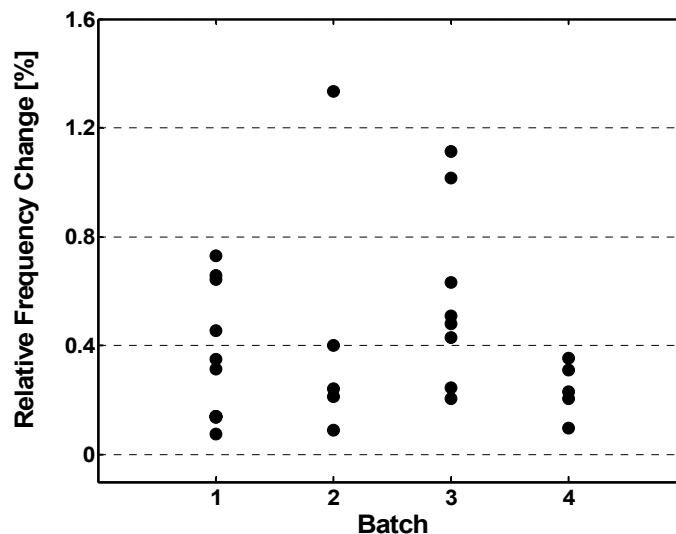
Figure 7.5: Relative frequency change Δf/f of 26 resonators from 4 coating batches after enzyme immobilization.

If monolayers of enzyme are covalently immobilized on the resonator surface, the relative frequency change upon enzyme loading should show only small deviations independent of the processing batch. However, the measured relative frequency changes before and after enzyme immobilization showed substantial variation from sample to sample and from batch to batch, as can be noted in Figure 7.5. This might indicate that the immobilized enzyme is not a monolayer but multiple layers of protein and that a significant quantity of enzyme molecules are adsorbed instead of covalently bonded on the resonator surface. Sufficient cleaning after each step of the immobilization sequence is critical to prevent adsorption of enzyme molecules, but the small cavity under the resonators and the small air gap between the resonators and the silicon substrate make cleaning challenging. Even though the adsorbed enzyme on the glutaraldehyde support is not easily desorbed [118], adsorbed enzymes are less stable than the covalently immobilized enzyme [10, 12] and can cause unstable and irreproducible sensor responses.

7.3.2 Resonance Frequency Stabilization

Adsorbed enzyme molecules can be washed away from the resonator surface or floating enzyme molecules inside flow channel can be adsorbed back to the resonator surface during operation in liquid environment, thus causing an unstable resonance frequency of the resonator. Besides adsorbed enzymes, residues coming from the fabrication or dicing process, and trapped air bubbles inside the flow cell can also cause unpredictable frequency fluctuations.

To measure only the frequency change by specific binding of antibodies to the immobilized antigens (enzymes), the enzyme-immobilized resonator is operated in water at a constant flow rate of 8 μL/min until the resonance frequency of the resonator stabilizes. Figure 7.6 shows a typical frequency output of a disk resonator during this stabilization step.
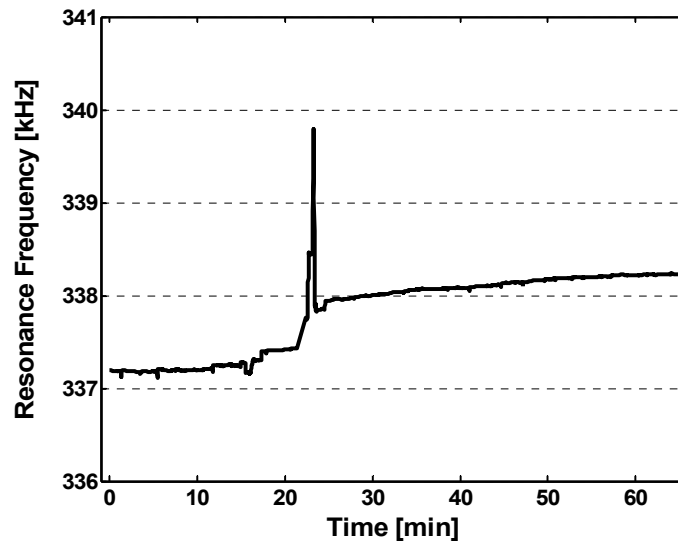
Figure 7.6: Resonance frequency of a resonator during the initial stabilization step in DI water at a flow rate of 8 μl/min.

As can be noted in Figure 7.6, an abrupt frequency jump is observed 20~30 minutes after initial water injection and the resonance frequency slowly approaches to a stable value after about 1 hour. Without sufficient stabilization in water, an unstable resonance frequency of the resonator is observed when antibody solution is injected through the flow cell, as shown in Figure 7.7.
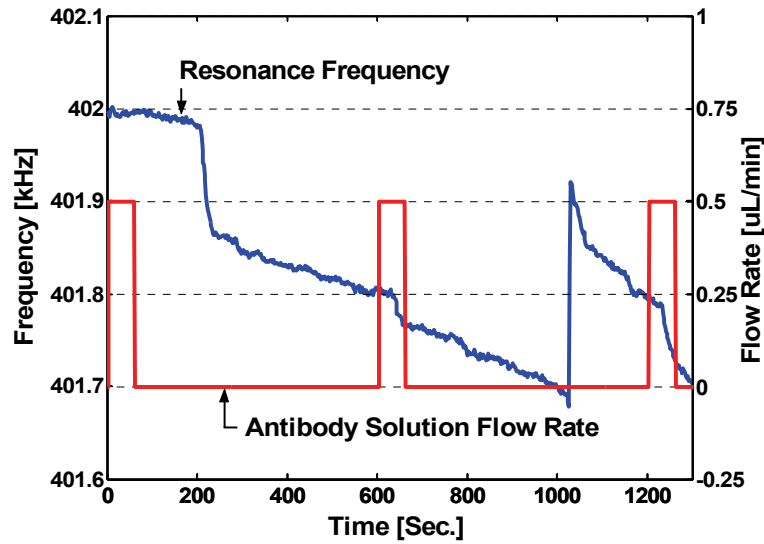
Figure 7.7: Unstable resonance frequency during anti-β-galactosidase antibody injection into the flow cell.

7.3.3 Antibody Injection Test

A disk resonator of r_1 = 150 μm, r_2 = 40 μm, g = 20 μm has been used for this experiment. From the surface area of the chosen disk resonator, the mass loading by immobilized enzyme is roughly estimated first under the assumption that the immobilized enzymes are forming a mono-layer. The dimensions of β-galactosidase from E-coli, 175×135×90 Å [125], is approximated as 150×150×150 Å and the molecular weight of 465kD is used for the mass loading estimation. If both sides of the resonator are

uniformly coated with a mono-layer of enzyme, then 347 pg mass loading or a frequency change of less than 300 Hz is expected. However, the resonance frequency decreased by approx. 2.2 kHz after enzyme immobilization, which is almost 6 times more than expected as shown in Figure 7.8.
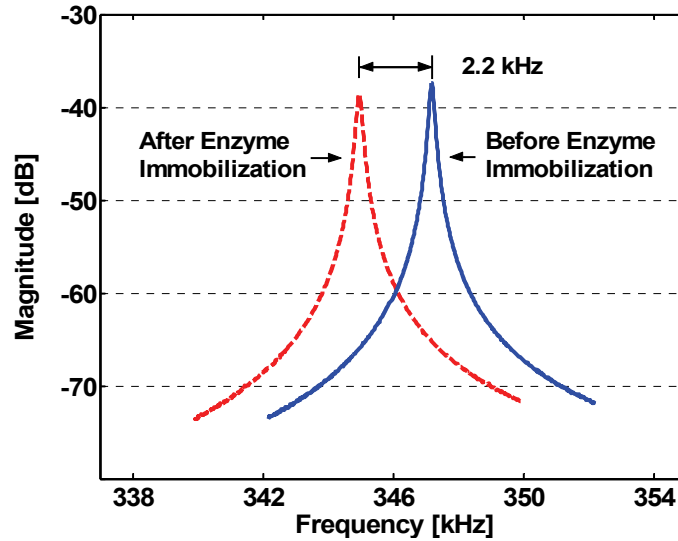
Figure 7.8: Amplitude transfer characteristic of a disk resonator with radius of 150 μm around the in-plane resonance frequency before and after enzyme immobilization.

Figure 7.8 is the open-loop frequency response of the resonator in air before and after enzyme immobilization. The higher than expected frequency change may be caused either by multiple layers of immobilized enzyme, or by a resonator stiffness change caused by thermal and chemical reactions during the immobilization process. However, the origin of the frequency change is difficult to evaluate by a frequency measurement itself.

Following the enzyme immobilization, a 0.73 μg/ml anti-β-galactosidase antibody solution was prepared by diluting 1 μl of 2.2 mg/ml antibody solution with water by 1:3,000. The enzyme immobilized resonator, attached to the PMMA flow cell, was

operated in water for several hours until its frequency signal stabilized at a constant flow rate of 8 μl/min as shown in Figure 7.6. After the frequency of the resonator stabilized in water, 0.5 μl antibody solution containing approximately 0.36 ng antibody was injected every 10 minutes at a flow rate of 0.5 μl/min, while maintaining a constant total flow rate of 8 μl/min through the flow cell.

Figure 7.9 shows the resonance frequency over time. A distinct frequency change occurs about 2~3 minutes after the antibody injection into the flow cell. The combined volume of the tubing and the sample chamber inside the flow cell causes this time delay. After the first antibody injection, the resonance frequency decreases by approx. 1 kHz while the frequency drop is approx. 400 Hz after the second antibody injection. After the third injection, the frequency change is barely visible, indicating the gradual saturation of the antibody binding sites on the enzyme coated resonator surface.
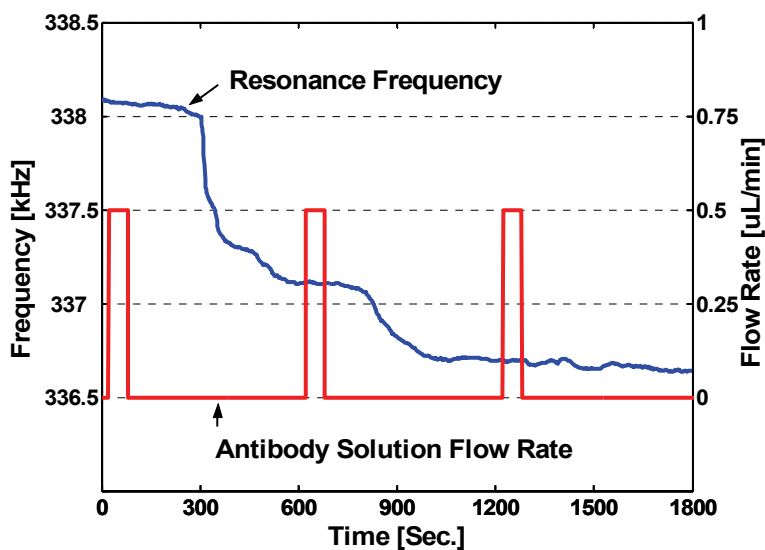
Figure 7.9: Resonance frequency of disk resonator as a function of time while periodically injecting antibody solution containing 0.36 ng anti-β-galactosidase per injection cycle.

The resonator showed a larger frequency decrease than expected from the mass sensitivity of the chosen disk resonator and the 0.36ng antibody mass per injection cycle. A viscosity change by the injected antibody solution cannot explain such a high frequency change because the solution is highly diluted with water. Considering a temperature coefficient of the resonance frequency of -30 ~ -60 ppm/°C, the observed frequency change of $\approx$ 4000 ppm is certainly not caused by a temperature change. Compared to the above mentioned possibilities, binding of organic impurities or an error in the concentration of the prepared antibody solution are more probable causes of the high frequency change. In addition, if the bound antibody is concentrated at the edge of the disk resonator, it may cause higher frequency changes because of the larger change in the mass moment of inertia. However, to evaluate the sensor resolution and sensitivity more quantitatively, more careful and precise experiments must be carried out in the future.

7.4. Discussions and Conclusions

The initial results demonstrate that the disk resonator vibrating in a rotational in-plane mode can be used as a biological sensor, detecting in this particular experiment the specific binding of anti-β-galactosidase antibody to immobilized β-galactosidase enzyme. Considering the short-term frequency stabilities of the disk resonators as low as 2.3×10^{-6} in water, mass detection limits in the low or even sub-picogram regime are expected in liquid environment. Even though the measurement results are promising, a precise estimation of sensor sensitivities and resolution has not been carried out yet. Furthermore, the measurement setup, the flow cell design and the immobilization procedure must be optimized in the future to improve the reliability and repeatability of the sensor response. A few possible ways of improvement are highlighted in the following.

The enzyme immobilization method chosen in this work is not suitable for localized enzyme coating, i.e. only on the disk areas, if no special dispensing system is used. From this point of view, immobilization methods based on thiol monolayers on gold surfaces are more attractive than the method investigated in this work. When a thin layer of gold is deposited on the disk area during the fabrication process, enzyme immobilization only on the disk area becomes feasible with thiol-based immobilization methods, thus improving the detection limit of the sensor for a given volume of antibody solution.

Moreover, modifications to the measurement setup and the flow channel design are required to get more predictable sensor responses when antibody solution is injected. Considering the small volume of antibody solution per injection, air bubbles trapped inside the T-junction (where the antibody solution is mixed with the carrier solution) cause a substantial time delay in detecting measurable frequency changes of a resonator after antibody injection. Therefore, the start of the real antibody injection to the flow channel is unpredictable. A four-way switching valve might be more suitable than the T-junction in this respect. In addition, air bubbles trapped inside the cavity under the resonators, which cause frequency instabilities, are hard to remove with the current flow channel design. For easy removal of trapped air bubbles, a flow cell design, which guides the liquid flow from the top of the resonator to the bottom cavity under the resonator, is more preferable.

CHAPTER 8

CONCLUSION

The main objective of this research is the performance improvement of microresonators in mass-sensitive chemical and biological sensing applications. Two approaches have been investigated in this thesis. The first approach is based on improving the frequency resolution by designing a microresonator with high Q-factor in air and liquid environment. The second approach is based on minimizing the frequency drift of microresonators by compensating for frequency drift caused by temperature and, thus, stabilizing the resonance frequency.

A new disk-shape resonant microstructure vibrating in a rotational in-plane mode has been investigated in this work. The designed resonators feature integrated electrothermal excitation elements and a piezoresistive Wheatstone bridge for vibration detection, which is sensitive only to the desired rotational in-plane vibration mode. Microresonators with different dimensions and resonance frequencies between 300 and 1,000 kHz have been fabricated and extensively characterized both in air and in water. By shearing the surrounding fluid instead of compressing it, damping is reduced and quality factors up to 5,800 in air and 94 in water have been measured. The integrated excitation and detection elements enable a closed-loop operation of the disk-type resonators, and frequency stabilities, measured with the Allan-variance method at 1-sec gate time, as low as 1.07×10^{-8} in air and 2.3×10^{-6} in water have been obtained. Considering the sub-microgram mass of the disk resonators, these frequency stabilities translate into mass detection limits in the low femto-gram and pico-gram range in air and liquid, respectively. With its promising performance characteristics compared to the more conventional cantilever-based microresonators, the designed disk-type resonators are

152

promising transducer candidates for a mass-sensitive chemical and biological sensing platform.

Analytical models for the resonance frequency and the Q-factor of the designed resonators have been derived to facilitate their design optimization. Despite many simplifying assumptions, the derived analytical models showed good agreement with FEM simulation data and experimental results, especially in air. However, a more careful and systematic analytical analysis is required to explain the differences between measured and calculated Q-factors in water. Especially, the mass loading effect by the surrounding fluid and the squeezed film damping have to be considered to derive an improved analytical model for the disk resonators.

The potential application of the designed resonators for biological sensing in a liquid environment has been demonstrated experimentally using the specific binding of anti-β-galactosidase antibody to β-galactosidase enzyme immobilized on the resonator surface. The resonators exhibited a stable response when exposed to the antibody solution, and showed an approx. 1 kHz frequency change upon injection of 0.36 ng of antibody. However, a precise estimation of the sensor sensitivity and resolution in detecting the anti-β-galactosidase antibody has not been done yet. This requires an improved repeatability of the sensor response, and in particular a careful redesign of the measurement setup and the flow cell. Moreover, the enzyme immobilization method must be optimized to enable a localized deposition of the β-galactosidase enzyme only in the disk areas of the resonator.

The second approach for improving the mass detection capability of microresonators is based on the compensation for resonance frequency drifts caused by temperature changes. The compensation method is based on a controlled stiffness change introduced by an additional feedback loop and relative quality-factor changes are extracted by investigating the resonance frequency shift by the additional feedback loop. Temperature-induced relative quality factor changes are exploited to estimate

temperature changes of the resonator. By compensating for subtle temperature changes, the resonance frequency variation caused by mass changes, i.e. the effective sensor signal, can be assessed more precisely. The obtained measurement results indicate that temperature-induced frequency changes even in the low ppm range can be compensated with the developed method. A particular advantage of the compensation scheme is that it only requires an additional feedback loop, thus this method can be applied to other resonators without structural modifications. Moreover, the temperature dependence of the excitation and detection elements does not influence the precision of the proposed compensation method. However, influences of other environmental factors on the developed compensation method are not carefully investigated yet. Furthermore, the compensation method still requires a calibration step for temperature compensation.

Two possible approaches to improve the performance of resonant microstructures as mass sensitive sensors have been demonstrated in this thesis. Clearly, a creative design of the resonant microstructure, coating strategies, which are optimized for the micro-scale structure, and clever compensation techniques are keys to any successful commercialization of a resonant mass-sensitive biochemical sensor.

APPENDIX A

FEEDBACK CIRCUIT FOR TEMPERATURE COMPENSATION

The implemented feedback circuit for effective stiffness modulation of a microresonator is given below.
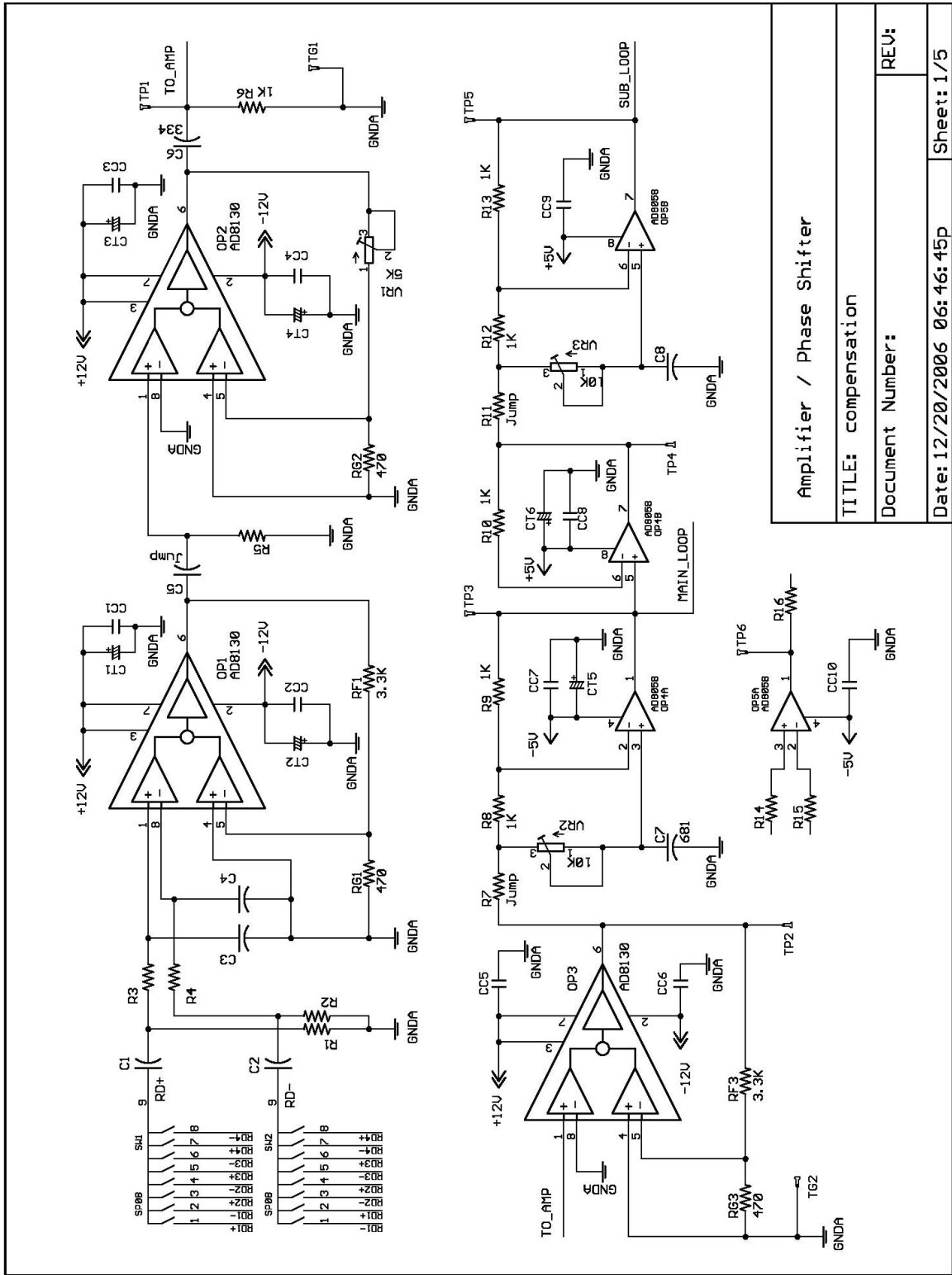
Figure A.1: Pre-amplifiers and phase-shifter circuits.
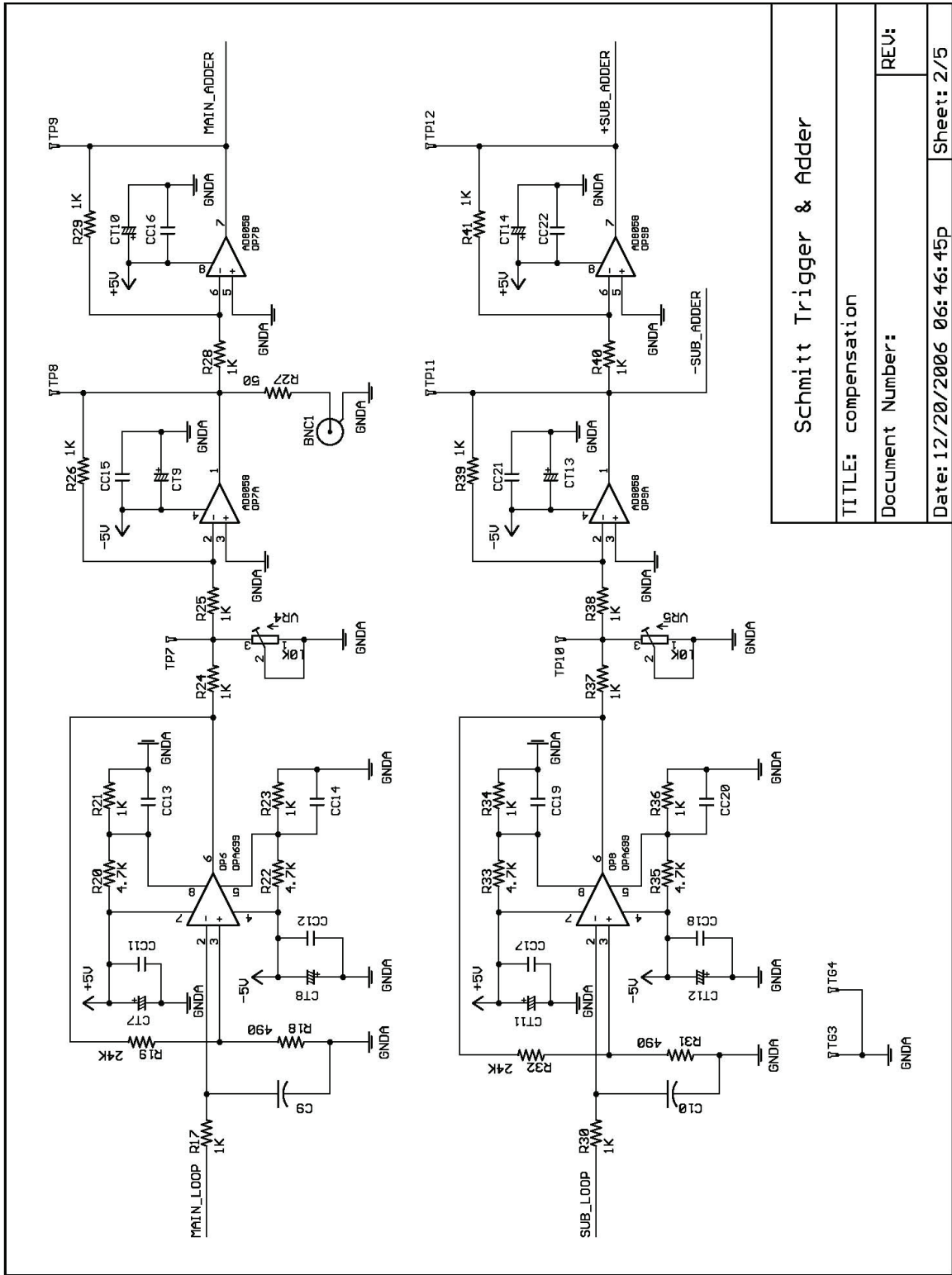
Figure A.2: Voltage limiter and adder circuits.
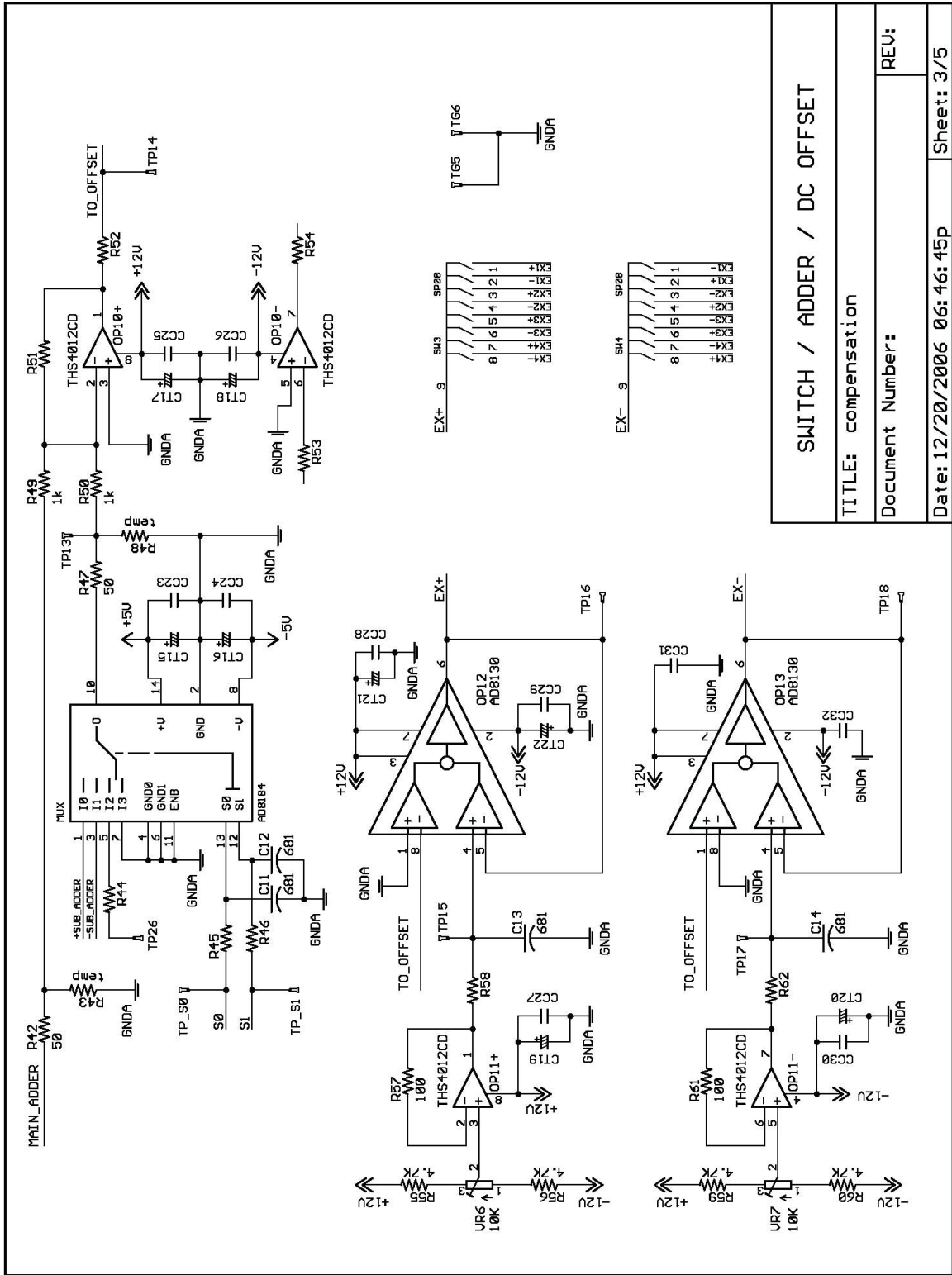
Figure A.3: Switch and level-shifter circuits.
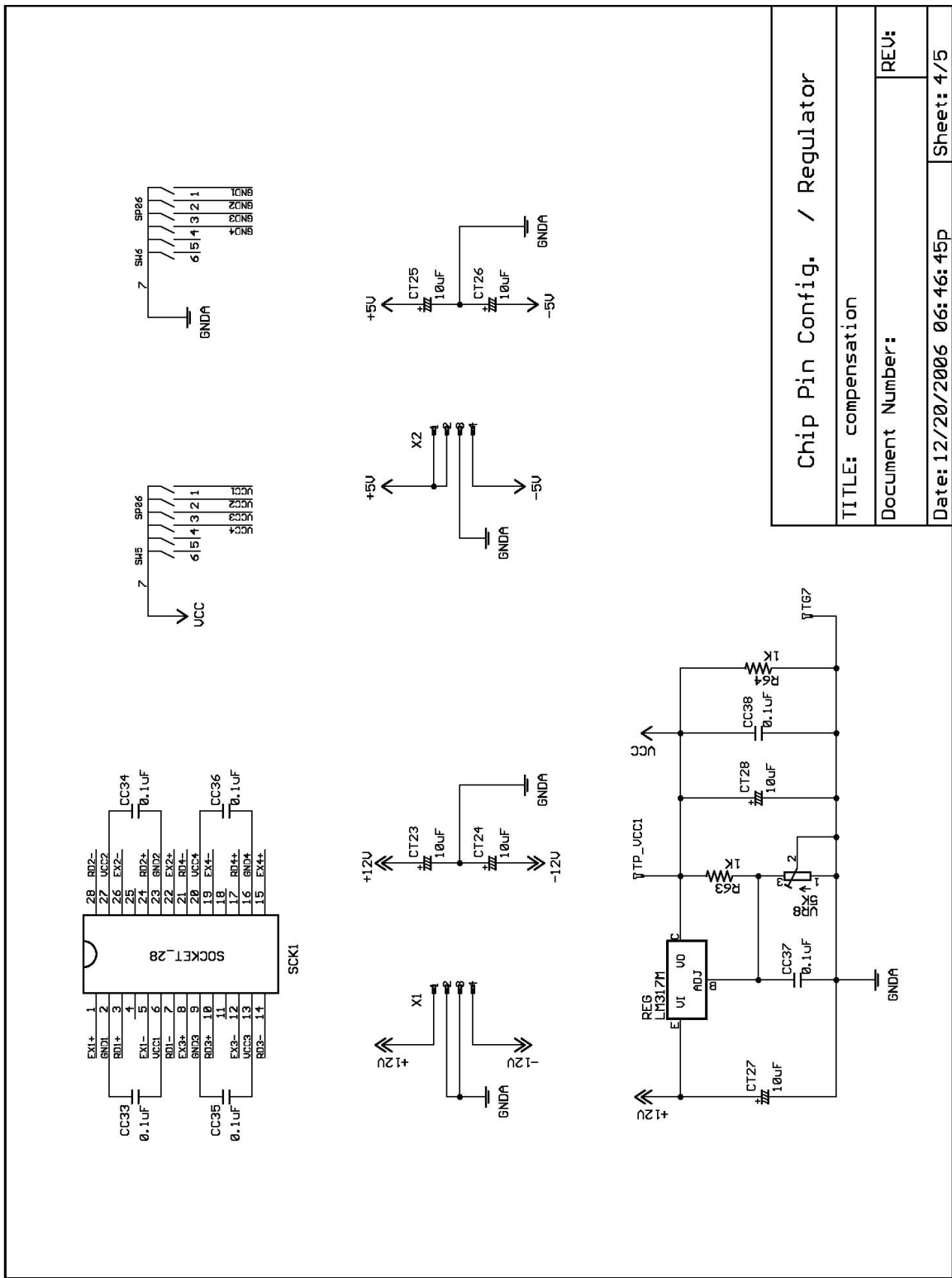
Figure A.4: Power connector and voltage regulator circuit.

REFERENCES

[1]   "Chemical Sensors: Liquid, Gas and Biosensors," Freedonia Industry Study #1547, April 2002.

[2]   G. A. Campbell and R. Mutharasan, "Detection of pathogen Escherichia coli O157:H7 using self-excited PZT-glass microcantilevers," *Biosensors and Bioelectronics*, vol. 21, pp. 462-473, 2005.

[3]   B. Ilic, D. Czaplewski, M. Zalalutdinov, H. G. Craighead, P. Neuzil, C. Campagnolo, and C. Batt, "Single cell detection with micromechanical oscillators," *Journal of Vacuum Science and Technology B: Microelectronics and Nanometer Structures*, vol. 19, pp. 2825-2828, 2001.

[4]   J. Pei, F. Tian, and T. Thundat, "Glucose biosensor based on the microcantilever," *Analytical Chemistry*, vol. 76, pp. 292-297, 2004.

[5]   A. Hierlemann, O. Brand, C. Hagleitner, and H. Baltes, "Microfabrication techniques for chemical/biosensors," *Proceedings of the IEEE*, vol. 91, pp. 839-863, 2003.

[6]   T. P. Burg and S. R. Manalis, "Suspended microchannel resonators for biomolecular detection," *Applied Physics Letters*, vol. 83, pp. 2698-2700, 2003.

[7]   D. Lange, C. Hagleitner, A. Hierlemann, O. Brand, and H. Baltes, "Complementary metal oxide semiconductor cantilever arrays on a single chip: Mass-sensitive detection of volatile organic compounds," *Analytical Chemistry*, vol. 74, pp. 3084-3095, 2002.

[8]   C. Vancura, J. Lichtenberg, A. Hierlemann, and F. Josse, "Characterization of magnetically actuated resonant cantilevers in viscous fluids," *Applied Physics Letters*, vol. 87, pp. 162510, 2005.

[9]   O. Brand and H. Baltes, "Micromachined Resonant Sensors - an Overview," *Sensors Update*, vol. 4, pp. 3-51, 1998.

[10]   J. Janata, M. Josowicz, and D. M. DeVaney, "Chemical sensors," *Analytical Chemistry*, vol. 66, pp. 207-228, 1994.

[11]   J. Janata, M. Josowicz, P. Vanysek, and D. M. DeVaney, "Chemical sensors," *Analytical Chemistry*, vol. 70, pp. 179-208, 1998.

[12]   C. Hagleitner, A. Hierlemann, D. Lange, A. Kummer, N. Kerness, O. Brand, and H. Baltes, "Smart single-chip gas sensor microsystem," *Nature*, vol. 414, pp. 293-296, 2001.

[13]   P. Krebs and A. Grisel, "Low power integrated catalytic gas sensor," *Sensors and Actuators, B: Chemical*, vol. B13, pp. 155-158, 1993.

[14]   M. Zanini, J. H. Visser, L. Rimai, R. E. Soltis, A. Kovalchuk, D. W. Hoffman, E. M. Logothetis, U. Bonne, L. Brewer, O. W. Bynum, and M. A. Richard, "Fabrication and properties of a Si-based high-sensitivity microcalorimetric gas sensor," *Sensors and Actuators, A: Physical*, vol. 48, pp. 187-192, 1995.

[15]   C. Hagleitner, D. Lange, A. Hierlemann, O. Brand, and H. Baltes, "CMOS single-chip gas detection system comprising capacitive, calorimetric and mass-sensitive microsensors," *IEEE Journal of Solid-State Circuits*, vol. 37, pp. 1867-1878, 2002.

[16]   P. Bataillard, E. Steffgen, S. Haemmerli, A. Manz, and H. M. Widmer, "Integrated silicon thermopile as biosensor for the thermal monitoring of glucose, urea and penicillin," *Biosensors and Bioelectronics*, vol. 8, pp. 89-98, 1993.

[17]   Y. Zhang and S. Tadigadapa, "Calorimetric biosensors with integrated microfluidic channels," *Biosensors and Bioelectronics*, vol. 19, pp. 1733-1743, 2004.

[18]   N. V. Lavrik, M. J. Sepaniak, and P. G. Datskos, "Cantilever transducers as a platform for chemical and biological sensors," *Review of Scientific Instruments*, vol. 75, pp. 2229-2253, 2004.

[19]   Y. Arntz, J. D. Seelig, H. P. Lang, J. Zhang, P. Hunziker, J. P. Ramseyer, E. Meyer, M. Hegner, and C. Gerber, "Label-free protein assay based on a nanomechanical cantilever array," *Nanotechnology*, vol. 14, pp. 86-90, 2003.

[20]   J. Fritz, M. K. Baller, H. P. Lang, H. Rothuizen, P. Vettiger, E. Meyer, H. J. Guntherodt, C. Gerber, and J. K. Gimzewski, "Translating biomolecular recognition into nanomechanics," *Science*, vol. 288, pp. 316-318, 2000.

[21]   G. Wu, R. H. Datar, K. M. Hansen, T. Thundat, R. J. Cote, and A. Majumdar, "Bioassay of prostate-specific antigen (PSA) using microcantilevers," *Nature Biotechnology*, vol. 19, pp. 856-860, 2001.

[22]   E. Benes, M. Groschl, W. Burger, and M. Schmid, "Sensors based on piezoelectric resonators," *Sensors and Actuators, A: Physical*, vol. A48, pp. 1-21, 1995.

[23]   S. M. Sze, *Semiconductor sensors*, New York: Wiley, 1994.

[24]   S. Koller-Lucae, "Resonating viscosity sensors: micro versus macro approach," Ph.D. Thesis, ETH Zurich, 1999.

[25]   L. Rodriguez-Pardo, J. F. Rodriguez, C. Gabrielli, H. Perrot, and R. Brendel, "Sensitivity, noise, and resolution in QCM sensors in liquid media," *IEEE Sensors Journal*, vol. 5, pp. 1251, 2005.

[26]   C. Zimmermann, D. Rebiere, C. Dejous, J. Pistre, and R. Planade, "Love-waves to improve chemical sensors sensitivity: Theoretical and experimental comparison of acoustic modes," in *Proceedings of the 2002 IEEE International Frequency Control Symposium*, 2002, pp. 281-288.

[27]   M. Hoummady, A. Campitelli, and W. Wlodarski, "Acoustic wave sensors: Design, sensing mechanisms and applications," *Smart Materials and Structures*, vol. 6, pp. 647-657, 1997.

[28]   E. Gizeli, F. Bender, A. Rasmusson, K. Saha, F. Josse, and R. Cernosek, "Sensitivity of the acoustic waveguide biosensor to protein binding as a function of the waveguide properties," *Biosensors and Bioelectronics*, vol. 18, pp. 1399-1406, 2003.

[29]   E. Benes, M. Groschl, F. Seifert, and A. Pohl, "Comparison between BAW and SAW sensor principles," in *Proceedings of the 1997 IEEE International Frequency Control Symposium*, 1997, pp. 5-20.

[30]   R. Ince and R. Narayanaswamy, "Analysis of the performance of interferometry, surface plasmon resonance and luminescence as biosensors and chemosensors," *Analytica Chimica Acta*, vol. 569, pp. 1-20, 2006.

[31]   L. Gorton, *Biosensors and modern biospecific analytical techniques*, vol. 44, 1st ed. Boston: Elsevier, 2005.

[32]   M. D. Marazuela and M. C. Moreno-Bondi, "Fiber-optic biosensors - An overview," *Analytical and Bioanalytical Chemistry*, vol. 372, pp. 664-682, 2002.

[33]   B. Liedberg, C. Nylander, and I. Lundstrom, "Surface plasmon resonance for gas detection and biosensing," *Sensors and Actuators*, vol. 4, pp. 299-304, 1983.

[34]   www.wikipedia.com.

[35]   J. Homola, S. S. Yee, and G. Gauglitz, "Surface plasmon resonance sensors: review," *Sensors and Actuators, B: Chemical*, vol. B54, pp. 3-15, 1999.

[36]   B. Sepulveda, J. S. del Rio, M. Moreno, F. J. Blanco, K. Mayora, C. Dominguez, and L. M. Lechuga, "Optical biosensor microsystems based on the integration of highly sensitive Mach-Zehnder interferometer devices," *Journal of Optics A: Pure and Applied Optics*, vol. 8, pp. 561-566, 2006.

[37]   P. V. Lambeck, "Integrated optical sensors for the chemical domain," *Measurement Science and Technology*, vol. 17, pp. 93-116, 2006.

[38]   A. Brandenburg and A. Gombert, "Grating couplers as chemical sensors: a new optical configuration," *Sensors and Actuators, B: Chemical*, vol. B17, pp. 35-40, 1993.

[39]   W. Lukosz, P. M. Nellen, C. Stamm, and P. Weiss, "Output grating couplers on planar waveguides as integrated optical chemical sensors," *Sensors and Actuators, B: Chemical*, vol. B1, pp. 585-588, 1990.

[40]   P. M. Nellen, K. Tiefenthaler, and W. Lukosz, "Integrated optical input grating couplers as biochemical sensors," *Sensors and Actuators*, vol. 15, pp. 285-295, 1988.

[41]   G. Gauglitz, "Direct optical sensors: Principles and selected applications," *Analytical and Bioanalytical Chemistry*, vol. 381, pp. 141-155, 2005.

[42]   D. M. Wilson, S. Hoyt, J. Janata, K. Booksh, and L. Obando, "Chemical sensors for portable, handheld field instruments," *IEEE Sensors Journal*, vol. 1, pp. 256-274, 2001.

[43]   K. Domansky, D. L. Baldwin, J. W. Grate, T. B. Hall, J. Li, M. Josowicz, and J. Janata, "Development and calibration of field-effect transistor-based sensor array for measurement of hydrogen and ammonia gas mixtures in humid air," *Analytical Chemistry*, vol. 70, pp. 473-481, 1998.

[44]   J. Janata, "Electrochemical Microsensors," *Proceedings of the IEEE*, vol. 91, pp. 864-869, 2003.

[45]   T. Matsumoto, S. Saito, and S. Ikeda, "A multilayer membrane amperometric glucose sensor fabricated using planar techniques for large-scale production," *Journal of Biotechnology*, vol. 122, pp. 267-273, 2006.

[46]   A. Hierlemann, *Integrated Chemical Microsensor Systems in CMOS Technology*, 1st ed., New York: Springer Verlag, 2005.

[47]   L. A. Pinnaduwage, V. Boiadjiev, J. E. Hawk, and T. Thundat, "Sensitive detection of plastic explosives with self-assembled monolayer-coated microcantilevers," *Applied Physics Letters*, vol. 83, pp. 1471-1473, 2003.

[48]   J. R. Vig and F. L. Walls, "A review of sensor sensitivity and stability," in *Proceedings of the 2000 IEEE International Frequency Control Symposium*, 2000, pp. 30-33.

[49]   K. Arshak, E. Moore, G. M. Lyons, J. Harris, and S. Clifford, "A review of gas sensors employed in electronic nose applications," *Sensor Review*, vol. 24, pp. 181-198, 2004.

[50]   C. Qing-Yun, P. Jeongim, D. Heldsinger, H. Meng-Da, and E. T. Zellers, "Vapor recognition with an integrated array of polymer-coated flexural plate wave sensors," *Sensors and Actuators, B: Chemical*, vol. B62, pp. 121-130, 2000.

[51]   J. A. Covington, J. W. Gardner, P. N. Bartlett, and C. S. Toh, "Conductive polymer gate FET devices for vapour sensing," *IEE Proceedings-Circuits, Devices and Systems*, vol. 151, pp. 326-334, 2004.

[52] S. V. Patel, T. E. Mlsna, B. Fruhberger, E. Klaassen, S. Cemalovic, and D. R. Baselt, "Chemicapacitive microsensors for volatile organic compound detection," *Sensors and Actuators, B: Chemical*, vol. B96, pp. 541-553, 2003.

[53] P. T. Moseley, "Solid state gas sensors," *Measurement Science & Technology*, vol. 8, pp. 223-237, 1997.

[54] K. Y. Yasumura, T. D. Stowe, E. M. Chow, T. Pfafman, T. W. Kenny, B. C. Stipe, and D. Rugar, "Quality factors in micron- and submicron-thick cantilevers," *Journal of Microelectromechanical Systems*, vol. 9, pp. 117-125, 2000.

[55] Y. Jinling, T. Ono, and M. Esashi, "Energy dissipation in submicrometer thick single-crystal silicon cantilevers," *Journal of Microelectromechanical Systems*, vol. 11, pp. 775-783, 2002.

[56] A. Vidic, D. Then, and C. Ziegler, "A new cantilever system for gas and liquid sensing," *Ultramicroscopy*, vol. 97, pp. 407-416, 2003.

[57] J. Tamayo, A. D. L. Humphris, R. J. Owen, and M. J. Miles, "High-Q dynamic force microscopy in liquid and its application to living cells," *Biophysical Journal*, vol. 81, pp. 526-537, 2001.

[58] A. K. Kar and M. A. George, "Improved detection of thermally induced higher resonance modes and harmonics of a microcantilever," *Journal of Applied Physics*, vol. 94, pp. 4626-4631, 2003.

[59] A. Maali, C. Hurth, R. Boisgard, C. Jai, T. Cohen-Bouhacina, and J.-P. Aim, "Hydrodynamics of oscillating atomic force microscopy cantilevers in viscous fluids," *Journal of Applied Physics*, vol. 97, pp. 074907, 2005.

[60] G. Stemme, "Resonant silicon sensors," *Journal of Micromechanics and Microengineering*, vol. 1, pp. 113-25, 1991.

[61] H. Baltes. O. Brand, "Micromachined Resonant Sensors - an Overview," *Sensors Update*, vol. 4, pp. 3-51, 1998.

[62] F. Ayazi, *Advanced Micro and Nanosystems*, vol. 1: Wiley-VCH, 2004.

[63]   J. Bernstein, R. Miller, W. Kelley, and P. Ward, "Low-noise MEMS vibration sensor for geophysical applications," *Journal of Microelectromechanical Systems*, vol. 8, pp. 433, 1999.

[64]   D. S. Ballantine, *Acoustic wave sensors : theory, design, and physico-chemical applications*, Academic Press, 1997.

[65]   I. J. Busch-Vishniac, "The case for magnetically driven microactuators," *Sensors and Actuators, A: Physical*, vol. A33, pp. 207, 1992.

[66]   C. Liu, T. Tsao, Y.-C. Tai, and C.-M. Ho, "Surface micromachined magnetic actuators," in *Proceedings of the IEEE Micro Electro Mechanical Systems*, 1994, pp. 57-60.

[67]   C. Vancura, M. Ruegg, Y. Li, C. Hagleitner, and A. Hierlemann, "Magnetically actuated complementary metal oxide semiconductor resonant cantilever gas sensor systems," *Analytical Chemistry*, vol. 77, pp. 2690, 2005.

[68]   J. H. Seo and O. Brand, "Novel high Q-factor resonant microsensor platform for chemical and biological applications," in *Proceedings of the Transducers'2005*, 2005, pp. 593-596.

[69]   O. Brand, "Micromachined Resonators for Ultrasound Based Proximity Sensing," Ph. D. Thesis, ETH Zurich, 1994.

[70]   J. H. Seo and O. Brand, "Self-magnetic excitation for in-plane mode resonant microsensor," in *Proceedings of the IEEE Micro Electro Mechanical Systems*, 2006, pp. 74-77.

[71]   V. M. McNeil, S. S. Wang, and M. A. Schmidt, "Issues regarding the application of the electrochemical etch-stop technique to fabricate microstructures using wafer bonding," in *Proceedings of the First International Symposium on Semiconductor Wafer Bonding*, 1992, 180-189.

[72]   T. Muller, M. Brandl, O. Brand, and H. Baltes, "Industrial CMOS process family adapted for the fabrication of smart silicon sensors," *Sensors and Actuators, A: Physical*, vol. 84, pp. 126-133, 2000.

[73] B. Ratier, J. Yong Seok, A. Moliton, and P. Audebert, "Vapor deposition polymerization and reactive ion beam etching of poly(p-xylylene) films for waveguide applications," *Optical Materials*, vol. 12, pp. 229-233, 1999.

[74] D. W. Allan and J. A. Barnes, "A modified Allan variance with increased oscillator characterization ability," in *Proceedings of the Thirty Fifth Annual Frequency Control Symposium*, 1981, pp. 470-475.

[75] D. Lange, "Cantilever-based microsystems for gas sensing and atomic force microscopy," Ph.D. Thesis, ETH Zurich, 2000.

[76] R. Melamud, M. Hopcroft, C. Jha, K. Bongsang, S. Chandorkar, R. Candler, and T. W. Kenny, "Effects of stress on the temperature coefficient of frequency in double clamped resonators," in *Proceedings of the Transducers'2005*, 2005, pp. 392-395.

[77] M. J. Tudor, M. V. Andres, K. W. H. Foulds, and J. M. Naden, "Silicon resonator sensors: interrogation techniques and characteristics," *IEE Proceedings, D: Control Theory and Applications*, vol. 135, pp. 364-368, 1988.

[78] M. J. Madou, *Fundamentals of microfabrication : the science of miniaturization*, 2nd ed. Boca Raton CRC Press, 2002.

[79] J. M. Gere, *Mechanics of materials*, 6th ed. London: Brooks/Cole, 2004.

[80] W. C. Young and R. G. Budynas, *Roark's formulas for stress and strain*, 7th ed. New York: McGraw-Hill, 2002.

[81] W. C. Young and R. G. Budynas, "Beams of relatively great depth," in *Roark's formulas for stress and strain*, 7th ed. New York: McGraw-Hill, 2002, pp. 166-169.

[82] L. D. Landau and E. M. Lifshitz, *Fluid mechanics*, 2nd ed: Butterworth-Heinemann, 1987.

[83] F. M. White, *Viscous fluid flow*, 2nd ed. New York: McGraw-Hill, 1991.

[84]   Y. H. Cho, B. M. Kwak, A. P. Pisano, and R. T. Howe, "Slide film damping in laterally driven microstructures," *Sensors and Actuators, A: Physical*, vol. A40, pp. 31-39, 1994.

[85]   W. C. Tang, T.-C. H. Nguyen, and R. T. Howe, "Laterally driven polysilicon resonant microstructures," *Sensors and Actuators*, vol. 20, pp. 25-32, 1989.

[86]   O. Brand and H. Baltes, "Microsensor packaging," *Microsystem Technologies*, vol. 7, pp. 205-208, 2002.

[87]   M. Yang, M. Thompson, and W. C. Duncan-Hewitt, "Interfacial properties and the response of the thickness-shear-mode acoustic wave sensor in liquids," *Langmuir*, vol. 9, pp. 802-811, 1993.

[88]   M. I. Newton, C. R. Evans, G. McHale, N. J. Shirtcliffe, and S. M. Stanley, "The effect of SU-8 patterned surfaces on the response of the quartz crystal microbalance," *Sensors and Actuators, A: Physical*, vol. 123-124, pp. 73-6, 2005.

[89]   X. Zhang, Y. Zhu, and S. Granick, "Hydrophobicity at a Janus interface," *Science*, vol. 295, pp. 663-666, 2002.

[90]   Y. Zhu and S. Granick, "Rate-dependent slip of Newtonian liquid at smooth surfaces," *Physical Review Letters*, vol. 87, pp. 96105, 2001.

[91]   G. McHale and M. I. Newton, "Surface roughness and interfacial slip boundary condition for quartz crystal microbalances," *Journal of Applied Physics*, vol. 95, pp. 373-380, 2004.

[92]   F. L. Walls and J. J. Gagnepain, "Environmental sensitivies of quartz oscillators," *IEEE Transactions on Ultrasonics, Ferroelectrics and Frequency Control*, vol. 39, pp. 241-249, 1992.

[93]   R. Melamud, M. Hopcroft, C. Jha, K. Bongsang, S. Chandorkar, R. Candler, and T. W. Kenny, "Effects of stress on the temperature coefficient of frequency in double clamped resonators," in *Proceedings of the Transducers'2005*, 2005, pp. 392-395.

[94] A. Nakladal, K. Sager, and G. Gerlach, "Influences of humidity and moisture on the long-term stability of piezoresistive pressure sensors," *Measurement: Journal of the International Measurement Confederation*, vol. 16, pp. 21-29, 1995.

[95] T. Thundat, G. Y. Chen, R. J. Warmack, D. P. Allison, and E. A. Wachter, "Vapor detection using resonating microcantilevers," *Analytical Chemistry*, vol. 67, pp. 519-521, 1995.

[96] J.-H. Jeong, S.-H. Chung, S.-H. Lee, and D. Kwon, "Evaluation of elastic properties and temperature effects in Si thin films using an electrostatic microresonator," *Journal of Microelectromechanical Systems*, vol. 12, pp. 524-530, 2003.

[97] T. Thundat, R. J. Warmack, G. Y. Chen, and D. P. Allison, "Thermal and ambient-induced deflections of scanning force microscope cantilevers," *Applied Physics Letters*, vol. 64, pp. 2894-2896, 1994.

[98] M. Koskenvuori, T. Mattila, A. Haara, J. Kiihamaki, I. Tittonen, A. Oja, and H. Seppa, "Long-term stability of single-crystal silicon microresonators," *Sensors and Actuators, A: Physical*, vol. A115, pp. 23-27, 2004.

[99] R. L. Filler and J. R. Vig, "Long-term aging of oscillators," *IEEE Transactions on Ultrasonics, Ferroelectrics and Frequency Control*, vol. 40, pp. 387-94, 1993.

[100] B. Roith, A. Gollwitzer, A. Lerner, and G. Fischerauer, "Microcontroller-based temperature compensation scheme for two-port SAW oscillators," in *Proceedings of the 2006 IEEE International Frequency Control Symposium*, 2006, pp. 827-830.

[101] T. W. Schneider, G. C. Frye-Mason, S. J. Martin, J. J. Spates, T. V. Bohuszewicz, G. C. Osbourn, and J. W. Bartholomew, "Chemically selective coated quartz crystal microbalance (QCM) array for detection of volatile organic chemicals," in *Proceedings of the SPIE*, 1998, pp. 85-94.

[102] J. H. Smith and S. D. Senturia, "Self-consistent temperature compensation for resonant sensors with application to quartz bulk acoustic wave chemical sensors," in *Proceedings of the Transducers'1995*, 1995, pp. 724-727.

[103] T. Ono, D. F. Wang, and M. Esashi, "Mass sensing with resonating ulltrathin double beams," in *Proceedings of the IEEE Sensors*, 2003, pp. 825-829.

[104] M. G. Schweyer, J. C. Andle, D. J. McAllister, and J. F. Vetelino, "An acoustic plate mode sensor for aqueous mercury," *Sensors and Actuators, B: Chemical*, vol. B35, pp. 170-175, 1996.

[105] J. Veris, "Temperature compensation of silicon resonant pressure sensor," *Sensors and Actuators, A: Physical*, vol. 57, pp. 179-182, 1996.

[106] J. R. Vig, "Temperature-insensitive dual-mode resonant sensors-a review," *IEEE Sensors Journal*, vol. 1, pp. 62-8, 2001.

[107] K. Ogata, *Modern control engineering*, 4th ed. Upper Saddle River, NJ: Prentice Hall, 2002.

[108] C. Seungkeun, K. Seong-Hyok, Y. Yong-Kyu, and M. G. Allen, "A magnetically excited and sensed MEMS-based resonant compass," *IEEE Transactions on Magnetics*, vol. 42, pp. 3506-8, 2006.

[109] R. Sunier, T. Vancura, Y. Li, K.-U. Kirstein, H. Baltes, and O. Brand, "Resonant magnetic field sensor with frequency output," *Journal of Microelectromechanical Systems*, vol. 15, pp. 1098-1107, 2006.

[110] M. A. Hopcroft, M. Agarwal, K. K. Park, B. Kim, C. M. Jha, R. N. Candler, G. Yama, B. Murmann, and T. W. Kenny, "Temperature compensation of a MEMS resonator using quality factor as a thermometer," in *Proceedings of the IEEE Micro Electro Mechanical Systems*, 2006, pp. 222-225.

[111] J. Thurn and R. F. Cook, "Stress hysteresis during thermal cycling of plasma-enhanced chemical vapor deposited silicon oxide films," *Journal of Applied Physics*, vol. 91, pp. 1988-1992, 2002.

[112] J. A. Chiou and S. Chen, "Thermal hysteresis analysis of MEMS pressure sensors," *Journal of Microelectromechanical Systems*, vol. 14, pp. 782-787, 2005.

[113] F. J. Dechow, "Enzyme Immobilization," in *Separation and Purification Techniques in Biotechnology,* William Andrew Publishing/Noyes 1989, pp. 307-310.

[114] S. K. Bhatia, M. J. Cooney, L. C. Shriver-Lake, T. L. Fare, and F. S. Ligler, "Immobilization of acetylcholinesterase on solid surfaces: chemistry and activity

studies [for biosensor technology]," *Sensors and Actuators, B: Chemical*, vol. B3, pp. 311-317, 1991.

[115] M. C. Flickinger and S. W. Drew, "Enzymes, Immobilization Methods," in *Encyclopedia of bioprocess technology: fermentation, biocatalysis, and bioseparation*, New York: John Wiley, 1999, pp. 1062-1145.

[116] M. C. Flickinger and S. W. Drew, "Cell Immobilization," in *Encyclopedia of bioprocess technology: fermentation, biocatalysis, and bioseparation,* New York: John Wiley, 1999, pp. 504-513.

[117] A. Nanci, J. D. Wuest, L. Peru, P. Brunet, V. Sharma, S. Zalzal, and M. D. McKee, "Chemical modification of titanium surfaces for covalent attachment of biological molecules," *Journal of Biomedical Materials Research*, vol. 40, pp. 324-335, 1998.

[118] R. A. Williams and H. W. Blanch, "Covalent immobilization of protein monolayers for biosensor applications," *Biosensors and Bioelectronics*, vol. 9, pp. 159-167, 1994.

[119] L. C. Shriver-Lake, B. Donner, R. Edelstein, K. Breslin, S. K. Bhatia, and F. S. Ligler, "Antibody immobilization using heterobifunctional crosslinkers," *Biosensors and Bioelectronics*, vol. 12, pp. 1101-1106, 1997.

[120] F. Mizutani, Y. Sato, S. Yabuki, T. Sawaguchi, and S. Iijima, "Enzyme electrodes based on self-assembled monolayers of thiol compounds on gold," *Electrochimica Acta*, vol. 44, pp. 3833-3838, 1999.

[121] K. A. Peterlinz and R. Georgiadis, "In situ kinetics of self-assembly by surface plasmon resonance spectroscopy," *Langmuir*, vol. 12, pp. 4731-4740, 1996.

[122] R. Marie, H. Jensenius, J. Thaysen, C. B. Christensen, and A. Boisen, "Adsorption kinetics and mechanical properties of thiol-modified DNA-oligos on gold investigated by microcantilever sensors," *Ultramicroscopy*, vol. 91, pp. 29-36, 2002.

[123] J. Moon, T. Kang, S. Oh, S. Hong, and J. Yi, "In situ sensing of metal ion adsorption to a thiolated surface using surface plasmon resonance spectroscopy," *Journal of Colloid and Interface Science*, vol. 298, pp. 543-549, 2006.

[124] C. Grogan, R. Raiteri, G. M. O'Connor, T. J. Glynn, V. Cunningham, M. Kane, M. Charlton, and D. Leech, "Characterisation of an antibody coated microcantilever as a potential immuno-based biosensor," *Biosensors and Bioelectronics*, vol. 17, pp. 201-207, 2002.

[125] R. H. Jacobson, X. J. Zhang, R. F. DuBose, and B. W. Matthews, "Three-dimensional structure of beta-galactosidase from E coli," *Nature*, vol. 369, pp. 761-766, 1994.